UNIVERSITY OF BIRMINGHAM

IN-SITU TRANSMISSION ELECTRON MICROSCOPY STUDY OF DISLOCATION IN TI-6AL-4V

by

XINYU LU

A thesis submitted to the University of Birmingham for the degree of DOCTOR OF PHILOSOPHY

School of Metallurgy and Materials

University of Birmingham

MARCH 2017

Preface

This research was carried out by Xinyu Lu in School of Metallurgy and Materials, University of Birmingham (from September 2012 to September 2016), under the supervision of Dr YuLung Chiu and Prof Ian Jones.

The present work is original and no part of the work has been submitted for another degree at any other university. Wherever other researchers' work has been drawn or cited, it is acknowledged in the text and the references are listed.

Abstract

In-situ TEM compression testing is able to probe quantitatively the mechanical response of materials with simultaneous imaging of the deformation microstructure evolution. Ti-6Al-4V (Ti64), known for high strength, is the most widely used Ti alloy. A better understanding of the plastic deformation micro-mechanisms is sought using in-situ TEM studies. This project investigates the dislocation characterization of bulk Ti64 and the dislocation activities in micro-pillars during in-situ TEM compression.

The as-annealed specimen has two types of low angle grain boundaries (LAGBs): <a> and <c+a>. <c+a> LAGB is on the basal plane and formed by <c+a> dislocations with various Burgers vectors. Due to different types of misfit, dislocations existing on different β/α interfaces during phase transformation, the consequential LAGBs adopt specific crystallographic planes. Dislocation interactions may also lead to a greater variety of <c+a> dislocations on LAGBs. These <c+a> LAGBs are sessile and show only a weak hindering effect on the slip bands during macro-compression. <a> type screw dislocations cross slip between the prismatic plane and the first order pyramidal plane. The cross-slipped dislocations dissociate into extended dislocations on prismatic planes, which leads to strong residual contrast of some slip bands.

In-situ TEM compression tests were performed on three groups of pillars along $[12\bar{3}4]$, $[\overline{20}8,12,7]$ and $[0001]$ directions give rise to single slip ($\frac{1}{3}[11\bar{2}0](0002)$), multiple slip ($\frac{1}{3}[\bar{1}\bar{1}20](1\bar{1}00), \frac{1}{3}[\bar{2}110](000\bar{1})$) and <c+a> pyramidal

slip ($\frac{1}{3}[1\bar{2}13](\bar{1}101)$), respectively. A viewing g vector perpendicular to the loading direction is ideal for avoiding most bend contours.

The first dislocation source was always produced at the probe/pillar contact surface and continuously created dislocations. These dislocations accumulated in the pillar and eventually formed steps on the free surface which slightly relieved the strain. The increase of slip steps can be linked to stain bursts and load drops in the stress-strain curves. Dislocation sources at other positions in the pillar were less favourable until the source at the contact surface became exhausted. Movements of dislocations emitted from the contact surface were slow and heterogeneous due to obstacles. The speed of <a> basal slip is ten times faster than <c+a> pyramidal slip. The dislocations emitted from other sources moved much more quickly.

Planar slip exists in micro-pillars and is loading direction-dependent. Planar slip occurs in <a> basal slip but not in <c+a> pyramidal slip, where the strong entanglement of dislocations leads to uniform deformation. The pre-existing <c+a> LAGBs remained on the basal plane and prevented the motion of newly generated dislocations to a limited extent. The pre-existing non-basal <c+a> dislocations were slightly activated but for the most part pinned and did not perform as dislocation sources during deformation.

Pillars start to yield when shear bands initiate on the free surface. The first dislocation generates in the pillar long before obvious yielding. Compared with the bulk sample, yield stresses are dramatically increased for micro-pillars, which is consistent with the dislocation starvation hypothesis.

Acknowledgements

Firstly, I would like to express my deepest appreciation and gratitude to Dr YuLung Chiu and Prof Ian Jones, my academic supervisors, for their professional supervision, patient guidance and continuous encouragement throughout the entire project. Dr YuLung Chiu has provided enlightening suggestions and personal help. Prof Ian Jones supervised my academic research with his wide scientific knowledge and cheered me up with his enthusiasm.

Many thanks is given to Dr Rengen Ding for his practical guidance and academic advice. I would like to thank Mr Paul Stanley and Mrs Theresa Morris of the Electron Microscope Centre for their support.

I am especially appreciative of the nice company provided by my colleagues in the EM group over these years: Xinxin Zhao, Ruiling Zeng, Yu Lu, Thiago Pereira, Rayan Ameen, Bo Pang, Jing Wu, Zhaoran Liu, Minshi Wang, Daniel Higgins, Gareth Douglas, Jinsen Tian, Subash Rai, Shanshan Si and Ubaid Ur Rehman Ghori. It is a pleasant and wonderful experience to work with them.

Finally, I would like to thank my parents and boyfriend for their endless support, patience and love, which encourage me to be optimistic and enthusiastic in my study.

Contents

Chapter 1. Introduction

Ti-6Al-4V, known for high strength and good corrosion resistance, has been widely used in aircraft and aerospace. The slip of many dislocations on a microscopic level constitutes macroscopic plastic deformation.

In-situ TEM mechanical tests which have been studied for more than 60 years offer the opportunity to observe the dynamic response of materials subjected to external stimuli, such as temperature, pressure etc. Significant progress has been made thanks to improved sample geometries, precise load control and high resolution force and displacement measurement. Quantitative in-situ TEM compression is able to measure the mechanical response of materials with simultaneous imaging of dislocation motion. Although there are some breakthroughs in the technology, the application of in-situ experiments is still limited by stringent processing requirements, high resolution imaging and data capture. Significant challenges are still associated with the preparation, handling and testing of small volumes of material.

It is of interest to achieve a better understanding of the plastic deformation micro-mechanisms using in-situ TEM studies. This project investigates the dislocation characterization of bulk Ti64 and the dislocation activities in micro-pillars during the in-situ TEM compression.

The outline of this PhD thesis is as follows:

Chapter 2 presents a literature review of the microstructure and mechanical properties of Ti64, deformation mechanisms of the α phase of Ti64 and the historical development of micro-scale mechanical testing, especially in-situ TEM testing.

Chapter 3 summarizes experimental procedures, in particular the experimental method for in-situ TEM testing.

Chapter 4 identifies the dislocation characteristics and slip behaviour of the as-received, annealed and macro-compressed Ti64 specimens.

Chapter 5 presents the in-situ TEM test results from three groups of pillars with single slip, multiple slip and <c+a> slip respectively activated.

Chapter 6 compares the dislocation behaviour in the macro-compression and in-situ TEM compression and also discusses the mechanical behaviour of different groups of pillars.

Chapter 7 draws the main conclusions of this study and makes some suggestions for future work

Chapter 2. Background

2.1. Titanium alloys

Titanium alloys have low density, high yield stress and fatigue strength and good corrosion resistance. These characteristics make titanium alloys an ideal choice for aircraft and aerospace applications. Some of the basic characteristics of titanium compared to other structural metals are listed in Table 2.1.

Table 2.1 Characteristics of Ti, Fe, Ni and Al [1]

	Ti	Fe	Ni	Al
Melting Temperature (°C)	1670	1538	1455	660
Allotropic Transformation (°C)	$\beta \overset{882}{\longrightarrow} \alpha$	$\gamma \overset{912}{\longrightarrow} \alpha$	-	-
Crystal Structure	bcc → hcp	fcc → bcc	fcc	fcc
Room Temperature E (GPa)	115	215	200	72
Density (g/cm^3)	4.5	7.9	8.9	2.7
Comparative Corrosion Resistance	Very high	Low	Medium	High
Comparative Reactivity with Oxygen	Very high	Low	Low	High
Comparative Price of Metal	Very high	Low	High	Medium

Under atmospheric pressure, Ti generally exists as α phase at low temperature and β phase at high temperature. Figure 2.1 shows the unit cells of the α and β phases. α phase has the hexagonal closely packed (hcp) structure, while β phase has the body centred cubic (bcc) structure. The axial ratio c/a of α phase is 1.587, smaller than the ratio of the ideal hcp crystal (1.63). Ti and its alloys also have other allotropes such as pressure induced ω phase, non-equilibrium hexagonal and orthorhombic martensite [2]. However, such modifications are not within the scope of this project.

Pure Ti undergoes an allotropic phase transformation at 882°C [1]. For Ti alloys, the exact transformation temperature is much influenced by alloying elements [3].

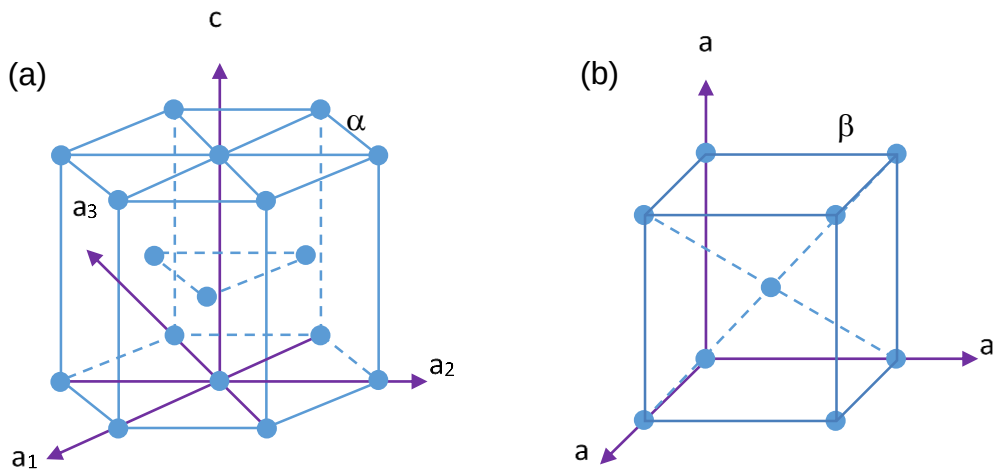

Figure 2.1 Unit cells of (a) α phase and (b) β phase

2.1.1. Ti-6Al-4V

Ti-6Al-4V (Ti64) is a typical α+β alloy with the typical chemical composition of commercial Ti64 is show in Table 2.2. Al is a strong α stabilizer, which increases the transus temperature. On the other hand, V stabilizes β phase [4]. The α/β phase transus temperature of Ti64 is around 996°C. Ti64 combines the advantages of strength of α phase and ductility of β phase.

Table 2.2 The typical chemical composition (wt%) of commercial Ti-6Al-4V alloy [5]

Composition	Ti	Al	V	Fe	O	C	N	H
Wt%	Bal	5.5-6.5	3.5-4.5	<0.25	<0.2	<0.08	<0.07	<0.0125

The transformation of β to α phase occurs by a nucleation and shear type process when cooling through the transus temperature. α phase and the parent β phase follow the Burgers orientation relationship (OR) [6]:

$$(0001)_\alpha \,/\!/\, \{110\}_\beta$$

$$\langle 11\bar{2}0\rangle_\alpha \,/\!/\, \langle 111\rangle_\beta$$

The Burgers OR results in an α/β interface plane near to one of the $\{10\bar{1}0\}$ prismatic planes [7] and varies slightly depending on the chemical composition in order to minimize the interfacial dislocation energy and allow the easy slip transmission of specific systems through the α/β interface. Figure 2.2 is a schematic diagram showing the crystallographic relationship between α and β lamellae within the Burgers OR [8].

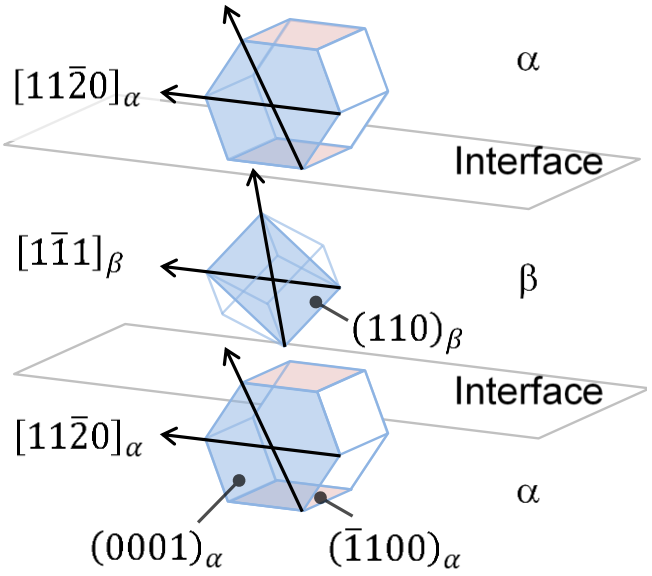

Figure 2.2 Burgers orientation relationship between α and β phases.

The microstructure and texture of Ti64 have significant impact on its mechanical behaviour. In Ti64, three types of microstructures (Figure 2.3) can be obtained by changing the thermo-mechanical processing route: fully lamellar structures, fully equiaxed structures, and bi-modal microstructures which contains primary α (α_p) and lamellar α/β grain. The fully lamellar structure is applied to applications that require

fatigue crack propagation resistance, creep resistance and high fracture toughness [3]. The colony size and width of the lamellae determine the performance of lamellar structured Ti64. Bi-modal structures provide good yield strength, tensile ductility and fatigue strength. Fully equiaxed structures possess good ductility and fatigue strength. However, compared to bi-modal microstructures, fully equiaxed microstructures reduce the fatigue crack nucleation resistance, since the strong crystallographic texture can make the slip length in fully equiaxed structures much larger than α grain size. For the bi-modal structure, Lütjering [9] pointed out that the strength of material increased with decreasing volume fraction of α_p. Therefore, the volume fraction of α_p in bi-modal microstructures should be kept below about 50% to avoid extensive converging of α_p grains in practical production [3].

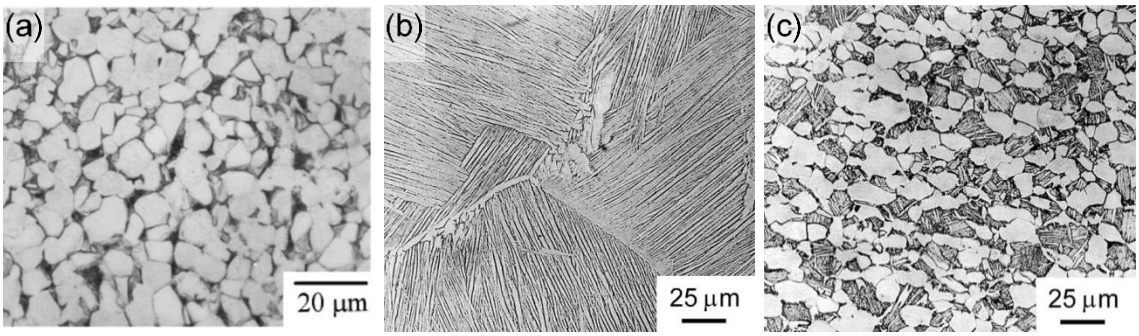

Figure 2.3 Typical microstructures of Ti64 (a) equiaxed [10] (b) fully lamellar [11] (c) bi-modal [11].

Texture strongly affects the mechanical behaviours of Ti64 due to the anisotropy of the crystallographic slip associated with the HCP crystal [12]. For instance, the yield strength may enhance by 40% for certain textured Ti-Al alloys [13]. For the Ti64

processed by rolling and forging, three categories of texture can be produced at different processing temperatures, viz. basal, transverse and basal/transverse textures [14]. These textures are resulted from the processing at around 815°C, 980°C and the intermediate working temperatures, respectively. A random texture can also be found in commercial Ti64. Figure 2.4 shows an example of (0001) pole figures of these textures with normal direction (ND) perpendicular to the rolled sheet [15].

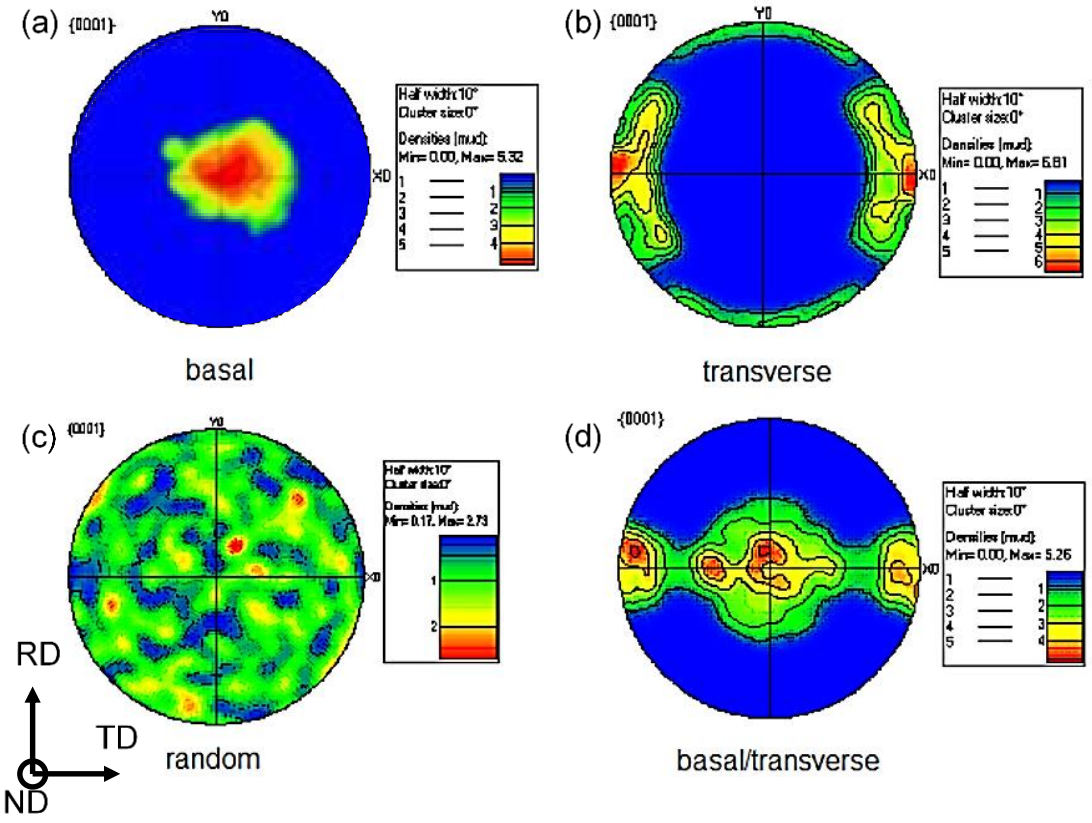

Figure 2.4 (0001) pole figures of (a) basal, (b) transverse, (c) random and (d) basal/transverse textures [15]. Arrows indicate the rolling direction (RD) and transverse direction (TD)

Mueller et al. [16] has specifically studied the influence of extrusion temperature on the resultant texture and mechanical properties of Ti64 rods. The texture analyses were performed on the cross section of the rods. Figure 2.5 [16] shows the 0002 pole figure of billet material and extruded rods at different temperatures. The billet material (Figure 2.5a) possesses a typical two-dimensional formed texture. The highest intensities of the basal planes transfer from the circular around the extrusion axis (Figure 2.5b) to the centre (Figure 2.5d) with the increase of extrusion temperature from 920°C to 1000°C.

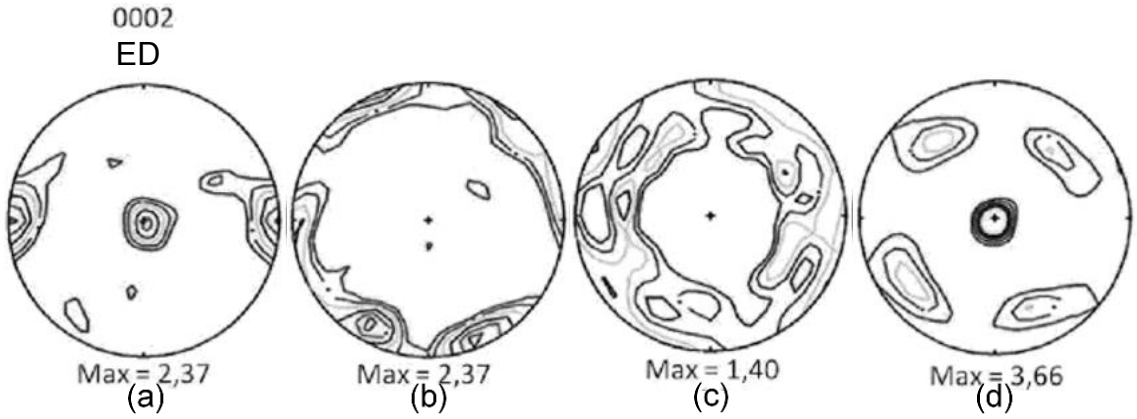

Figure 2.5 0002 pole figure of (a) billet material (b) extruded rods at 920°C (c) extruded rods at 960°C (d) extruded rods at 1000°C. [16]

2.2. Dislocations and deformation

For a perfect crystal, if plastic deformation is to occur when the shear stress τ displaces a whole layer of atoms from one equilibrium position to another, an approximate expression for τ would be: $\tau = \tau_{max} \sin\left(2\pi \frac{x}{a}\right)$, where a is the interatomic spacing and τ_{max} would be the yield stress. Using $\gamma = x/a$ as the shear strain, the shear modulus G can be written as: $G = \frac{d\tau}{d\gamma}\Big|_{\gamma \to 0} = \tau_{max} \cdot 2\pi$. Thus, $\tau_{max} = G/2\pi$.

However, the experimentally observed yield stress is 2-3 orders of magnitude smaller than the theoretical value τ_{max} [17]. The difference between predication and experiment was first accounted for by dislocation theory in 1934 [18].

A dislocation is a line defect in the crystal. One example consists of the edge of an extra plane of atoms halfway between the normal equilibrium positions. Instead of displacing the entire plane of atoms to achieve plastic deformation, the shear stress only needs to move the plane of atoms above the dislocation by one atomic spacing. This greatly reduces the stress required. The slip of many dislocations on a microscopic level constitutes macroscopic plastic deformation. The applied stress required to overcome the lattice resistance to the dislocation movement is the Peierls-Nabarro stress [19-21], which is often described as the critical resolved shear stress (CRSS) at 0K [22].

2.2.1. Slip systems

The common slip systems in the BCC β phase have a $\langle 111 \rangle$ slip direction on $\{110\}$, $\{112\}$ and $\{123\}$ slip planes. Since α is the dominant phase in Ti64, slip in α phase plays an important role in the deformation of Ti64, this survey mainly focuses on α phase.

The deformation of pure α-titanium has been extensively studied [23]. Generally speaking, slip can occur on prismatic, pyramidal and basal planes by the movement of <a>, [c] and <c+a> type dislocations. <a> type dislocations (with the Burgers vector of $\frac{1}{3}\langle 11\bar{2}0 \rangle$) are common to all three planes - basal, prismatic and first order pyramidal planes. <c+a> (with the Burgers vector of $\frac{1}{3}\langle 11\bar{2}3 \rangle$) slip can take place on prismatic and first order pyramidal planes. [c] type dislocation is restricted to prismatic planes only and does not glide [24]. The operation of <a> type dislocation slip provides only four independent slip systems [1], which do not allow shear straining along the c-direction. In order to satisfy the von Mises criterion which requires at least five independent slip systems for extensive ductility in polycrystalline materials, and to achieve a displacement in the c-direction, another deformation mode needs to be activated. The potential deformation modes providing this additional degree of freedom are <c+a> slip on first-order $\{10\bar{1}1\}$ or second-order $\{11\bar{2}2\}$ pyramidal planes, or twinning in some cases. While twinning is often observed in unalloyed Ti and some α/β Ti-Al alloys, the potential for twinning decreases with increasing Al content [25]. Twinning is rarely observed in Ti64. The

common slip planes and slip directions for α titanium are listed in Table 2.3 and indicated in the hexagonal unit cell in Figure 2.4.

Table 2.3 Slip systems in α phase[1]

Slip system type	Burgers vector type	Slip direction	Slip plane	No. of slip systems	
				Total	Independent
1	a	$\langle 11\bar{2}0\rangle$	(0002)	3	2
2	a	$\langle 11\bar{2}0\rangle$	$\{10\bar{1}0\}$	3	2
3	a	$\langle 11\bar{2}0\rangle$	$\{10\bar{1}1\}$	6	4
4	c+a	$\langle 11\bar{2}3\rangle$	$\{10\bar{1}1\}$	6	5

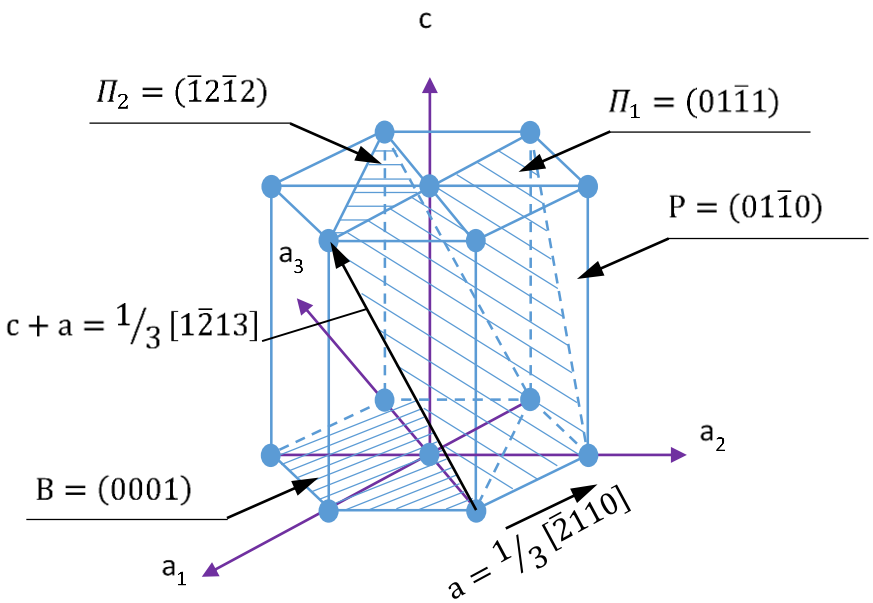

Figure 2.6 Slip systems in α phase: basal (B), prismatic (P) and first-order pyramidal (Π_1) planes containing <a> dislocations; first (Π_1) and second-order (Π_2) pyramidal slip planes containing <c+a> dislocation.

The basal planes in HCP materials with the c/a ratio greater than 1.633 have the largest inter-planar spacing. In these cases, $\langle\bar{1}\bar{1}20\rangle(0002)$ is the principal slip system and the common <c+a> slip is $\langle\bar{1}\bar{1}23\rangle\{11\bar{2}2\}$. Titanium, with the c/a ratio less than 1.633, the most common slip systems are $\langle a\rangle$ slip on prismatic plane [26] and $\langle c+a\rangle$ on $\{10\bar{1}1\}$ plane [27]. The preferred slip plane depends on the <a> type dissociated dislocation core structure and the staking fault energy of the different families of slip planes [28]. Slip in Ti is dominated by screw dislocations, which have non-planar equilibrium dislocation cores spreading into the prismatic plane [28]. Only a few reports are about $\langle\bar{1}\bar{1}23\rangle\{11\bar{2}2\}$ slip in Ti: Minonishi and Morozumi [29] compressed a single crystal of Ti along the c axis and indirectly inferred $\langle\bar{1}\bar{1}23\rangle\{11\bar{2}2\}$ slip. Their results showed that crystals mainly deformed by twinning on $\{11\bar{2}2\}$ at room temperature associated with $\langle c+a\rangle$ slip.

2.2.2. Schmid factor

The Schmid factor characterizes the effectiveness of a slip system. According to Schmid's law [30], when a force F acts upon a single crystal with cross-sectional area *A*, the shear stress τ resolved in the slip direction is:

$$\tau = \frac{F\cos\lambda}{A/\cos\varphi} = \sigma\cos\varphi\cos\lambda$$

φ is the angle between the loading direction and the slip plane normal. λ is the angle between the loading direction and the slip direction. $\sigma = \mathrm{F/A}$ is the applied stress. $\mathrm{m} = \cos\varphi \cos\lambda$ known as the Schmid factor. When the shear stress is larger than the critical resolved shear stress, the slip system will be activated. Thus, under a certain direction of loading, a slip system with a larger Schmid factor is more inclined to be activated.

The interplanar and inter-directional angle formulae for an hcp material using Miller-Bravais four-axis indices are listed below [31]:

$$\cos\varphi = \frac{h_1h_2 + k_1k_2 + i_1i_2 + \frac{3a^2}{2c^2}l_1l_2}{\left\{\left({h_1}^2 + {k_1}^2 + {i_1}^2 + \frac{3a^2}{2c^2}{l_1}^2\right) \times \left({h_2}^2 + {k_2}^2 + {i_2}^2 + \frac{3a^2}{2c^2}{l_2}^2\right)\right\}^{1/2}}$$

$$\cos\lambda = \frac{u_1u_2 + v_1v_2 + t_1t_2 + \frac{2c^2}{3a^2}w_1w_2}{\left\{\left({u_1}^2 + {v_1}^2 + {t_1}^2 + \frac{2c^2}{3a^2}{w_1}^2\right) \times \left({u_2}^2 + {v_2}^2 + {t_2}^2 + \frac{2c^2}{3a^2}{w_2}^2\right)\right\}^{1/2}}$$

where h,k,i,l and u,v,t,w are the corresponding four index planes and directions.

2.2.3. Critical resolved shear stress (CRSS)

The CRSS is the resolved shear stress in the slip direction on the slip plane necessary to initiate slip. The low symmetry of the hcp structure results in different CRSS for different slip systems. CRSS is also temperature-dependent, since the motion of dislocation is a stress-assisted thermally activated phenomenon. The evolution of the CRSS with temperature describes the interplay between the influence of stress and temperature with two extreme cases. The Peierls stress at 0K where lattice friction is overcome under the sole influence of stress and the thermal regime where thermal activation frees the dislocation from lattice friction. [22]

The CRSS also affects the probability of the activation of a particular slip system. To determine the CRSS, numerous studies have been conducted on the deformation of Ti-Al binary alloys subjected to different strain rates at different temperatures. Generally speaking, the CRSS of <a> slip is much lower than that of <c+a> slip. The low CRSS of prismatic and basal <a> slip makes their activation easy. The high value of CRSS of <c+a> slip on pyramidal planes is mainly due to its large Burgers vector [32]. Thus, the percentage of grains deforming by <c+a> slip is quite low in α titanium polycrystals. <c+a> dislocations are only activated when the dislocation mobility for <a> type is minimized, i.e. the sample under a loading direction nearly parallel to the c-axis or deformed at low temperatures and/or high strain rates [7]. <c+a> dislocations were also observed near grain boundaries to relieve incompatibility strains developed during deformation of polycrystals [33].

The absolute values of CRSS are strongly dependent on alloy content and test temperature. Prismatic slip dominates deformation of Ti-Al binary alloys when Al content is low (< 2.9 wt.%) [25]. Basal slip becomes important with increasing Al concentration [25]. The CRSS of all slip systems decreases with increasing temperature [34]. Salem [34] measured the CRSS of slip systems in Ti64 with a lamellar microstructure at 815°C. The CRSS of a_1 prismatic slip measured by Salem is about 42MPa which is one fifth of the value at room temperature (210MPa) measured by Savage et.al. [35] in a similar material, Ti-6246Si. There is little difference in CRSS at room temperature between the three types of slip systems with <a> Burgers vector, although $\{10\bar{1}0\} \leq \{10\bar{1}1\} \leq (0002)$ CRSS. At room temperature, the relative CRSS values for α-Ti and α/β Ti alloys were summarized by Mayeur [36] and are shown in Table 2.4.

Mayeur's [36] final adopted radio of $\tau_{\mathrm{CRSS}}^{\mathrm{basal}<a>} / \tau_{\mathrm{CRSS}}^{\mathrm{prism}<a>}$, $\tau_{\mathrm{CRSS}}^{\mathrm{pyr}<a>} / \tau_{\mathrm{CRSS}}^{\mathrm{prism}<a>}$ and $\tau_{\mathrm{CRSS}}^{\mathrm{pyr}<c+a>} / \tau_{\mathrm{CRSS}}^{\mathrm{prism}<a>}$ were 1, 2, 3, respectively, Given $\tau_{\mathrm{CRSS}}^{\mathrm{prism}<a>} = 300MPa$. Rengen et.al. [37, 38] studied the compressive CRSS values for different slip systems in Ti64 micro-cantilevers, Combined the study of Mayeur and Rengen et.al., the following CRSS values can be used as reference values in single α phase: $\tau_{\mathrm{CRSS}}^{\mathrm{prism}<a>} = 340MPa$, $\tau_{\mathrm{CRSS}}^{\mathrm{basal}<a>} = 340MPa$, $\tau_{\mathrm{CRSS}}^{\mathrm{pyr}<a>} = 680MPa$, $\tau_{\mathrm{CRSS}}^{\mathrm{pyr}<c+a>} = 1035MPa$.

Table 2.4 Relative CRSS of slip systems for α-titanium and α/β Ti alloys, normalized to the CRSS for prismatic slip at room temperature [36]

$\tau_{CRSS}^{basal<a>}/\tau_{CRSS}^{prism<a>}$	$\tau_{CRSS}^{pyr<a>}/\tau_{CRSS}^{prism<a>}$	$\tau_{CRSS}^{pyr<c+a>}/\tau_{CRSS}^{prism<a>}$	Reference
1.25	-	2.625	Paton et al., 1973 [39]
0.93-1.3	1	1.1-1.6	Medina et al., 1995 [33]
1.5	1	3	Dunst and Mecking, 1996 [40]
5	5	8.0-15.0	Fundenberger et al., 1997 [41]
1	-	8	Lebensohn and Canova, 1997 [42]
1.43	-	4.23	Bieler and Semiatin, 2001 [43]
1	2	3	Mayeur, 2007 [36]

(τ_{CRSS} represents the critical resolved shear stress; the superscripts represent different slip systems)

2.2.4. Low angle grain boundaries (LAGBs)

LAGBs are composed of an array of widely-spaced lattice dislocations and are repeatedly observed through various methods such as chemical etching [44], decoration technique, field ion microscopy and TEM [45]. ‘Low angle’ here means that the misorientation between the two sides of the boundary is less than 10°.

Grown-in dislocations in annealed materials have relatively low density. The distribution of these grown-in dislocations could be random or regular. Thus, the LAGB is an important type of dislocation arrangement in annealed materials. LAGBs also play roles in the plastic deformation: obstacles to dislocation motion, accommodation of deformation of the neighbouring grains, dislocation sources, etc.

On the other hand, high angle grain boundaries (HAGBs) whose misorientation is greater than 10° are not investigated in this study. Since HAGBs have a disordered structure, it cannot be described by relatively simple configuration of dislocations.

LAGBs can be divided into three types: tilt, twist and mixed, depending on the relative orientation of the rotation axis with respect to the boundary plane. The rotation axis of a tilt boundary lies on the boundary plane, since tilt boundary consists of an array of edge dislocations arranged one above the other. Such an array produces a tilt between the grains on opposite sides of the boundary. For the symmetrical tilt boundary, the tilt angle and dislocation separation distance are connected by the Read-Shockley model [46]: $\theta = b/D$, where θ is the angle of misorientation (arc), b is the magnitude of the Burgers vector and D is the dislocation separation distance. A more general tilt boundary with two degrees of freedom and

asymmetry boundary plane consists of two sets of uniformly spaced edge dislocations with mutually perpendicular Burgers vector, b_1 and b_2.The relationship between tilt angle ($\theta \ll 1$) and dislocation separation distance (D_1,D_2) is: $\theta = \frac{b_1}{D_1 \sin\varphi} = \frac{b_2}{D_2 \cos\varphi}$, where φ is an arbitrary angle between boundary plane and the main [100] direction of two grains [45]. A simple twist boundary formed by pure screw dislocations keeps stable with two sets of dislocations. In each set, $\theta = b/D$ still works [45].

For a general low-angle boundary, Frank's relation [47] is a more precise formula to determine the arrangements of dislocations in the boundary for small values of θ:

$$d = (r \times l)\theta$$

where r is an arbitrary vector lying in the boundary plane, l is a unit vector parallel to the rotation axis, $d = \sum_i N_i b_i$ is the sum of the Burgers vectors intersected by r, N_i is the number of dislocations of Burgers vectors cut by r.

In the previous work, LAGBs composed by one or two sets of dislocations are commonly observed by high resolution TEM [48-51]. Atomic structures of LAGB also have been simulated in terms of local energy [52]. Most study of LAGB was focus on the energy and mobility [49, 53-56]. The characterization of the dislocations in themselves is rarely mentioned. Akhtar and Teghtsoonian [44] observed <a> type edge dislocations on the LAGB parallel to the $[11\bar{2}0]$ direction in an annealed α-Ti. LAGBs formed by <c+a> dislocations have been barely observed in annealed Ti alloys. Dongliang Lin and Yi Liu [57, 58] investigated the dislocation configurations in

LAGBs of a deformed Fe_3Al alloy, which had different type of Burgers vectors. They explained the cause of formation as the reaction products of absorbed dislocations at LAGBs.

Grain boundary migration facilitates many microstructural evolution processes such as recrystallization and grain growth in polycrystals. The atomic configurations are collectively rearranged while grain boundary migrating and constrained in the boundary by the symmetries of the adjoining crystalline grains. The migration of LAGBs has been described as the collective motion of the dislocation array, when the Peach-Kohler force on the constituent dislocations is non-zero [54]. Lim et al. [54, 55] simulated the interaction of dislocations with LAGBs. Simulation of interaction of dislocations with LAGB network has also been studied [56, 59]. It would be more complicated in terms of the long-range nature of the elastic interdislocation interactions in LAGB. Paolo Moretti et al. [60] investigated the depinning transition of LAGBs and dislocation pileups using different models compared over the pinning stress and pinning lengths. The mobility of LAGB has been discussed. They indicated that the interaction between dislocation lines of different type in the LAGB and the dynamics constraints upon the motion of dislocation lines on their respective slip planes lead to the formation of metastable jammed configuration. The mechanism of the interactions needs further investigation.

2.3. Micro-scale mechanical test

With the increasing miniaturization of devices, the reliability and performance of small scale components have become more important. An accurate characterization of micro-scale materials is essential not only for miniature devices, such as micro-electro-mechanical systems (MEMS), but also to the fundamentals of micro-scale materials science. Therefore, micro-scale mechanical tests arise as required, which investigate the mechanical behaviour of materials with a characteristic dimension of the order of 0.1-10 μm. At this scale, materials usually express different mechanical behaviours from bulk ones, which is known as the size effect [61].

Extensive work has been done on micro-scale mechanical tests with a variety of test methodologies. Hemker et al. [61] give a good overview of the differences between various methods. The acquisitions, limitations and applications are summarized and listed in Table 2.5.

Among all the existing techniques, tensile and compression tests are the standard method for determining the mechanical properties of macro-scale specimens. They have the advantages of simplicity and the generation of a uniform stress state which provides readily interpretable data permitting to extract useful information in both elastic and plastic regimes. When comparing these two methods, compression tests have less procedure in the sample preparation and alignment, while tensile tests provide more real time mechanical information.

Table 2.5 Comparison of different micro-scale mechanical tests [61]

Test methods	Acquisitions	Limitations	Applications	Properties
Nanoindentation	Hardness, elastic modulus [62]	No strength and strain hardening	Thin films on hard substrates [63]	Indentation size dependent [62]
Bugle test	Young's modulus Poisson's ratio [64, 65]	Difficult to handle small samples	Substrate-free thin films [64]	
Micro-cantilever	Strength [66] fracture toughness [67]	Boundary condition and geometry dependence	Fatigue [67]	Larger deflections at lower loads
compression	uniform stress state			study size effects [68]
tensile	uniform stress state easy to analyze both elastic and plastic regimes [69]			dramatic increase in yield strength [70] [71]

2.3.1. Size effect

Size effects were seldom considered in plastic analysis until technical applications involving plasticity confined to small-scale, such as micro/nano-fabrication technologies, MEMS, composites, etc. Interest in the scale influence on plasticity is currently booming because several size effects in plasticity are known to exist in the small-scale range. [72]

Fundamental elastic interactions and intrinsic fracture toughness show no size effect since they depend on the bonding nature between the constituent atoms [61, 73]. By contrast, plastic deformation depending strongly on dislocation movement under induced stress [74] shows a size effect. Size effects govern the strength of ductile materials by creating geometrical constraints and surface effects, which force dislocations to move only in preferred directions. The fracture strength of brittle materials is extremely dependent on flaw size and distribution according to the Griffith relation. Therefore, smaller specimens or stressed regions tend to have higher fracture strength [75].

Size effects in dislocation-mediated plasticity can be classified into intrinsic and extrinsic types. The intrinsic size effect refers to the concomitant increase in strength and loss of ductility due to the reduction of defects with the decreasing sample size. Small sample size limits the generation, interaction and motion of dislocations. The principal mechanisms for the intrinsic size effect linked to the geometrically necessary dislocations and pile-up effects [76], dislocation starvation [77], dislocation source truncation [78] and changes in the dislocation forest [79]. Extrinsic size effect

could be caused by the plastic strain gradients or by the boundary conditions [61]. Crystalline materials accommodate plastic gradients by storing geometrically necessary dislocations, responsible for many size effects of practical interest [61].

Early studies of size effects originated from micron-size whiskers. Brenner [80] discovered a dramatic increase in the strength of whiskers with decreasing diameter. The strongest exhibit strength approached the ideal strength of a perfect crystal. Based on Frank and Read dislocation source theory, the resolved shear stress $\tau = Gb/l$ is determined by the source length (l) and thereby related to the statistical distribution of dislocations. A small sample size which limits the source quantity and source length will lead to a higher strength. Greer and Nix [77, 81] assumed dislocation starvation theory that dislocations leave the pillar before multiplication occurs, subsequently causes high stress required to activate new dislocations. Parthasarathy et al. [78] proposed size effect theory (single arm source) based on the availability of dislocation sources. In small-scale samples, dislocation sources were assumed to be controlled by the largest average distance between internal pinning points and the free surface [78]. Rao et al. [82] improved the theory by introducing the term exhaustion hardening which related to the cessation of initially-operating sources due to interaction with obstacles and other sources. By this theory, dislocation are not required to leave the pillar and accumulated in pillar. Two mechanisms may be concurrence in the micro-sized sample. Jennings et al. [83] explained the stain-rate sensitivity phenomenon in the compression of copper nano-pillars by a transition from exhaustion hardening dominated to the starvation/surface-

source dominated. As focused ion beam (FIB) machining advances, micropillars can be readily prepared to investigate the size effects. Many in-situ SEM studies have been carried out with the help of FIB. Both Kiener [84] and Dou [85] have reviewed the size-dependent compressive strength of various metal pillars.

The stress field generated by a dislocation is modified near a free surface, leading to extra forces acting on the dislocation, i.e. image force [86]. The image force caused by dislocation-surface interaction is negligible for bulk sample but becomes influential for micro-sized sample when surface area increases. The normal and shear stress at a free surface are zero since no reaction forces provided outside the surface. An imaginary dislocation of opposite sign is introduced outside the surface at symmetric position to simulate the image force. The forces acting on the dislocations from the surface are: $F_x = -\frac{Gb^2}{4\pi d}$, $F_x = -\frac{Gb^2}{4\pi(1-\nu)d}$, for screw and edge dislocation respectively, where d is the distance from dislocation to the free surface. Thus, dislocations are attracted to the surface. The real situation will be more complex involving curved dislocation, dislocation loops and dipoles, etc.

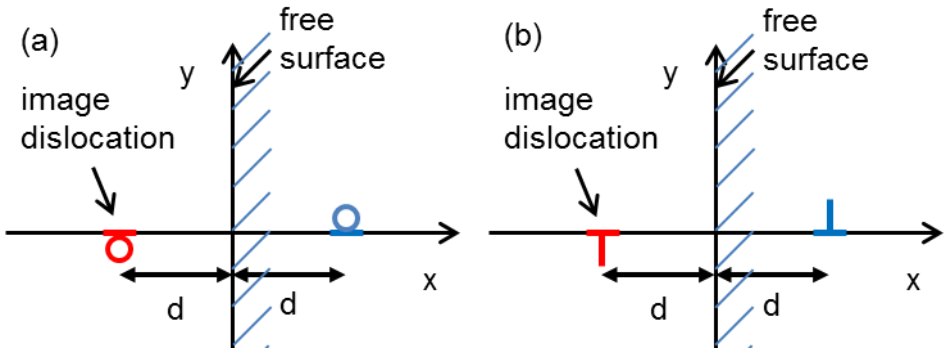

Figure 2.7 Schematic image force models for (a) screw dislocation (b) edge dislocation.

2.3.2. In-situ TEM tests

Most of the post-mortem TEM study lack of the spatial and the time resolution to investigate the dynamic process. In contrast, In-situ TEM studies offer the opportunity to observe the dynamic response of materials subjected to external stimuli, such as temperature, pressure etc. Many efforts have been made to develop the technique of in-situ TEM test [70, 87-89], and quantitative In-situ TEM compression test is an important branch.

Visualization is an important aspect of in-situ TEM tests. Hirsch et al. [90] and Whelan et al. [91] were first to observe dislocation movement in TEM in 1950's. The unexpected dislocations in the Al foil were induced by the locally heating due to a sudden flux of electron and emitted from a sub grain boundary then cross slipped between two planes [90]. In the 1960s and 1970s, with the help of high voltage TEMs (≥1MeV), several research groups investigated dislocation behaviours in thick specimens using custom-made straining holders [92]. Various approaches exist in in-situ TEM mechanical tests: simple mechanical actuation [93, 94], the miniaturization of MEMS [95] and with coefficients of thermal expansion[96]. Combined with MEMS and nano devices [70, 87, 89] which can apply external stimuli and simultaneously collect quantitative data, in-situ TEM study investigates the behaviour of materials and the deformation structures in low rate deformation.

Couret et al. [88, 93] used a straining holder to observe dislocation motion in polycrystalline samples. Using the same technique, Castany et al. [94, 97, 98] carried on a large amount of research on the dislocation mobility in a Ti64 alloy. Lee et al.

[99] has studied the passage of dislocations across grain boundaries. Although relatively large area could be investigated in their research, the mechanical response of material could not be directly linked to the dynamic microstructure evolution limited by the technique. Also, the very rigid displacement transmission allows to deform samples since thin area easily propagates cracks which increase the probability of brittle failure [87].

Quantitative in-situ TEM mechanical tests are able to investigate the mechanical response of materials with the simultaneous imaging of the deformation microstructure evolution instead of static results [100]. The nanoindentation tips attached on top of piezo-actuated holder can be accurately controlled to deform metals [87]. Minor et al. [101, 102] used quantitative in-situ TEM to investigate the dislocation motion and plastic deformation behaviours of micro-sized sample in different materials and confirmed dislocation exhaustion theories [102]. However, the dimension range accessible for pillars is more restricted for this technique than straining holder. The FIB preparation induces many damages on the surfaces which can influence the mechanical response of pillars [103]. The roughness of contact surface of the probe and pillar also affect the deformation.

In-situ TEM observation of dislocation has been studied for more than 60 year. Significant progress has been made thanks to the improved sample geometries, precise load controller and the high resolution force and displacement measurement. Furthermore, besides the basic material information like strength and ductility, some

specific in-situ experiments can provide other mechanical properties like fracture toughness. Although there are some breakthroughs in the technology, the application of in-situ experiments to predict the microscopic behaviour of material is still limited by stringent processing requirement, hard application of external stimuli, high resolution imaging and data capture. Significant challenges associated with the preparation, handling and testing of small volumes of material.

Chapter 3. Experimental procedure

3.1. As-received sample

The as-received material (Figure 3.1) was an extruded Ti64 rod with a diameter of 25 mm. All the specimens used in this project were cut from this rod.

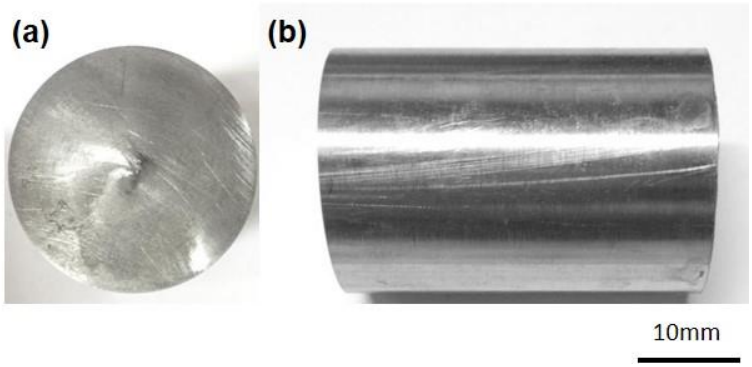

Figure 3.1 As-received Ti64 rod (a) cross section and (b) side view

3.2. Heat treatment

The as-extruded Ti64 rod was heat-treated in a Pyro Therm vacuum furnace. The heat treatment procedure is shown in Figure 3.2. The as-received sample was cut into small cubes with the dimensions of 5×5×8 mm, annealed at 1050 ℃ for 180 min and cooled at a rate of 0.5 ℃/min. The Beta annealing was performed at temperatures slightly above the β transus in order to enlarge grain size and reduce dislocation density.

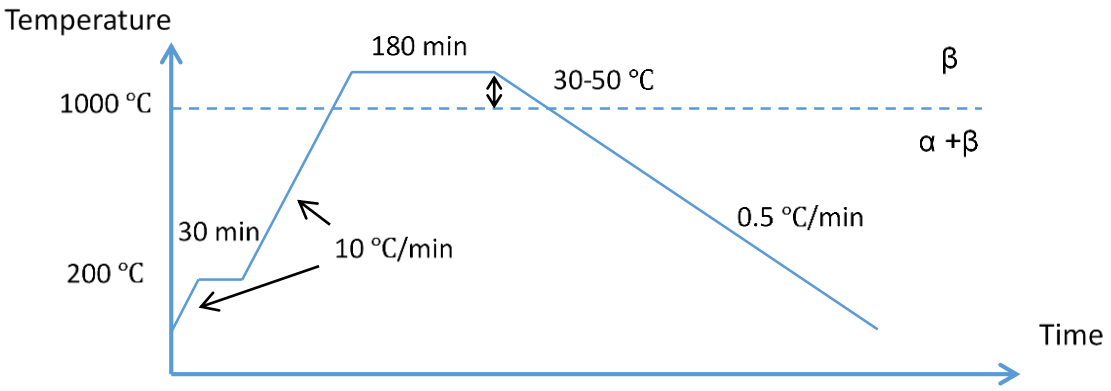

Figure 3.2 Schematic processing route

3.3. Compression test

Compression tests of the heat-treated samples were performed on a Zwick/Roell materialprufung materials testing system at room temperature. The tests were carried out at an initial strain rate of 1×10^{-3} s^{-1} to the permanent strain of about 2 % along the longest dimension. The loading direction was along the radial direction of the as-received sample which was perpendicular to the extruded direction.

3.4. Scanning electron microscopy (SEM)

In this study, Philips XL30, JEOL JSM-7000F and Tescan Mira-3 SEMs were employed for investigating the microstructure, chemical composition and grain orientations of the specimen.

3.5. Electron backscatter diffraction

The micro-texture of the as-received rods and the orientation of selected colony for micro-pillar preparation were determined using the electron backscatter diffraction (EBSD) technique in a Tescan SEM. The pole figures were measured using HKL Channel 5 software.

3.6. Transmission electron microscopy

In this study, a JEOL-2100 TEM was used for both the dislocation analysis and the in-situ compression testing.

Foils for TEM sample preparation were cut by an electro-discharge machining (EDM) and mechanically ground down to 100 μm. After that, the specimens were prepared by twin-jet electropolishing and observed in the TEM operating at 200 kV.

During the in-situ testing, the motion of the dislocations was recorded using an Oriss 200 CCD camera at 15 fps. After in-situ testing, the specimens were taken off from the sample mount and analysed using a double tilt holder within the TEM.

3.7. In-situ compression in TEM

3.7.1. Sample preparation

The pillars for in-situ compression were prepared directly from a half 3 mm TEM disc, which was prepared following the conventional method. Pillars for the in-situ compression test were cut using a Quanta 3D FEG focused ion beam (FIB) microscope, as shown in Figure 3.3.

A group of pillars with the same orientation were fabricated (Figure 3.3b). The pillars typically have a rectangular cross section of 0.4 μm (thickness) x 1 μm (width) x 2 μm (length).

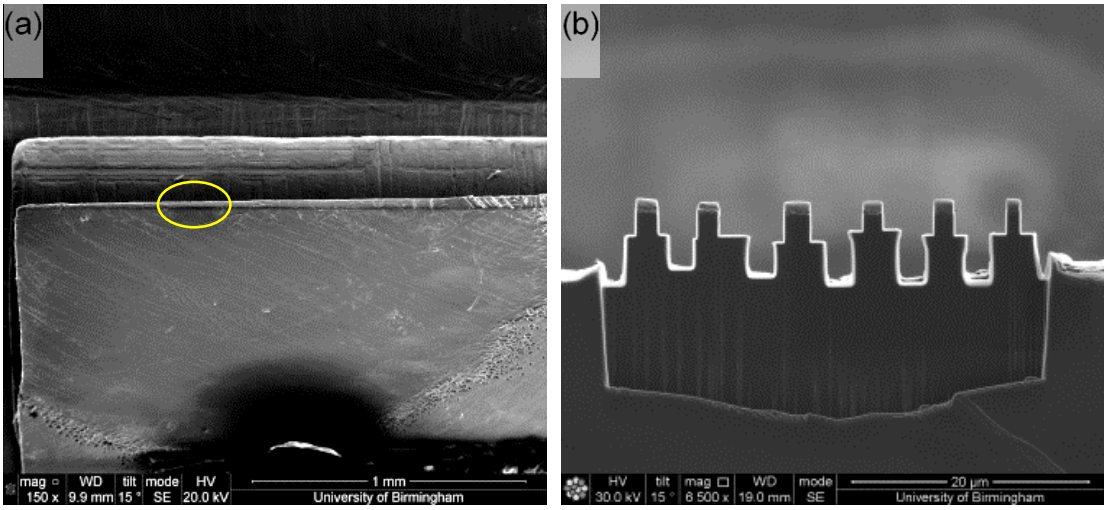

Figure 3.3 (a) SE image shows a half TEM disc. The circle marks the position where the 6 pillars shown in (b) were fabricated

A schematic diagram (Figure 3.4) illustrates the relative position between the sample mount, the pillars and the probe during the in-situ testing. The copper sample mount is specially designed for the in-situ test holder and has two screws through holes which can be fastened onto the holder. The half TEM disc was fixed to the sample mount using crystalbond. Colloidal graphite was used to cover the junction of the mount and the half TEM disc. The pillars were prepared after the half disc has been fixed onto the sample mount to improve the alignment between the pillar and the probe for compression.

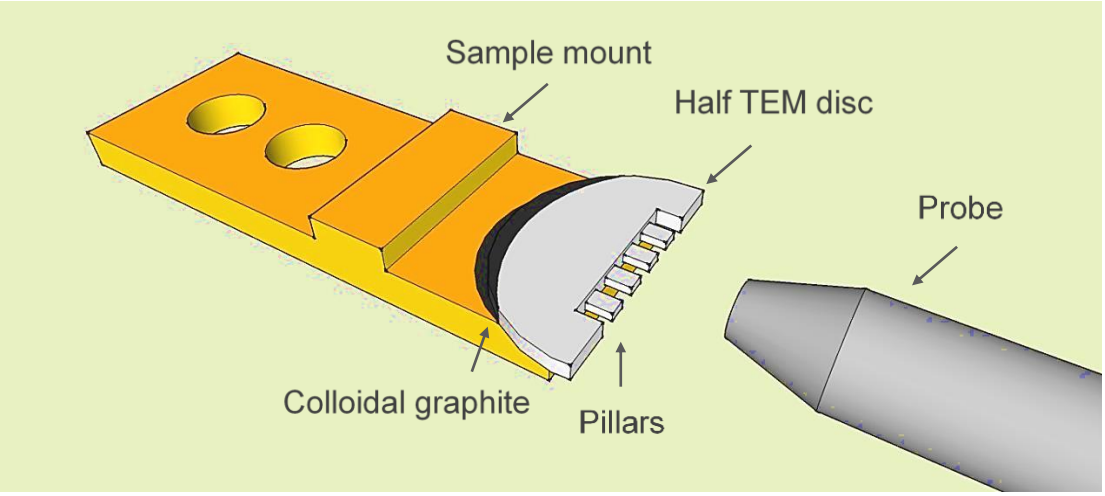

Figure 3.4 A schematic diagram illustrating the sample mount, pillars and probe.

A 38^{o} pre-tilt holder was used for the pillar preparation (Figure 3.5). The sample mount with the in-situ sample (Figure 3.5a) was fixed on the pre-tilt holder for FIB cutting. During the whole process of pillar preparation, the sample mount presented

as a reference to align the horizontal of the front edge of pillars and the vertical of sides of the pillars. Figures 3.5b and 3.5c are schematic diagrams showing the obverse and reverse positions used for FIB milling. At the obverse position (Figure 3.5b), the slope of the pre-tilt holder is parallel to the ion beam. Thus, the top and bottom surfaces of the pillar were milled parallel to the top and bottom flat surfaces of the sample mount. The obverse position is used to thin the pillars. After 180° rotation, the top surface of the specimen was facing the ion beam. After tilting by 14°, the reverse position (Figure 3.5c), the front edge of the pillar was milled parallel to the front surface of the sample mount. At the reverse position, the length and width of pilllars are shaped.

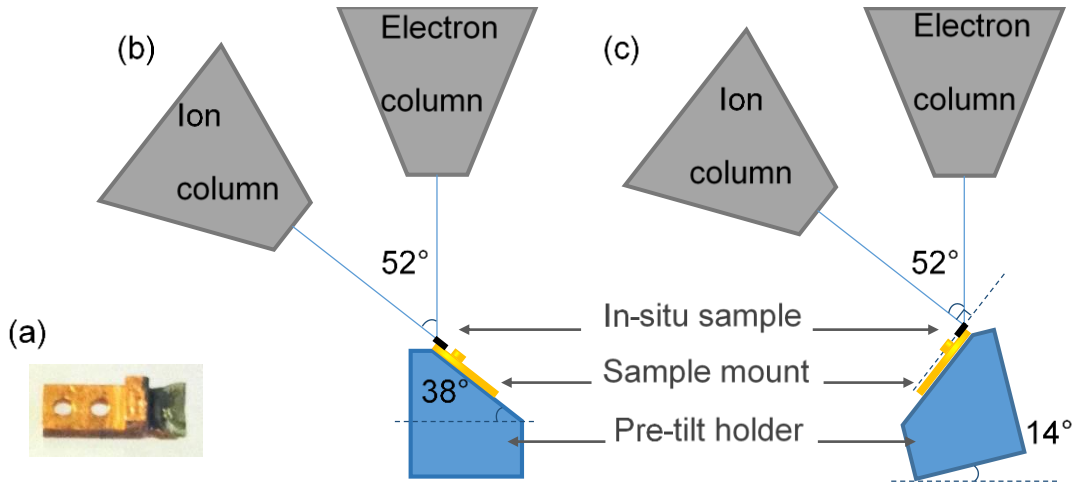

Figure 3.5 (a) Sample mount with the in-situ sample. (b) and (c) are the obverse and reverse positions for FIB milling. The in-situ sample, sample mount and pre-tilt holder are labelled for two positions.

In-situ test pillars were produced from the annealed specimen as well as the compressed specimen. To ensure the shape of the pillars and to reduce the beam damage, the obverse and reverse positions were used alternately while milling. The main milling process was performed at 30 kV. The ion beam current was reduced from 50 nA to 30 pA with decreasing sample size. Final polishing used a 5 kV beam and 7.7 pA current. Figure 3.6 shows sequential images of the pillar preparation process: (a) At the reverse position, clean the left and right sides of the interested area and mill the front surface flat using a large beam current. (b) Deposit Pt on the top of the front surface where the pillars will be cut at the obverse position. (c) At the obverse position, thin the selected area to 3 μm using 3 nA. (d) At the reverse position, roughly cut the pillar shape with dimensions 3 μm x 6 μm using 1 nA ion beam current. (e) At the obverse position, thin the pillars to 1 μm using 0.5 nA. (f) At the reverse position, cut the pillars roughly to 1 μm x 2 μm (besides the coating) using 0.1 nA ion beam current. (g) At the obverse position, finally thin the pillars to 400 nm using 50 pA. (h) At the reverse position, cut the top coating using 30 pA. The final size of the pillar is 1 μm x 2 μm. (i) Final cleaning at the obverse position.

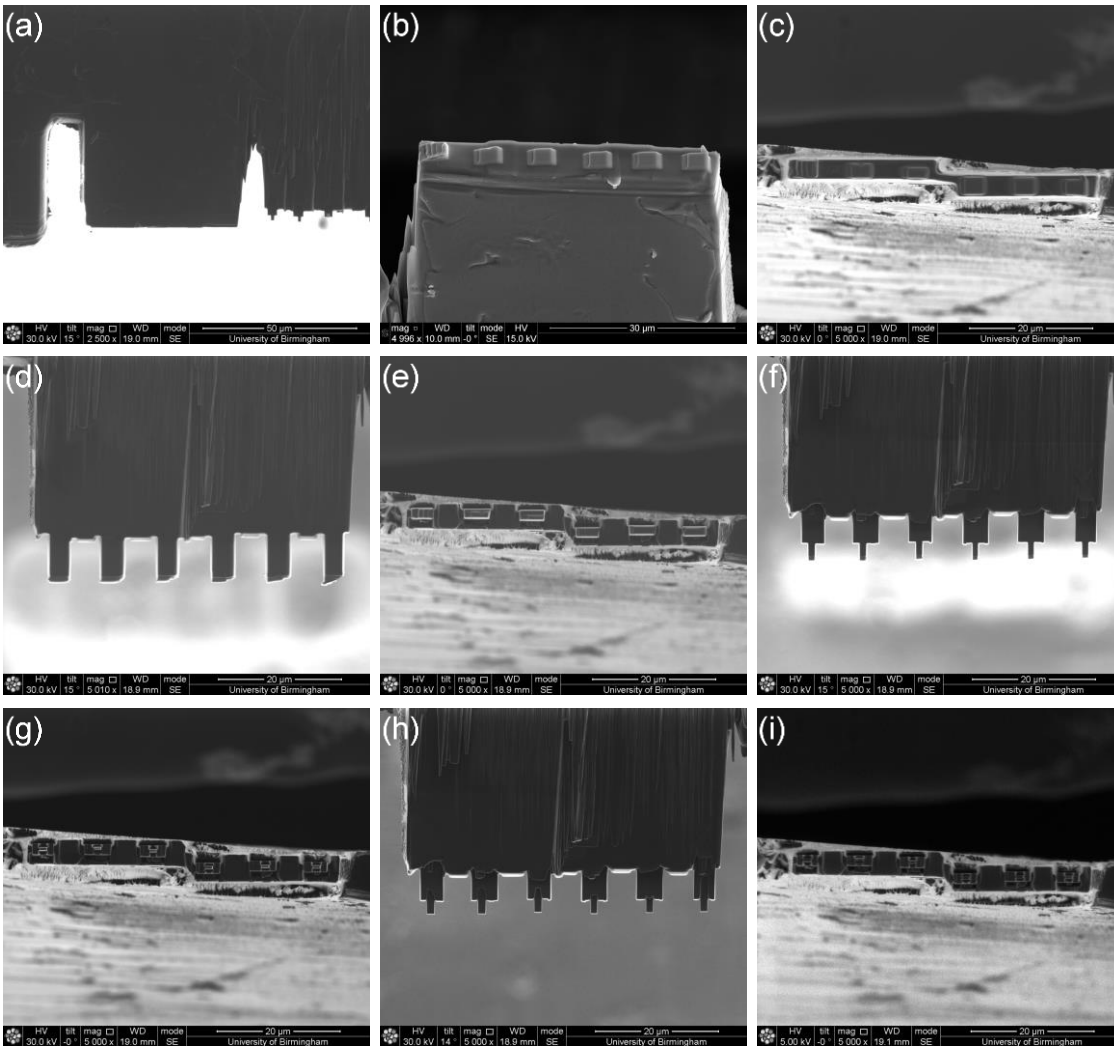

Figure 3.6 Sequence images of the in-situ sample preparing process: (a) Ion-beam image of the selected area with the front surface flat. (b) SEM image of the selected area with Pt-coating on the top. (c) Ion-beam image of the selected area after bulk thinning. (d) Ion-beam image of pillars after bulk milling. (e) Ion-beam image of the pillars after intermediate thinning. (f) Ion-beam image of the pillars after intermediate milling. (g) Ion-beam image of the pillars after final thinning. (h) Ion-beam image of the pillars after final milling. (i) Ion-beam image of the pillars after final cleaning.

3.7.2. In-situ testing

In-situ compression testing was carried out at room temperature on a JEOL-2100 TEM operated at 200 kV with a Hysitron PI 95 TEM Pico-Indenter (Figure 3.7a). The

maximum force for indentation is 3.2 mN. The sample to be tested was mounted and fixed to the front of the holder. Figure 3.7b is a bright field image showing the setup ready to be tested in the TEM. Compression video and load-displacement data were recorded by the Hysitron control system.

Figure 3.7 (a) The in-situ compression test holder - Hysitron PI95 TEM Pico-Indenter (b) TEM image of a pillar ready to be tested

The straining holder employed is a single-tilt holder. The displacement is controlled by a three-axis coarse positioner, a 3D piezoelectric actuator for fine positioning and a transducer with the electrostatic actuation. The three-plate capacitive displacement sensor provides high sensitivity, a large dynamic range and a linear force or displacement output signal [104]. Since the holder is contained in a chamber evacuated to a high vacuum, the probe undergoes an undamped motion when moving inside the TEM chamber. Q-control is used to actively dampen transducer oscillations during compression [104]. Both load-control and displacement-control, which can precisely achieve the desired force or displacement, can be used on this

holder. The typical loading rates used during in-situ tests were 5-10 μN/s or 1 nm/s corresponding to two control modes. The mechanical responses are different with respect to the control mode: strain bursts and load drops [101, 105], respectively, in responding to sudden plastic deformation.

3.7.2.1. Alignment of the probe and the pillar

Since a TEM image is a projection of the sample, it doesn't show the height difference (i.e. parallel to the beam) between the probe and the pillar, so alignment is necessary to ensure that the probe can compress the pillar properly during the test, in order to avoid bending. As shown in the schematic diagram (Figure 3.4), the ideal position is where the front surface of the pillar faces the centre of the front plane of the probe. During the whole process of in-situ testing, extra care was taken in the alignment to minimize any tangential force which may cause undesired lateral bending. The SEM image in Figure 3.8 shows an example of a fractured pillar under lateral load, where observation and analysis of dislocations were not possible.

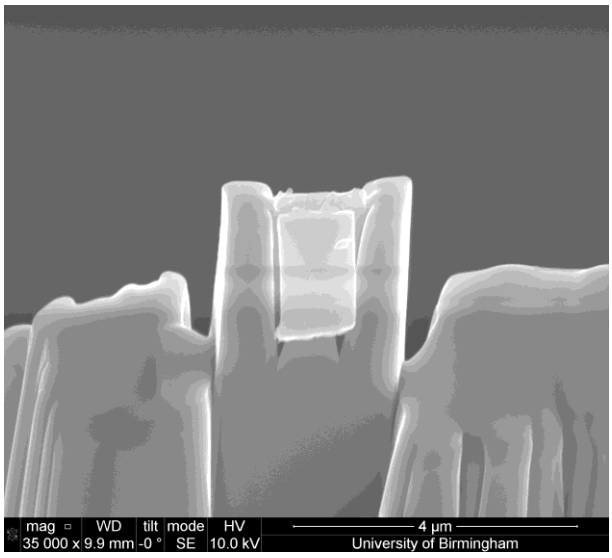

Figure 3.8 SEM image of a fractured pillar under lateral load

The image of pillar was first focused and then the position of the probe was adjusted mechanically to be roughly at the same height according to the image focus. Then the probe was moved to approach the pillar gently using the piezo controls.

Figure 3.9 shows a schematic diagram of the alignment at 0˚ in the two-dimensional drawings. Figure 3.9(a - c) are the plan views of the probe and the pillar. Figure 3.9 (d - f) are the side views. The blue pattern in the diagram represents the probe and the yellow pattern represents the pillar. x, y, z represent three motion axes, horizontal, vertical and indentation direction, respectively corresponding to the probe. The height of the probe is adjusted by the y axis control of the holder.

The probe was moved along the y axis and the y values when the probe just touched the upper (Figure 3.9a and d) and lower (Figure 3.9b and e) surfaces of the pillar were recorded. The averaged y value was used for the compression (Figure 3.9c and f). In other words, the axes of both the probe (z_1) and the pillar (z_2) are in one line.

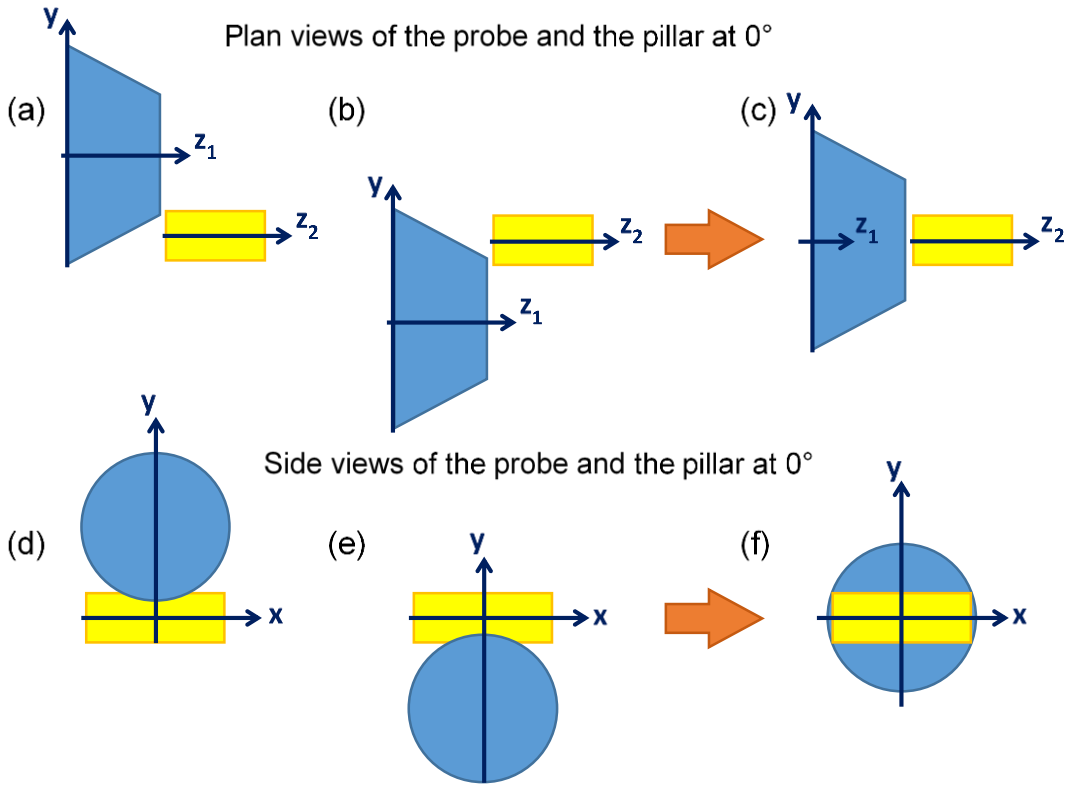

Figure 3.9 Alignment of the probe and the pillar at 0˚ (a-c) show the plan views of the probe (trapezium) and the pillar (rectangle). (d-f) show the side views of the probe (circle) and the pillar (rectangle). The probe just touched the (a, d) upper and (b, e) lower surfaces of the pillar. (c, f) show the optimized vertical position.

Similarly, for when the holder was tilted to any other orientation, where the in-situ compression tests were performed, a schematic diagram of the alignment is shown in Figure 3.10. The height of the probe is determined by both x and y axes. Therefore, both x and y values needed to be adjusted in this case.

It is worth noting that tilting the holder would change the relative position between the probe and the pillar. Even after each compression test, the relative position might be slightly changed. So before each test, the probe needed to be adjusted again.

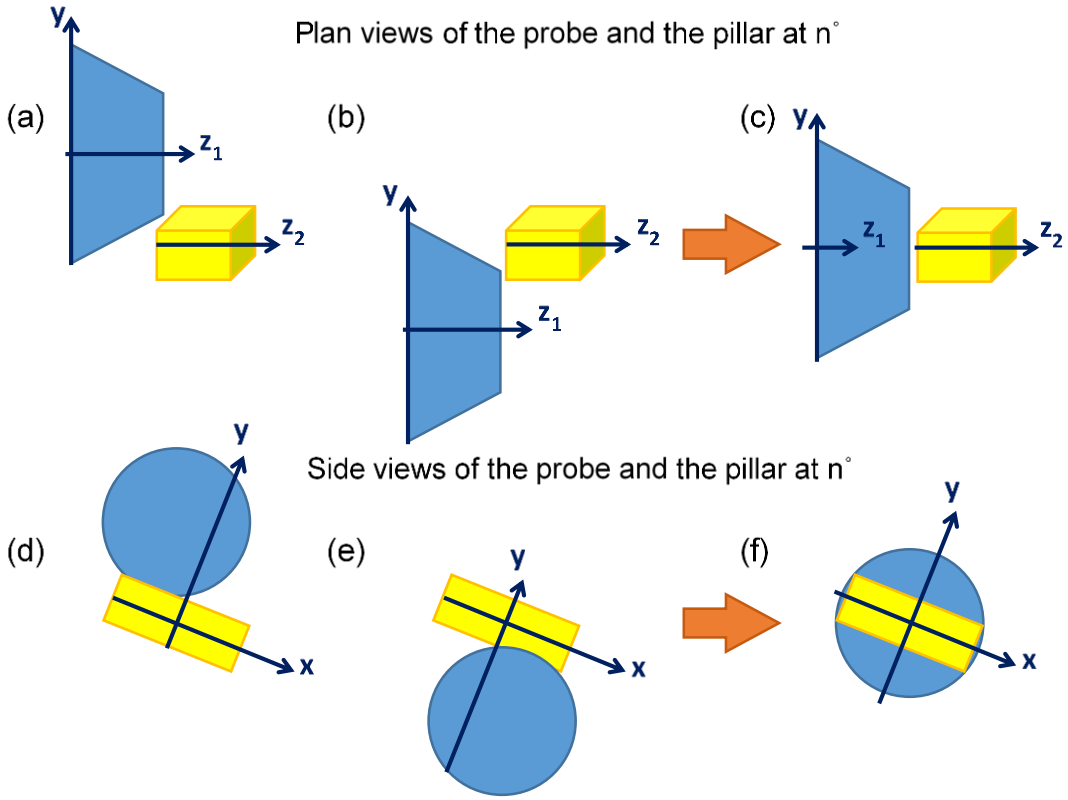

Figure 3.10 Alignment of the probe and the pillar at another tilt of n° (a-c) are the plan views of the probe (trapezium) and the pillar (cuboid). (d-f) are the side views of the probe (circle) and the pillar (rectangle). The probe just touched the (a, d) upper and (b, e) lower surfaces of the pillar. (c, f) show the optimized position.

3.7.2.2. Loading direction determination

The precise orientation of the pillars was determined from the TEM diffraction patterns. An example, Figure 3.11 shows a bright field image of the pillar and two diffraction patterns taken from different zone axes. When the probe and the pillar have been aligned, the compression loading direction was along the long side of the pillar and perpendicular to the contact surface between the probe and the pillar.

Since in-situ tests were carried out using the single tilt PI95 holder, beam directions were always perpendicular to the loading direction. Thus, the contact surface which contains the two beam directions B_1 (Figure 3.11b) and B_2 (Figure 3.11c) can be determined as: $P_0 = B_1 \times B_2$. The loading direction was the normal to P_0. The following formula can be used to work out the direction $[u, v, t, w]$ corresponding to the normal to plane (h, k, i, l): [31]

$$u = h, v = k, t = i, w = \frac{3a^2}{2c^2}l$$

where c/a is the axial ratio of the α phase.

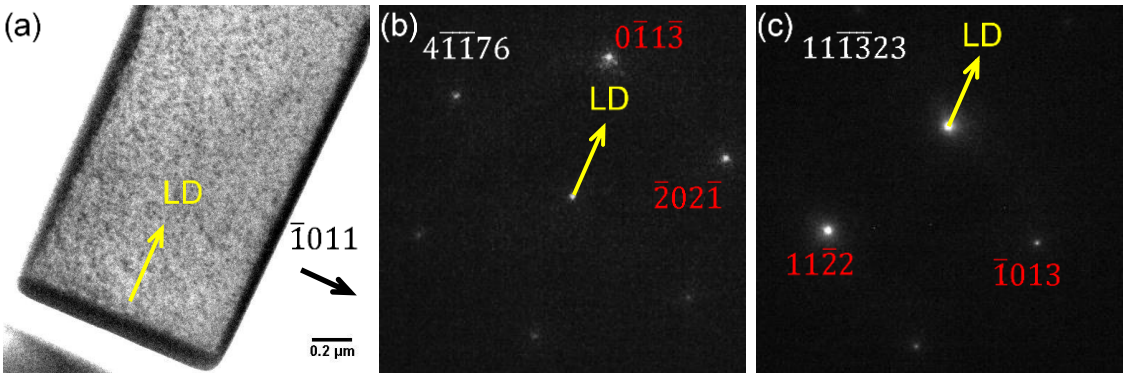

Figure 3.11 (a) Bright field image of the pillar with $\bar{1}011$ reflection, $\mathrm{BD} \sim [2\bar{3}11]$; (b) and (c) are the diffraction patterns taken along two zone axes. The arrows indicate the loading direction.

All the contact surfaces between the probe and the pillars and the loading directions involved in the in-situ TEM compression tests were determined by the above method.

Chapter 4. Microstructure of bulk Ti64

4.1. As-received specimen

4.1.1. Microstructure of the as-received specimen

Figure 4.1 shows SEM images obtained from the as-received alloy. The dark regions were identified as α phase by EDS, while the bright regions were β phase. The extrusion direction (ED) is denoted by the arrow in Figure 4.1b. After the extrusion, the rod exhibits a bimodal microstructure in general.

The microstructure of the as-received alloy is different in transverse and longitudinal sections as shown in Figures 4.1a and 4.1b. In cross section, the fine grains tend to present as a globular microstructure. In the longitudinal section, most of the primary-α (α_p) phase is stretched and displays a strip-like configuration along the extrusion direction. The remanent β phase is distributed along the α phase boundaries. In between the elongated grains are areas with α_s/β lamellar colonies, which are formed from a temporarily transformation into β phase during the heating and extrusion.

Structural differences also exist between the periphery and the centre of the rod as shown in Figure 4.2a. The grains at the periphery (Figure 4.2b) were highly elongated. A typical bi-modal microstructure composed of α_p and α_s/β lamellar colonies is present near the axis of the rod (Figure 4.2d). The region between them consists of less stretched grains (Figure 4.2c).

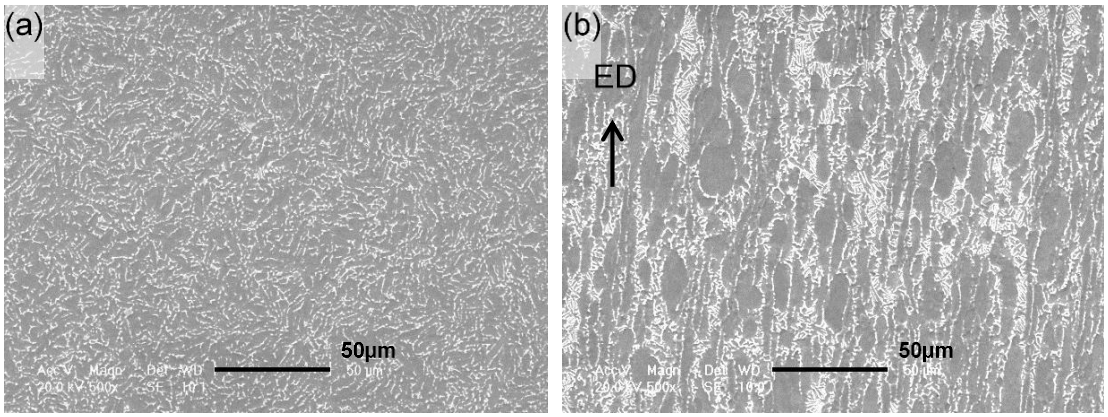

Figure 4.1 Microstructures of the as-received alloy (a) Fine grains in cross section and (b) stretched α_p and α_s/β lamellae in longitudinal section

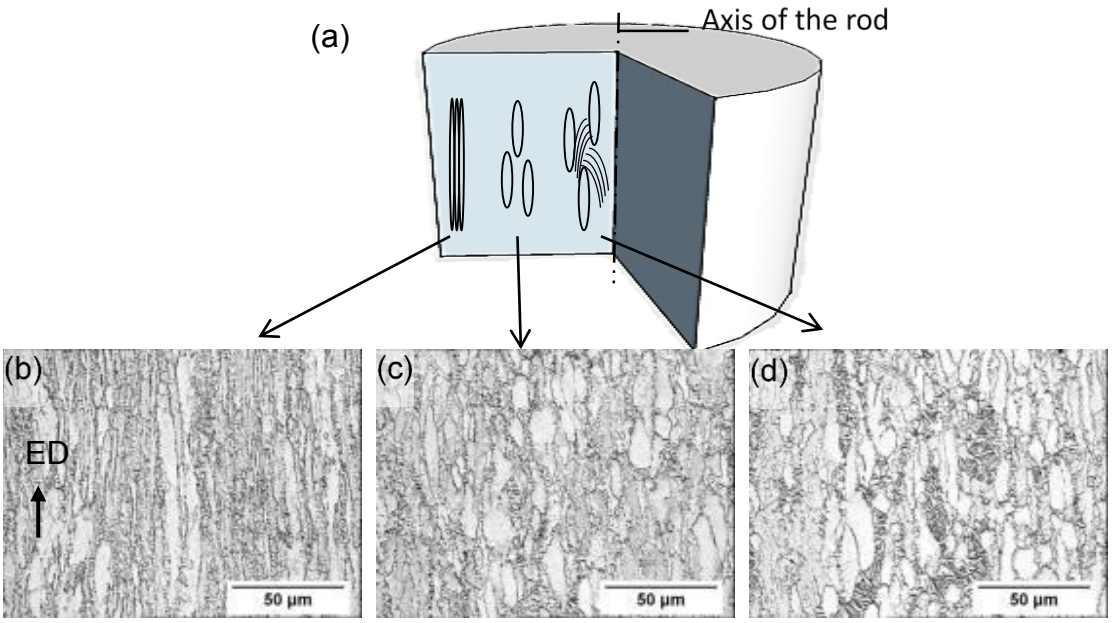

Figure 4.2 (a) Schematics of the longitudinal section through the as-received rod and various microstructures across it: (b) spindly grains in outer part of rod (c) less stretched grains halfway across the radius (d) bi-modal distribution of α_p and α_s/β lamellar colonies in the centre

The texture of the as-received sample is shown in Figure 4.3. Since the EBSD map was performed on the cross section of the rod, the basal planes are almost parallel to the extrusion direction with a rotation around the longitudinal axis of the rod (Figure 4.3a). There are intensities in the range of 12°-42° and 80°-90° in the $\{11\bar{2}0\}$ pole figure (Figure 4.3b). The $\{10\bar{1}0\}$ pole figure has the highest texture intensity at 0° (Figure 4.3c). The intensity decreases from 0° to 22°. Another high intensity region is at 45°-70°. The texture of the as-received specimen is similar to that of the extruded rods at 960°C [16].

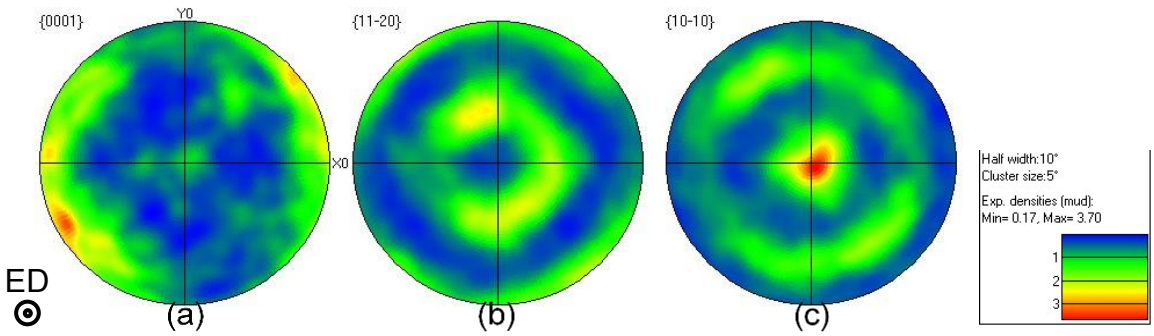

Figure 4.3 Pole figures of as-received rods (a) $\{0001\}$ pole figure (b) $\{11\bar{2}0\}$ pole figure (c) $\{10\bar{1}0\}$ pole figure.

4.1.2. Chemical composition and phase proportions of the as-received specimen

The area fraction of β phase in the as-received specimen is approximately 15% as averaged from 15 secondary electron (SE) images at a magnification of 1000x.

The chemical composition of the α and β phases as measured by EDS at 15kV is shown in Table 4.1, which was obtained from nine and seven measurements in the black and white areas, respectively. The mean values are together with the standard deviation. Compared with the measurements of Elmer [106], the chemical composition of the α phase is similar, while the content of V in the β phase is lower than expected. One possible reason is that the small size of the β phase, making the X-ray photons acquired come partially from the α phase.

Table 4.1 Chemical composition of the α and β phases (wt%)

Element	Al	V	Ti	Fe
α phase	6.59±0.15	2.52±0.39	90.88±0.28	-
β phase	4.6±0.27	11.14±1.6	83.14±1.92	1.31±0.32

4.1.3. Dislocations in the as-received specimen

The as-received specimen has fine subgrains and high density of dislocations, which makes dislocation analysis hard to perform. Figure 4.4 shows a relatively low dislocation density area in the as-received sample. Two different diffraction vectors ($\bar{1}010$ and $01\bar{1}0$) have been chosen to produce two bright field TEM images of the same field of view. Arrows 1, 2 and 3 in the images represent three groups of screw dislocations. By dislocation invisibility analysis, their Burgers vectors were <a> type (see caption).

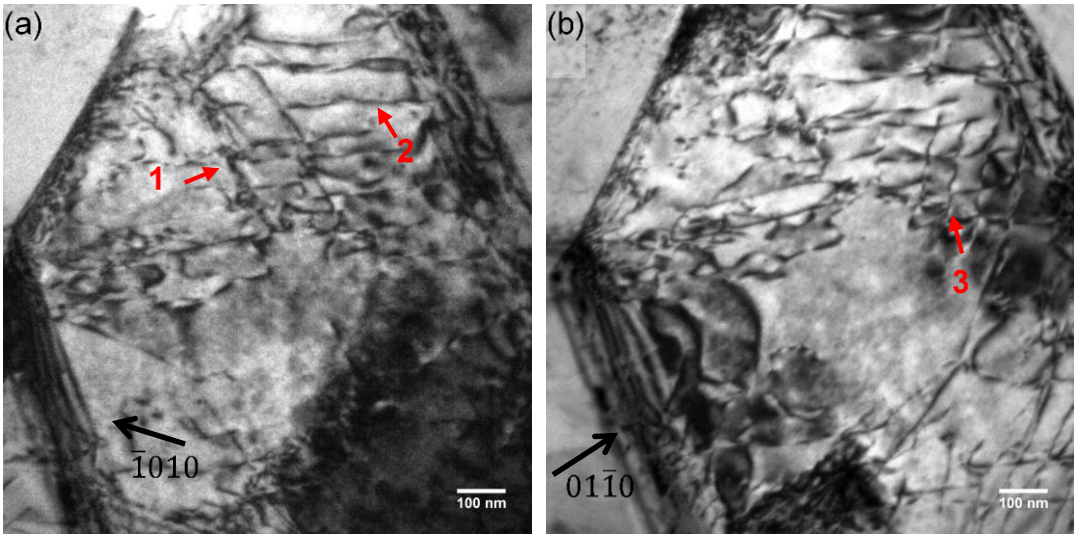

Figure 4.4 Bright field TEM images with (a) $\mathrm{g} = \bar{1}010$ and (b) $01\bar{1}0$, beam direction ~ $[0001]$. The Burgers vectors of the dislocations labelled 1, 2 and 3 are $\frac{1}{3}[\bar{2}110]$, $\frac{1}{3}[11\bar{2}0]$ and $\frac{1}{3}[1\bar{2}10]$, respectively.

The density of <c+a> dislocations observed in the as-received specimen was much lower than that of <a> type. Figure 4.5 shows the same area imaged with different g vectors. When $g = \bar{1}01\bar{1}$ (Figure 4.5a), several dislocations were visible in the selected area. All <a> dislocations were invisible when $g = 0002$. Thus, the dislocations labelled 1, 2 and 3 in Figure 4.5b have a Burgers vector of <c+a> type.

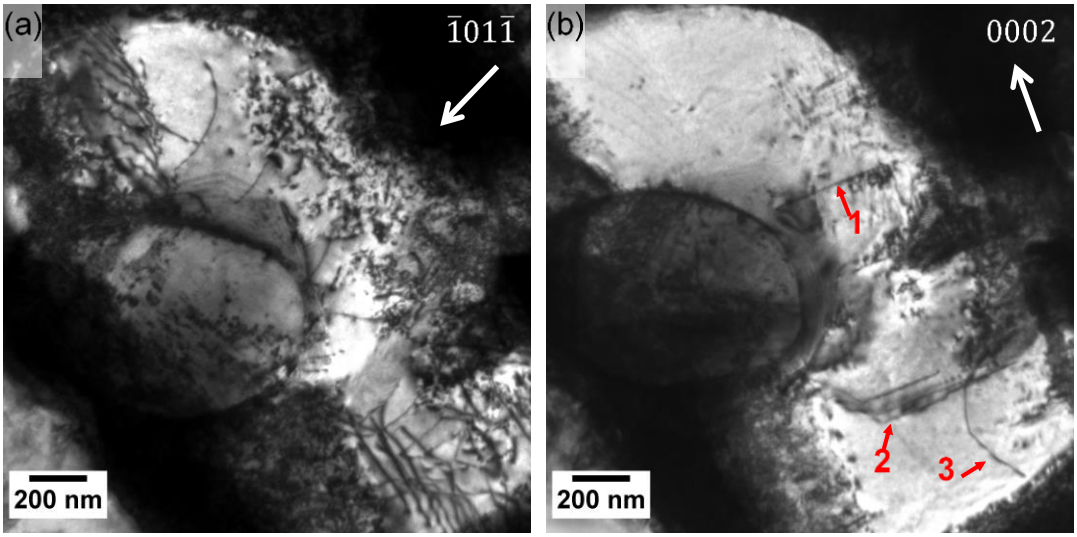

Figure 4.5 Bright field TEM images with (a) $g = \bar{1}01\bar{1}$and (b) 0002, beam direction ~ $[1\bar{2}10]$. The dislocations labelled 1, 2 and 3 are <c+a> type.

4.1.4. Conclusions

The microstructure of the as-received specimen is inhomogeneous, consisting of the elongated grains at the outside of the rod, less stretched grains mid-radius and bi-modal microstructure in the centre. The as-received sample generally has subgrains and high density of dislocations.

<a> dislocations as well as <c+a> dislocations were observed in the as-received sample. The density of the <c+a> dislocations in the as-received specimen was much lower than that of the <a> type.

4.2. Annealed specimen

4.2.1. Microstructure of the annealed specimen

Figure 4.6b is an SEM image obtained from the annealed sample. α laths are regularly separated by discontinuous thin β laths. Compared with the extruded specimen (Figure 4.6a) at the same magnification, the fine elongated grains have grown into millimetre-scale sized α/β lamellae.

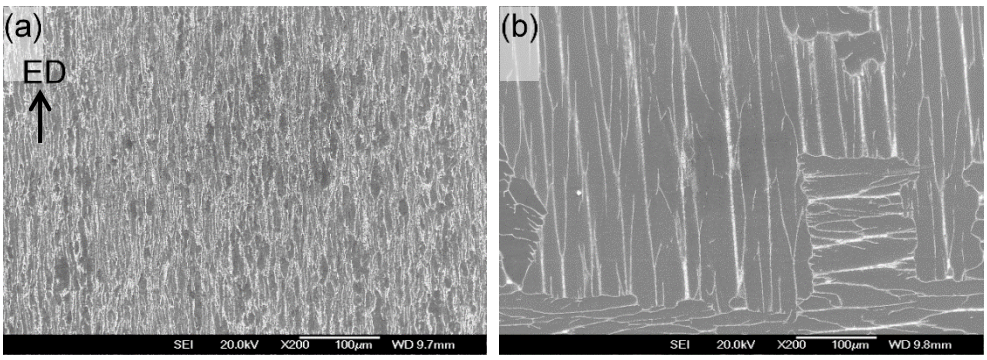

Figure 4.6 SEM images obtained from (a) the as-extruded sample and (b) the annealed sample

Figure 4.7 illustrates the same area of α phase in the annealed sample using different reflections in a TEM specimen. The grown-in dislocations are mostly arranged into two LAGBs. The dislocation density is relatively low. With the $000\bar{2}$ reflection (Figure 4.7b), all the dislocations retaining strong contrast are <c+a> dislocations. The main array of dislocations, labelled as 1 in Figure 4.7b, constitutes a low angle grain boundary. It can be inferred from Figure 4.7b that the boundary, although not flat, is close to the basal plane. Dislocations within the boundary are sometimes lightly staggered with respect to each other, which indicates that they lie on different layers of the basal plane.

(a)

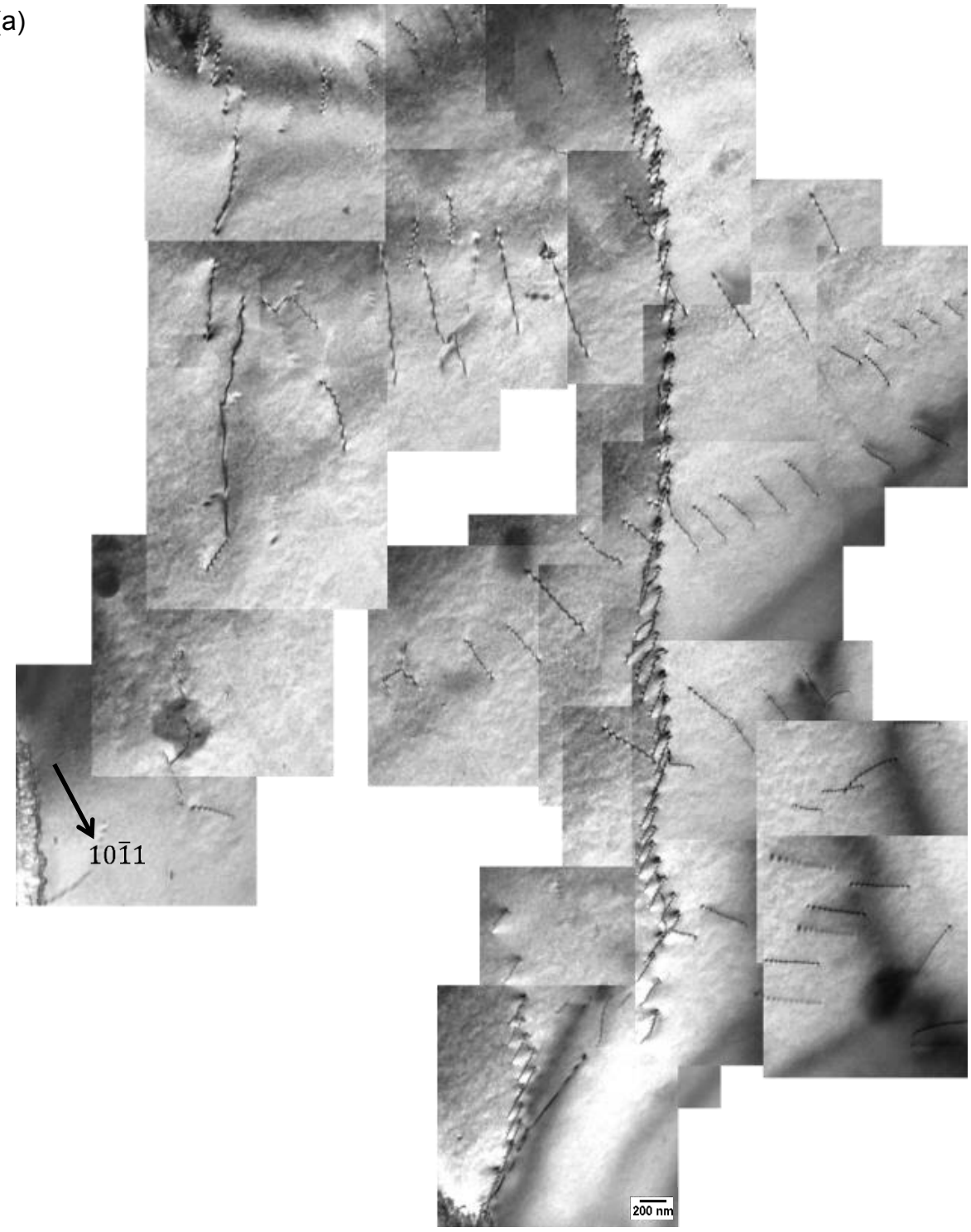

(b)

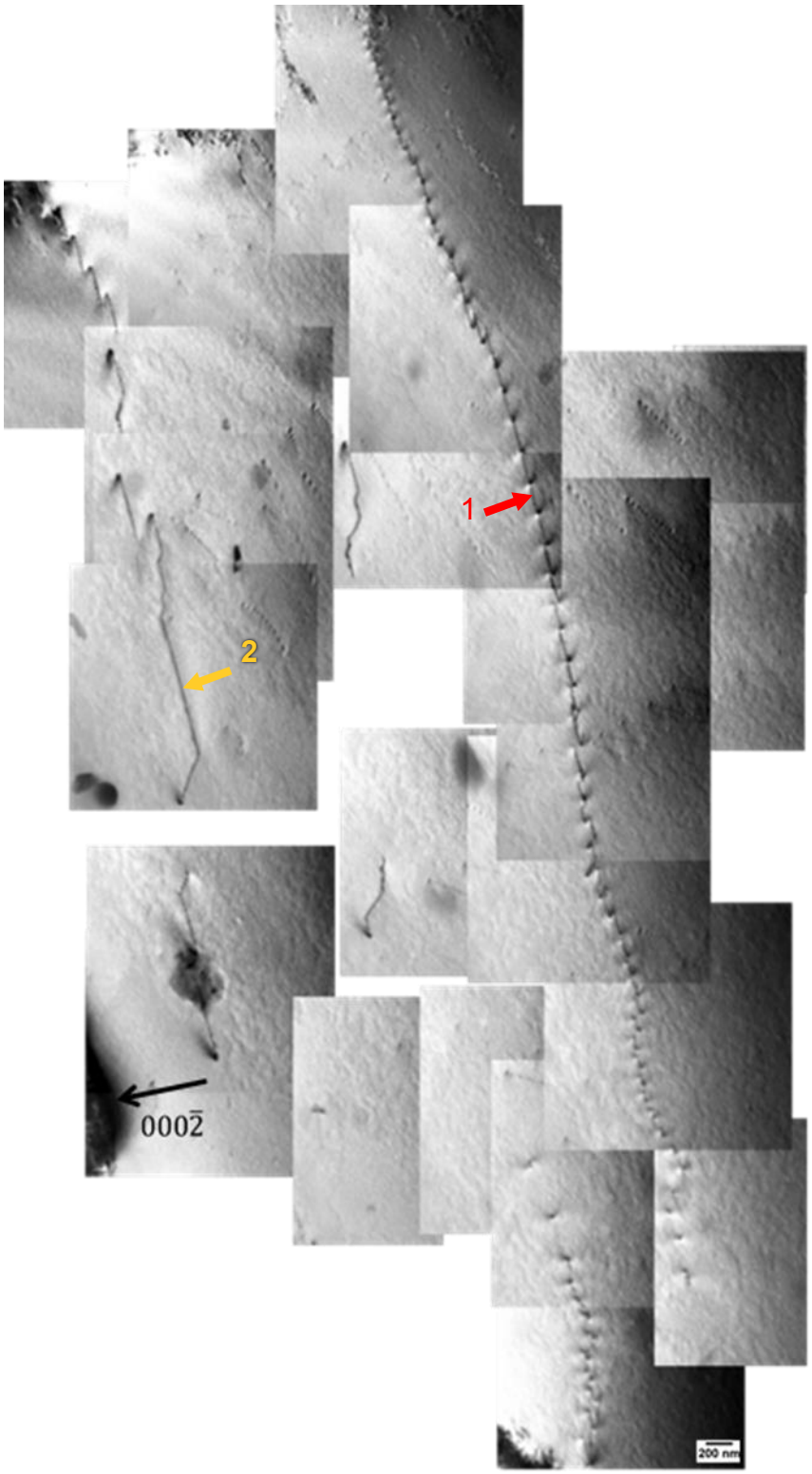

Figure 4.7 Bright field images showing grown-in dislocations in the annealed sample (a) $g = 10\bar{1}1$, $BD \sim [1\bar{3}21]$ (b) $g = 000\bar{2}$, $BD \sim [1\bar{2}10]$

4.2.2. Low angle grain boundary

LAGBs have been repeatedly observed in the annealed sample. These low angle grain boundaries represent most of the grown-in dislocations in the annealed sample.

4.2.2.1. <c+a> LAGB

Figure 4.8 shows the same prominent low angle grain boundary as in Figure 4.7a&b formed from <c+a> dislocations and imaged with the $10\bar{1}\bar{1}$ reflection. Apart from the <c+a> dislocations, there are also several <a> dislocations trapped as shown by arrows in Figure 4.8.

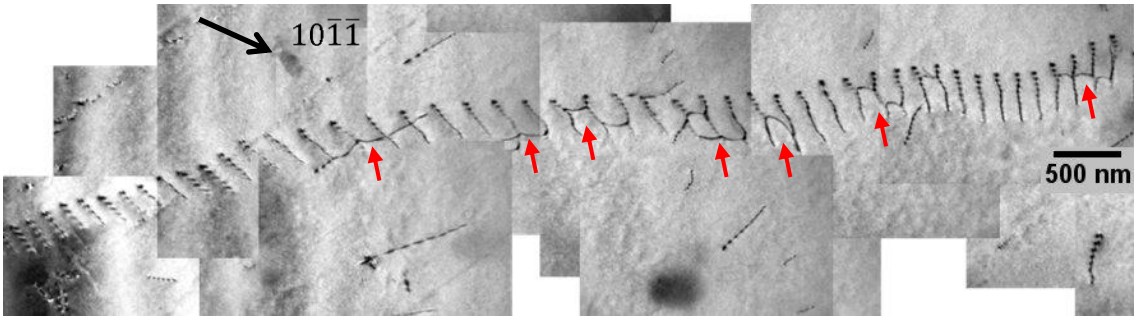

Figure 4.8 The low angle grain boundary from Figure 4.7 imaged with the $10\bar{1}\bar{1}$ reflection, $\mathrm{BD} \sim [1\bar{1}01]$

These dislocations have been analysed using the $\mathrm{g} \cdot \mathrm{b} = 0$ invisibility criterion. A few dislocations (labelled 1-7 in Figure 4.9) are included as an example. The same dislocation is marked using the same number under different reflections.

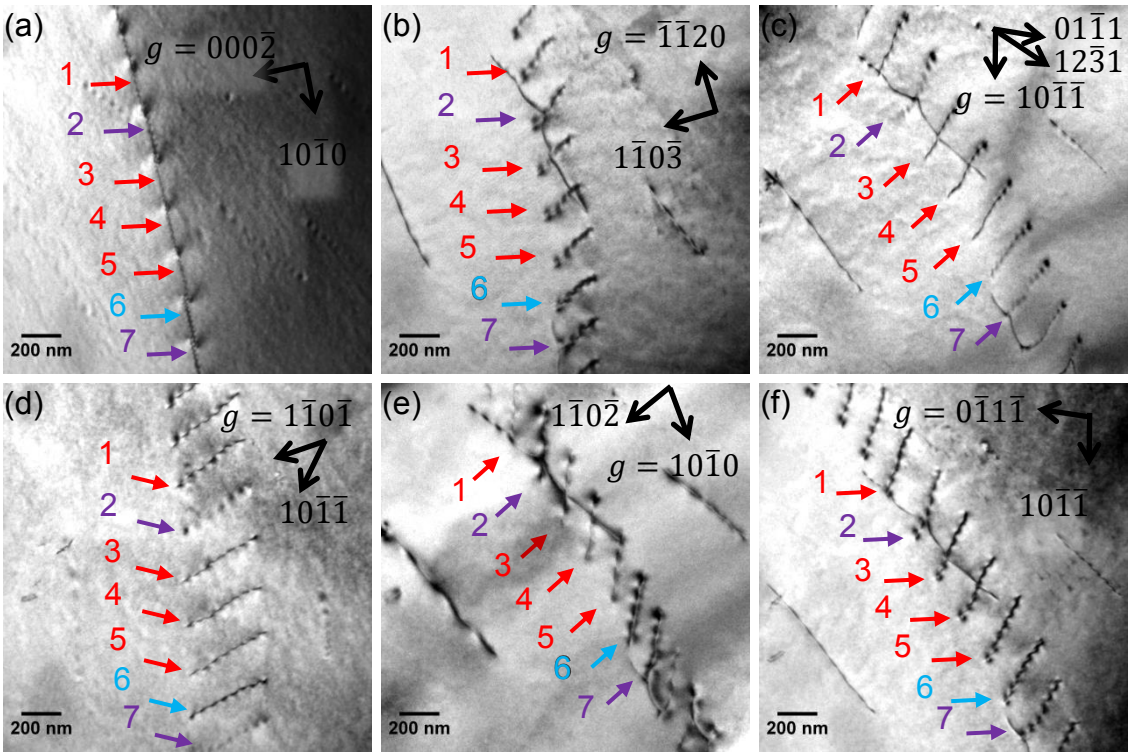

Figure 4.9 (a) to (f) show the same area of the LAGB imaged using different g vectors. (a) $g = 000\bar{2}$,$BD \sim [1\bar{2}10]$ (b) $g = \bar{1}\bar{1}20$, $BD \sim [3\bar{3}02]$ (c) $g = 10\bar{1}\bar{1}$, $BD \sim [1\bar{1}01]$ (d) $g = 1\bar{1}0\bar{1}$,$BD \sim [2\bar{1}\bar{1}3]$ (e) $g = 10\bar{1}0$, $BD \sim [2\bar{4}23]$ (f) $g = 0\bar{1}1\bar{1}$, $BD \sim [1\bar{1}01]$

Using the $000\bar{2}$ and $\bar{1}\bar{1}20$ reflections (Figures 4.9a and 4.9b), all the dislocations retaining contrast (labelled 1-7) were identified as <c+a>. The dislocations labelled 2, 7 are out of contrast when $g = 10\bar{1}\bar{1}$ (Figure 4.9c) and $g = 1\bar{1}0\bar{1}$ (Figure 4.9d). Thus, they have a Burgers vector of $\pm\frac{1}{3}[2\bar{1}\bar{1}3]$. It is worth noting that these two dislocations with different Burgers vector from the dislocations around are precisely located at the position of the trapped <a> dislocations. Using the same condition, the dislocation labelled 6 is out of contrast when $g = 10\bar{1}\bar{1}$, but is in strong contrast when $g = 1\bar{1}0\bar{1}$. Therefore, the Burgers vector of the dislocation labelled 6 is $\pm\frac{1}{3}[11\bar{2}3]$. The

dislocations labelled 1, 3, 4 and 5 are out of contrast when $g = 10\bar{1}0$ (Figure 4.9e), but in contrast for $g = 0\bar{1}1\bar{1}$ (Figure 4.9f), $g = 10\bar{1}\bar{1}$ and $g = 1\bar{1}0\bar{1}$. The Burgers vector of these dislocations is therefore $\pm\frac{1}{3}[\bar{1}2\bar{1}3]$.

In the same LAGB, there is another type of dislocation with $\mathrm{b} = \pm\frac{1}{3}[1\bar{2}13]$ (labelled 8 and 9 in Figure 4.10). These dislocations are out of contrast when $g = 01\bar{1}1$ (Figure 4.10b) and $g = 1\bar{1}0\bar{1}$ (Figure 4.10c).

However, the above criterion of invisiblity is relative to some extent. Since these <c+a> dislocations are mixed dislocations, in most cases they still have residual contrast rather than being completely invisible when $g \cdot b = 0$. The contrast of dislocations labelled 8 and 9 in Figure 4.10b is relatively lower than the rest of the dislocations in the same image. The contrast of dislocations 8 and 9 is much weaker when $g = 01\bar{1}1$, while other dislocations lines are very clear. Combined with the contrast under other reflections and the possible $g \cdot b$ values in Table 4.2, dislocations 8 and 9 in Figure 4.10b are considered as invisible.

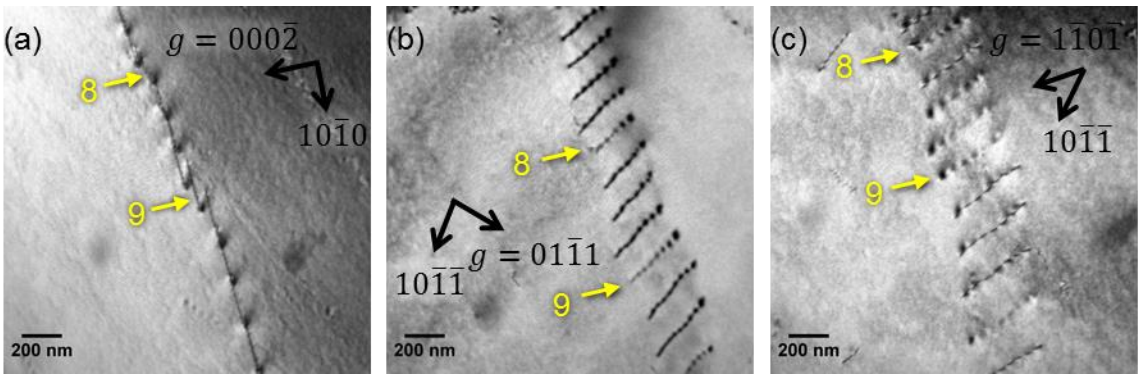

Figure 4.10 The Burgers vector of dislocations labelled 8 and 9 is $\pm\frac{1}{3}[1\bar{2}13]$. (a) $\mathrm{g} = 000\bar{2}$, $\mathrm{BD} \sim [1\bar{2}10]$ (b) $\mathrm{g} = 01\bar{1}1$, $\mathrm{BD} \sim [1\bar{1}01]$ (c) $\mathrm{g} = 1\bar{1}0\bar{1}$, $\mathrm{BD} \sim [2\bar{1}\bar{1}3]$

Table 4.2 summarises $g \cdot b$ for the various <c+a> dislocations and different g vectors. It helps to determine the Burgers vectors of dislocations with different contrast from the same reflection. In addition, the sense of the Burgers vectors of the dislocations in LAGB can be identified by the values of $g \cdot b$. Since the contrast at the two surfaces of all the dislocations in the LAGB is the same (Figure 4.7-Figure 4.10), the values of $g \cdot b$ have the same sign.

Table 4.2 Calculated values of $g \cdot b$

g \ b	$\frac{1}{3}[\bar{1}2\bar{1}3]$	$\frac{1}{3}[11\bar{2}3]$	$\frac{1}{3}[2\bar{1}\bar{1}3]$	$\frac{1}{3}[1\bar{2}13]$	$\frac{1}{3}[\bar{1}\bar{1}23]$	$\frac{1}{3}[\bar{2}113]$
$000\bar{2}$	-2	-2	-2	-2	-2	-2
$10\bar{1}\bar{1}$	-1	0	0	-1	-2	-2
$1\bar{1}0\bar{1}$	-2	-1	0	0	-1	-2
$10\bar{1}0$	0	1	1	0	-1	-1
$0\bar{1}1\bar{1}$	-2	-2	-1	0	0	-1

Thus, it can be determined that the dislocations in this particular LAGB have four types of Burgers vectors: $\frac{1}{3}[\bar{1}2\bar{1}3], \frac{1}{3}[11\bar{2}3], \frac{1}{3}[2\bar{1}\bar{1}3]$ and $\frac{1}{3}[1\bar{2}13]$. Figure 4.11 shows the above Burgers vectors in an hcp unit cell. $[5\bar{4}\bar{1}0]$ is the dislocation line direction.

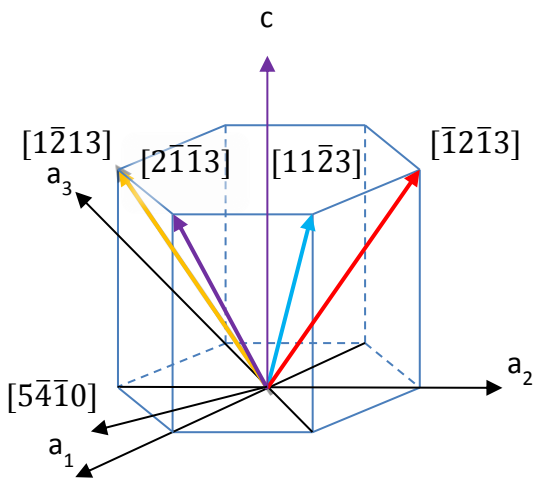

Figure 4.11 Illustration of four observed Burgers vectors in an hcp unit cell

The <c+a> LAGB given above is not an isolated one, although <c+a> LAGBs are less common than <a> LAGBs in the annealed specimen. Figure 4.12 shows another <c+a> dislocation formed LAGB in a different grain of the annealed sample. It also lies roughly on the basal plane as shown in Figure 4.12a. However, unlike the almost straight dislocations in the LAGB labelled 1 in Figure 4.7b, the <c+a> LAGB in Figure 4.12 contains many dislocations which have kinks. These dislocations with kinks are similar to the dislocation labelled 2 in Figure 4.7b and frequently appear in <c+a> LAGBs. In this LAGB (Figure 4.12), the variation in the dislocation contrast also indicates that they have different Burgers vectors. As shown in the upper zoom-in image (Figure 4.12b), the contrast of dislocations labelled 1-3 is stronger, although not so obviously, than the contrast of dislocations labelled 4-6. The criterion of invisibility is the same as stated for the former <c+a> LAGB. Also, similar grown-in <c+a> LAGBs are present in the compressed sample which will be further

investigated in section 4.3. From the above, it can be indicated that LAGBs formed of <c+a> dislocations with different Burgers vectors commonly exist in the annealed specimen.

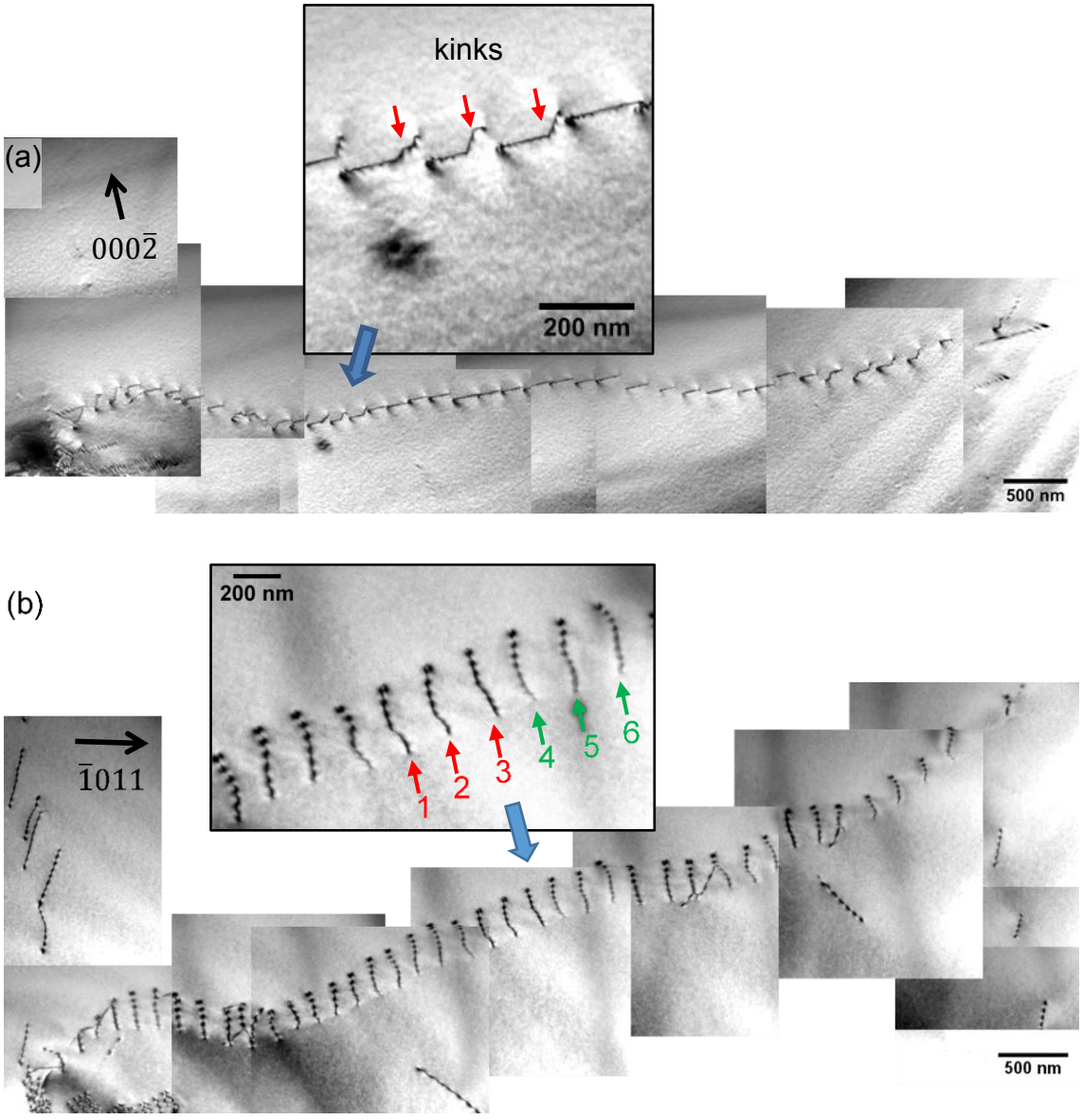

Figure 4.12 Another LAGB formed of <c+a> dislocations imaged using different Burgers vectors (a) $g = 000\bar{2}$, $BD \sim [1\bar{2}10]$ (b) $g = \bar{1}011$, $BD \sim [1\bar{1}01]$

4.2.2.2. Misorientation across the <c+a> LAGB in Figure 4.7

In this section, two distinct approaches are used to determine the misorientation of the LAGB shown in Figure 4.7. As shown in Figure 4.13, the <c+a> dislocations lined up when image along $[\bar{1}2\bar{1}0]$ and become edge-on. The grain boundary plane is parallel to (0002). As shown in Figure 4.11, the angles between the dislocation line direction $[5\bar{4}\bar{1}0]$ and the Burgers vectors ranges from 60° to 113°. Thus, these <c+a> dislocations have mix character.

Figure 4.13a shows a bright field image of the LAGB using 0002 reflection. Figure 4.13b shows the Kikuchi patterns taken from both sides of the LAGB. The beam direction is approximately $[\bar{1}2\bar{1}0]$. The larger Kikuchi pattern was taken from the left side of the LAGB, the smaller one from the right. The tilt angle between both sides of the LAGB was measured from the specimen tilts of two Kikuchi patterns as 0.3°.

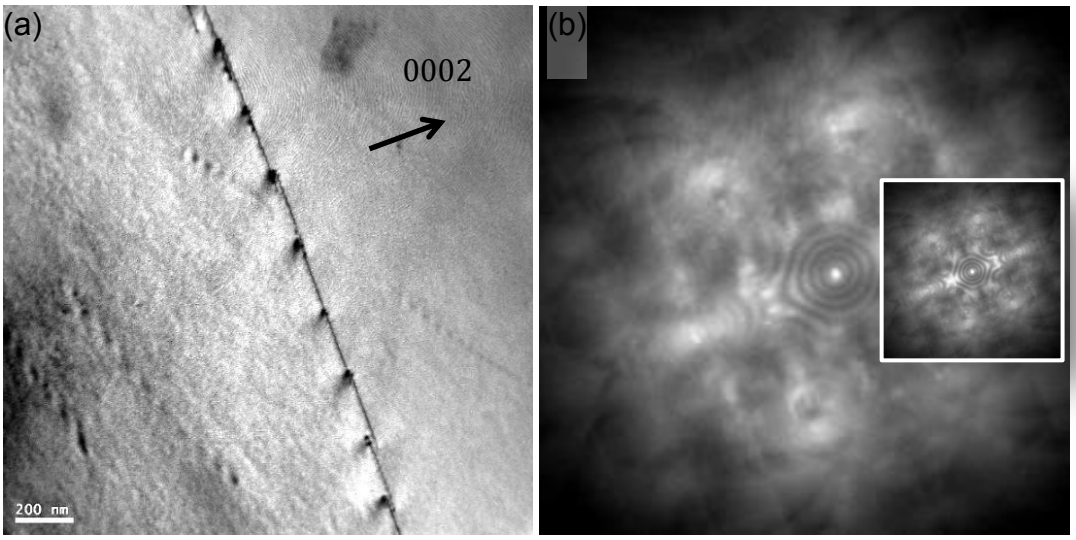

Figure 4.13 (a) Bright field image of the LAGB in Figure 4.7 using the 0002 reflection (b) Kikuchi patterns taken from both sides of the LAGB, $\mathrm{BD} = [\bar{1}2\bar{1}0]$

The dislocations in this boundary could not be tilted to end-on. The following correction formula can be used to adjust the projected angle. The relationship between the projected tilt angle β measured from Kikuchi patterns and the true tilt angle γ caused by the LAGB is:

$$l_1 = \frac{a}{cos\,\alpha},$$

$$l_2 = a \tan\frac{\beta}{2},$$

$$\gamma = 2\tan^{-1}\frac{l_2}{l_1} = 2\tan^{-1}(\tan\frac{\beta}{2}\cos\alpha) \qquad (1)$$

l_1, l_2, a are the intermediate parameters shown in Figure 4.14. α is the angle between the beam direction and the dislocation line direction.

Since the dislocations lie on plane $(000\bar{2})$ (Figure 4.9a) and plane $(12\bar{3}1)$ (Figure 4.9c), the dislocation line direction can be calculated via the formula: $u = P_1 \times P_2 \rightarrow [5\bar{4}\bar{1}0]$. The angle α between the line direction $[5\bar{4}\bar{1}0]$ and the beam direction $[\bar{1}2\bar{1}0]$ is $40.1°$.

When $\beta = 0.3°$, $\alpha = 40.1°$, the true experimental tilt angle is $\gamma = 0.23°$.

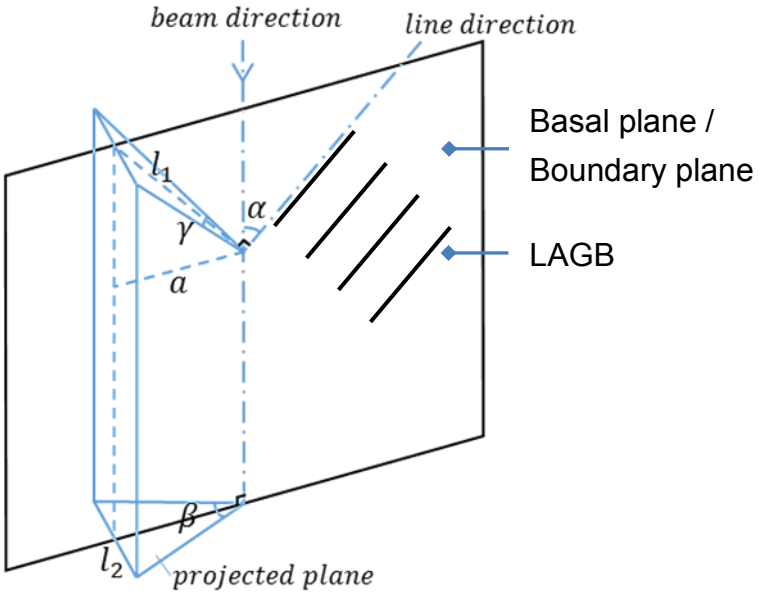

Figure 4.14 Relationship between the true tilt angle γ caused by the LAGB and the projected angle β measured from Kikuchi patterns

Similarly, the dislocation separation distance also needs to be corrected:

$$D = l \cos \alpha \tag{2}$$

where D is the true dislocation separation distance, l is the projected distance and α is the angle between the beam direction and the dislocation line direction (Figure 4.15).

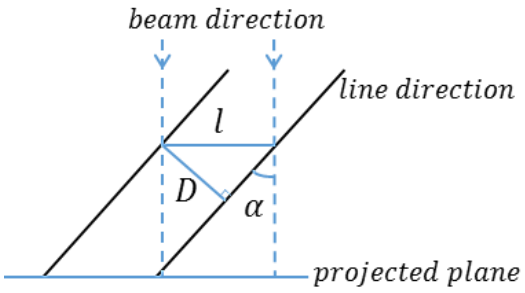

Figure 4.15 Orientation of dislocations

In the α phase of Ti64, the magnitude of the <c+a> Burgers vector $|b| = \sqrt{a^2 + c^2} = \sqrt{0.2925^2 + 0.467^2} = 0.551nm$. The average projected distance $l = 200nm$. D= 153 nm. The misorientation calculated via the Frank model [47] is:

$$(\mathrm{r} \times \mathrm{l})\theta = \sum_i N_i b_i$$

$$\theta = 0.21°$$

The misorientations deduced from the dislocation separation and measured directly from Kikuchi patterns match well.

4.2.2.3. <a> LAGB

The majority of the grown-in dislocations in the annealed specimen were of <a> type. These <a> dislocations also form LAGBs. All the <a> type LAGBs were formed by <a> dislocations with the same Burgers vector. They lay on prismatic planes in the lower part of Figure 4.16 ($\mathrm{B} \approx [1\bar{1}01]$). The top part of Figure 4.16 shows the same <c+a> LAGB as in Figure 4.7.

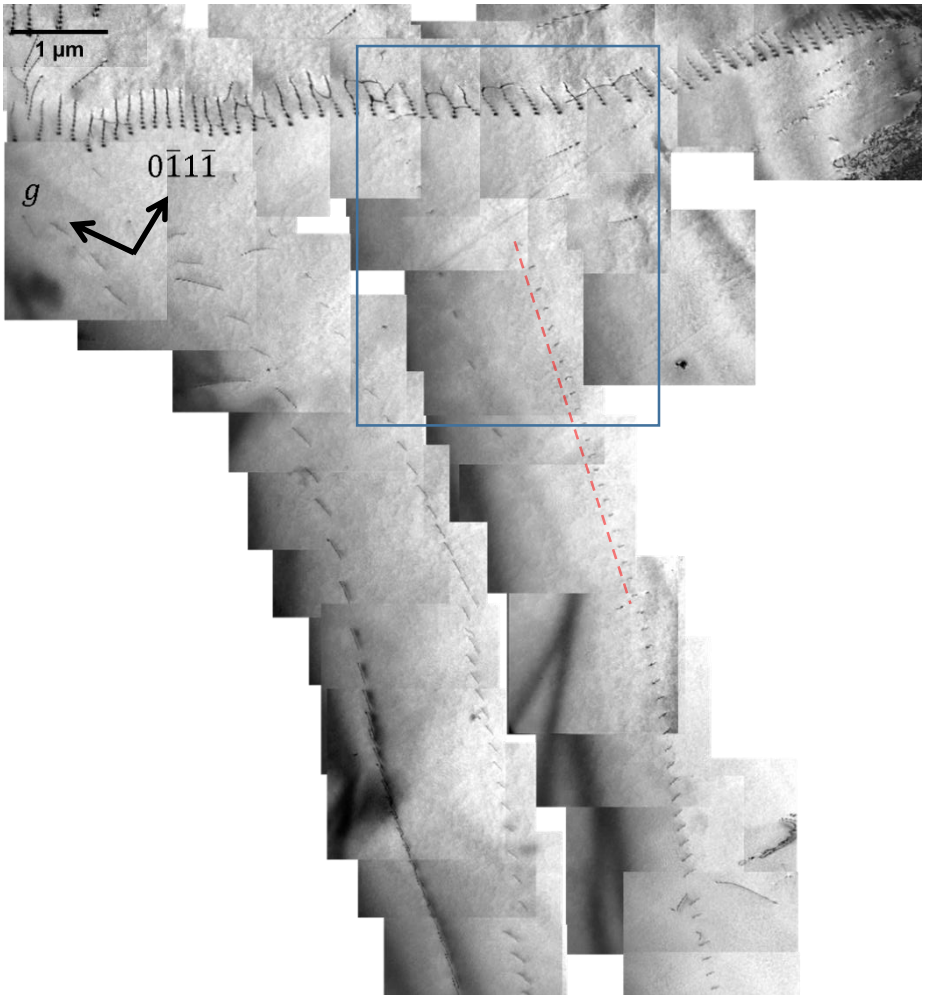

Figure 4.16 The three vertical arrays of dislocations in the lower part consist of <a> LAGBs, $g = 10\bar{1}\bar{1}$, $\mathrm{BD} \sim [1\bar{1}01]$

As shown in Figure 4.16, the <a> LAGB is curved, long range. However, at short range, the segment labelled with a dashed line is relatively straight. Figure 4.17 shows the boxed area in Figure 4.16 when the beam direction is along $[1\bar{1}01]$. The dislocations on the dashed line are end-on and lies on plane $(11\bar{2}0)$. The line direction of these dislocations is $[1\bar{1}01]$. The Burgers vector of these dislocations was determined as $\frac{a}{3}[11\bar{2}0]$ and these dislocations have the same line sense. They are pure edge dislocations. The plane containing these dislocation line direction and their Burgers vector is $(\bar{1}102)$, which is not a common slip plane for <a> dislocation. Thus, the dislocations are regarded as sessile.

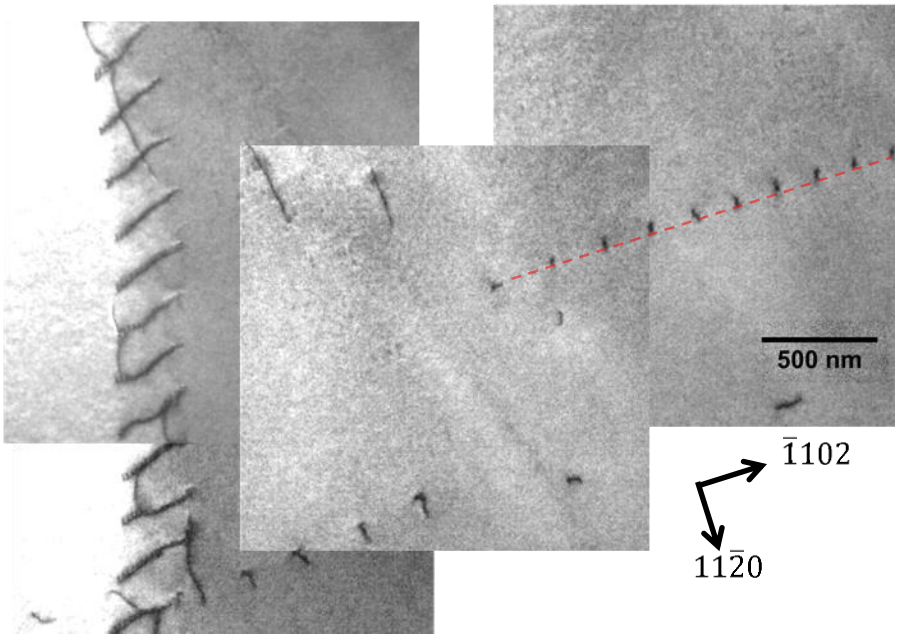

Figure 4.17 <a> LAGB labelled by the dashed line lies on plane $(\bar{1}\bar{1}20)$, $\mathrm{BD} = [1\bar{1}01]$

4.2.3. Dislocations in the annealed specimen

The annealed specimen had a relatively low dislocation density. Except for a few randomly distributed ones, most of dislocations are arranged as LAGBs. The Burgers vectors of the dislocations in the selected area have been identified.

In Figure 4.18, the red dislocations have been identified as $\frac{1}{3}[\bar{1}2\bar{1}3]$, the purple ones $\frac{1}{3}[2\bar{1}\bar{1}3]$, blue $\frac{1}{3}[11\bar{2}3]$ and yellow $\frac{1}{3}[1\bar{2}13]$. As shown in Figure 4.9, almost all the purple dislocations are the pinning positions for a_3 dislocations. The other two types of <c+a> dislocation are rare: the green $\frac{1}{3}[\bar{1}\bar{1}23]$, and the orange $\frac{1}{3}[\bar{2}113]$. The majority of the dislocations are the red ($\frac{1}{3}[\bar{1}2\bar{1}3]$).

The Burgers vectors of the <a> dislocations are shown in Figure 4.19 using the $10\bar{1}1$ reflection. All the <a> dislocations have been marked by coloured lines in the same way as above. For yellow $\mathrm{b} = \frac{1}{3}[11\bar{2}0]$, green $\mathrm{b} = \frac{1}{3}[1\bar{2}10]$, and blue $\mathrm{b} = \frac{1}{3}[\bar{2}110]$. The great preponderance, therefore, are of one type: a_3.

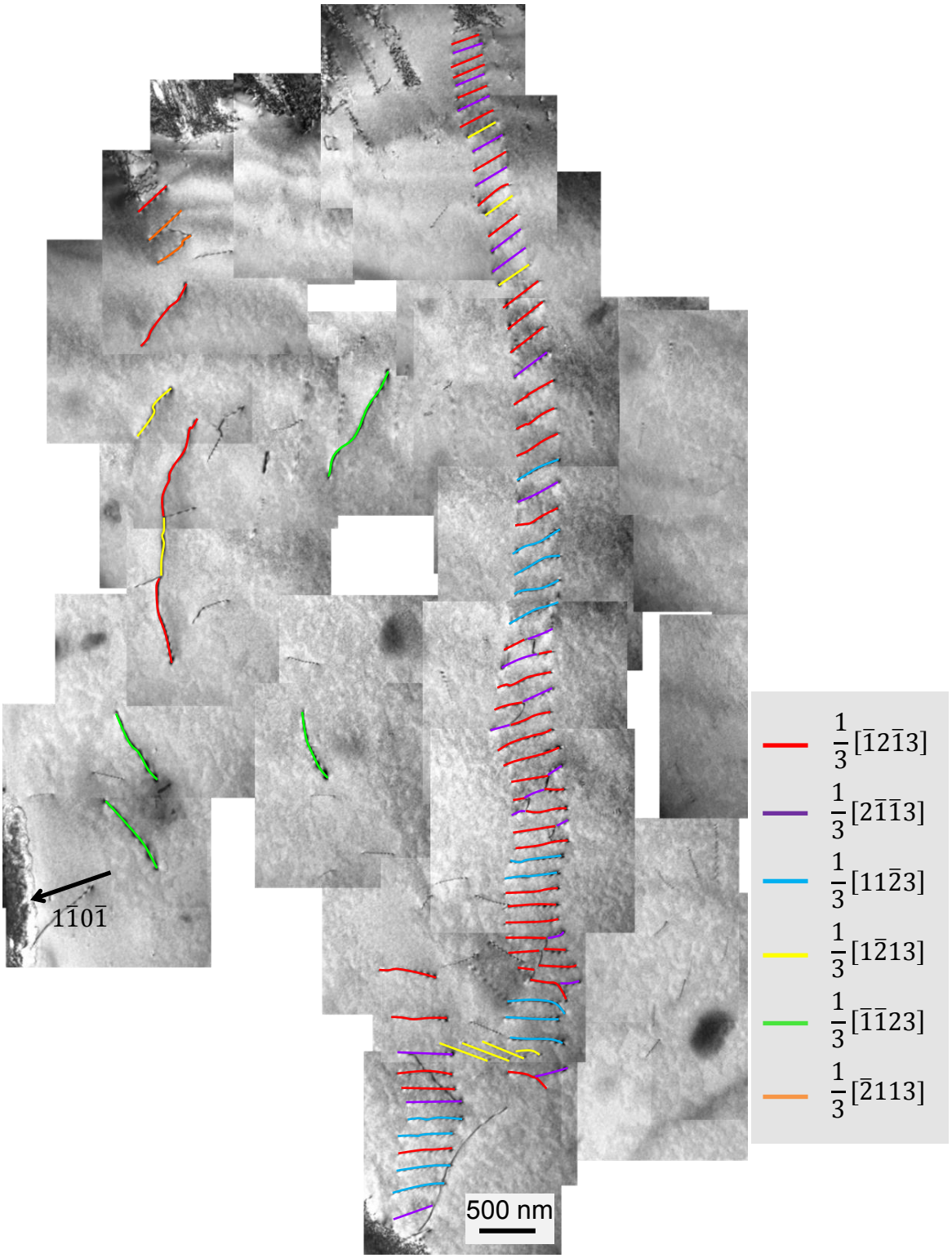

Figure 4.18 Six types of <c+a> dislocations exist in the annealed sample labelled using different colours. <c+a> LAGB is formed of four types of dislocations. $g = 1\bar{1}0\bar{1}$ BD ~ $[2\bar{1}\bar{1}3]$

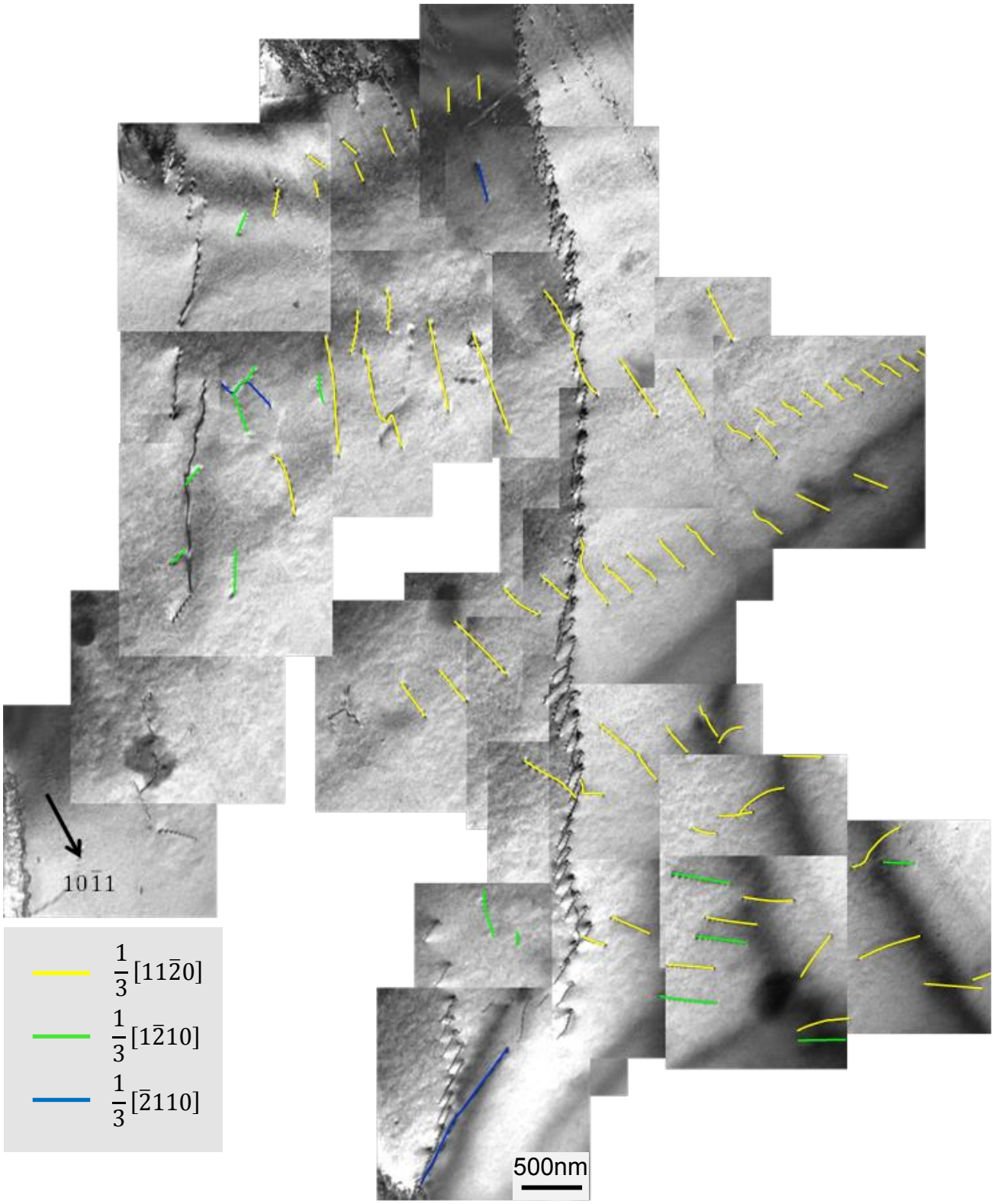

Figure 4.19 Three types of <a> dislocations exist in the annealed sample represented by different colours. Most of them are a_3. $g = 10\bar{1}1$, BD ~ $[1\bar{3}21]$

4.2.4. Discussion

4.2.4.1. Formation of LAGB

The as-received specimen was highly deformed and contained lots of dislocations. One possibility is that multiple slip induced by thermal stress results in the formation of LAGB as shown schematically in Figure 4.20. The array of dislocations comes from various slip systems and composes the LAGB. Thus, this array of dislocations has different Burgers vectors.

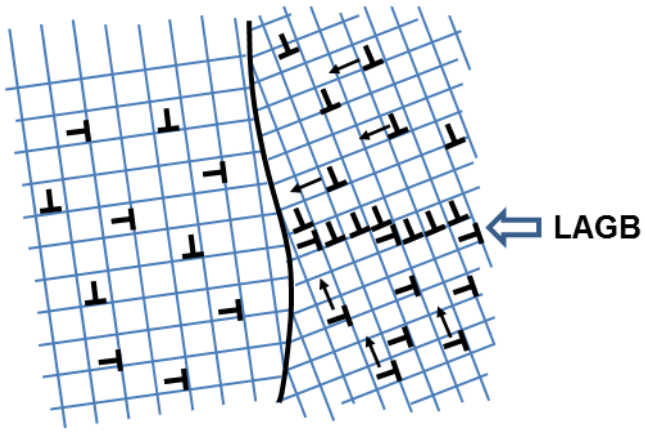

Figure 4.20 Schematic diagram showing how multiple slip contributes to the formation of LAGB.

Another possible formation mechanism of LAGB is caused by the precipitation of hcp α laths from the bcc β matrix. During the β/α transformation in cooling stage of annealing, the interfaces are semi-coherent and normally adopt specific crystallographic planes [107]. The exact plane adopted depends on the ratio of the lattice parameters. The interfaces can be characterized by a broad face, which

contains the ‘invariant line’ between the α and β phases, a side face and an edge face as shown in Figure 4.21. Different interfaces were observed consisting of different type of misfit dislocations [107-109]. Suri et al. [107] observed that the side face $(0001)_\alpha$ contains <a> misfit dislocations, while the broad face $(1\bar{4}30)_\alpha$ contains <c> dislocations. Menon and Aaronson [108] observed <a> misfit dislocations on the broad faces and <c+a> dislocation on the edge faces in a Ti-Cr alloy. Furuhara et al. [109] claimed that misfit dislocations on the broad face $(\bar{1}100)_\alpha$ are <c> type.

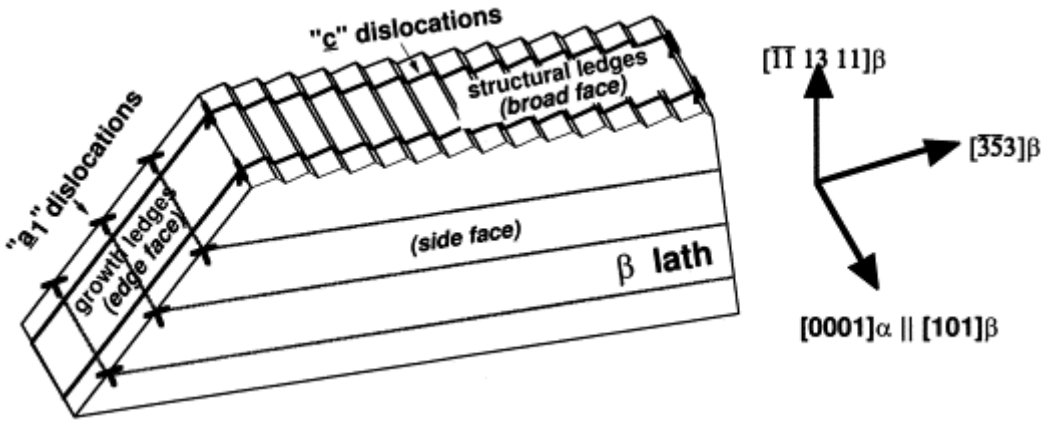

Figure 4.21 Schematic diagram representing the interface between the α and β phases. The side face of the β laths is $(101)_\beta$ and parallel to $(0001)_\alpha$. [107]

Figure 4.22 shows the process of the formation of LAGB in the annealed specimen as inferred from the above characteristics. At the beginning of the phase transformation, α phase surrounded by β phase has different misfit dislocations on different interfaces (Figure 4.22a). <c+a> dislocations lie on basal planes and <a> dislocations lie on prismatic planes. Misfit dislocations on the interfaces migrate with

the growth of α laths and eventually meet and form LAGBs when β phase transform totally into α phase (Figure 4.22b).

Or, LAGBs are intrinsically geometrically necessary boundaries formed between regions of different strain to accommodate the accompanying difference in lattice rotation [110].

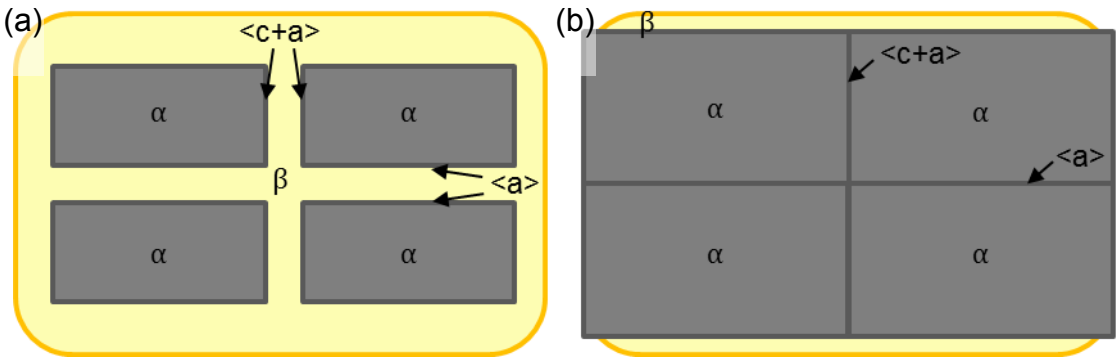

Figure 4.22 Schematic formation of LAGB in the annealed specimen during cooling stage. Misfit dislocations from the β/α interface form LAGB

Solid solutions can also affect grown-in dislocation density. Seki et al. [111] assumed that impurities act as obstacles for the introduction and propagation of dislocations. Since the bond strength is larger between solute atoms and the surrounding sublattice site atoms, dislocations tend to be pinned by solute atoms. The concentration of Bi has been directly observed by high-resolution HAADF-STEM imaging on a Cu grain boundary [112]. The specific reason needs further investigation.

4.2.4.2. Variety of <c+a> dislocations on LAGB

Interaction of <a> and <c+a> boundary dislocations may be the reason why dislocations in the <c+a> LAGBs have four types of Burgers vector. Lee et al. [99] demonstrated that the incorporation and decomposition of glissile dislocations into the grain boundary caused a change of the Burgers vector of grain-boundary dislocations or for a certain segment of dislocations to annihilate in α-Ti, although they did not identify the grain boundary dislocations. This may lead to a diversification of Burgers vectors in the <c+a> LAGB.

As shown clearly in Figure 4.9, <a> type dislocations can be trapped at boundary dislocations. Specifically, they were pinned by the dislocations labelled 2 and 7 which notably have a different Burgers vector from the dislocations around. It is also shown in the lower part of the <c+a> LAGB (Figure 4.18) that the red dislocations ($\frac{1}{3}[\bar{1}2\bar{1}3]$) and the purple dislocations ($\frac{1}{3}[2\bar{1}\bar{1}3]$) always tangle together. The indications of dislocation interaction in the <c+a> LAGB are that an initially yellow dislocation ($\frac{1}{3}[1\bar{2}13]$) incorporates a_3 and turns into a purple dislocation ($\frac{1}{3}[2\bar{1}\bar{1}3]$); the blue dislocation ($\frac{1}{3}[11\bar{2}3]$) may result from the red dislocation ($\frac{1}{3}[\bar{1}2\bar{1}3]$). The interactions follow the equations below:

$$\frac{1}{3}[1\bar{2}13] + \frac{1}{3}[11\bar{2}0] \rightarrow \frac{1}{3}[2\bar{1}\bar{1}3]$$

$$\frac{1}{3}[\bar{1}2\bar{1}3] + \frac{1}{3}[2\bar{1}\bar{1}0] \rightarrow \frac{1}{3}[11\bar{2}3]$$

Initially, the <c+a> LAGB was composed of two or three types of dislocations. Thermal stress drove dominant <a> dislocations passing the LAGB to interact with some of the <c+a> dislocations during heat treatment, which led to more variety of <c+a> dislocations on the LAGB.

4.2.5. Conclusions

The annealed specimen has millimetre sized α/β lamellae. The dislocation density has been effectively reduced compared with the as-extruded sample. The dislocations in the annealed specimen are sessile grown-in dislocations. The density of <a> dislocations is higher than that of <c+a> dislocations.

Most dislocations are arranged as LAGBs. Each LAGB contains the same type of dislocation: i.e. either <a> or <c+a>. Compared with the relatively homogeneous distribution of <a> dislocations, <c+a> dislocations tend more to collect into LAGBs. The strong elastic interdislocation interaction due to the large magnitude of <c+a> constrains <c+a> dislocations in the boundary [60]. Given the low number of <c+a> dislocations, <c+a> LAGBs are present in small quantities in individual grains.

The <a> LAGB investigated in this study is formed by <a> dislocations with the same Burgers vector of $\frac{1}{3}[11\bar{2}0]$ and lies on the second order prismatic plane $(11\bar{2}0)$. The <c+a> LAGBs lie on basal plane. The Burgers vectors of the dislocations on <c+a> LAGB are various. In the particular case presented in Figure 4.7, there are four Burgers vectors within one <c+a> LAGB: $\frac{1}{3}[\bar{1}2\bar{1}3]$, $\frac{1}{3}[11\bar{2}3]$, $\frac{1}{3}[2\bar{1}\bar{1}3]$ and $\frac{1}{3}[1\bar{2}13]$.

One possible reason that LAGBs adopt specific crystallographic planes is that different type of misfit dislocations exist on different β/α interfaces during phase transformation (<c+a> basal, <a> prism). They migrate with the growth of α laths and eventually meet and form LAGBs when β/α transfer totally complete. Dislocation interaction may lead to a greater variety of <c+a> dislocations on their LAGB.

4.3. Macroscopic compression test & the deformed microstructure

4.3.1. Mechanical behaviour of the compressed specimen

A typical stress-strain curve recorded from the compression test on the as-annealed specimen is shown in Figure 4.23. The yield stress (0.2 proof stress) of about 900 MPa can be determined. The proportional limit is about 750MPa.

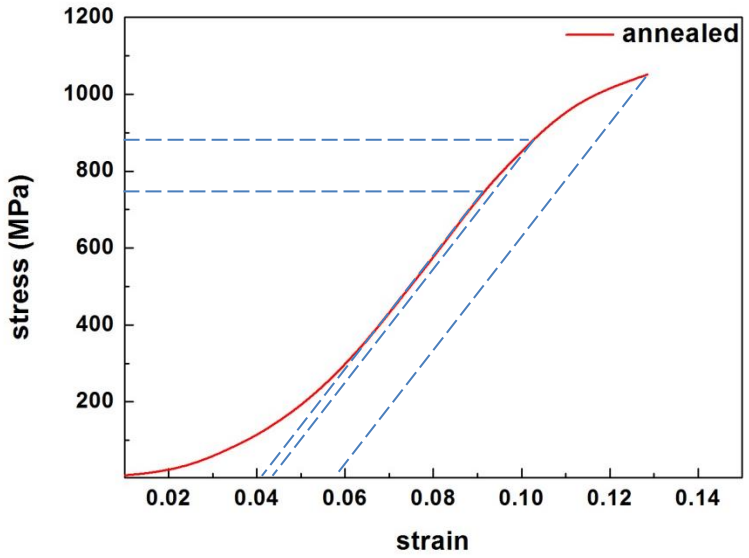

Figure 4.23 Stress-strain curve obtained from the annealed sample

4.3.2. Microstructure of the compressed specimen

No observable difference can be observed from the SEM image of the macroscopic compressed sample compared with the as-annealed specimen (Figure 4.24a).

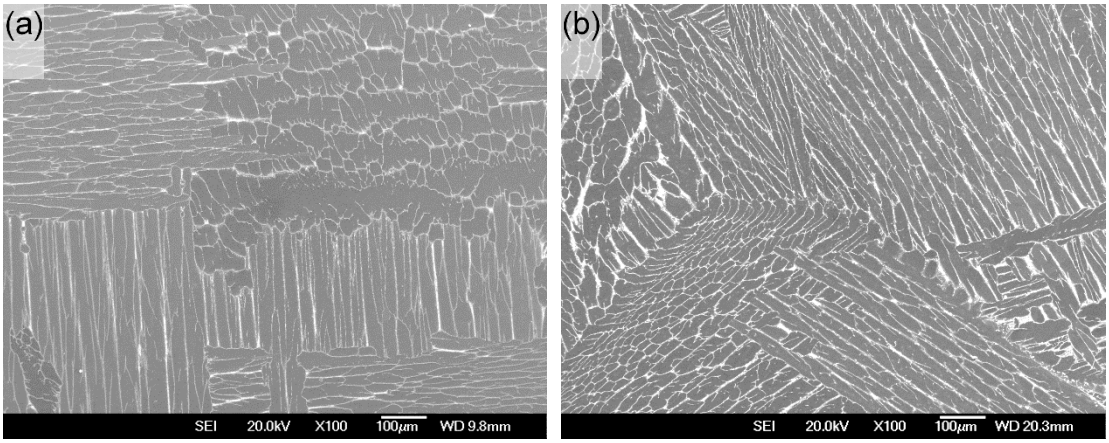

Figure 4.24 SEM images of (a) annealed sample and (b) compressed sample

4.3.3. Dislocations in the compressed specimen

Figure 4.25 shows images taken from two different areas of the compressed sample. The foil normal was along the loading direction. Multiple slip systems were activated during the compression. The distribution of dislocations was inhomogeneous. The majority of dislocations were arranged in slip bands. Some dislocations lay randomly in the area between the slip bands.

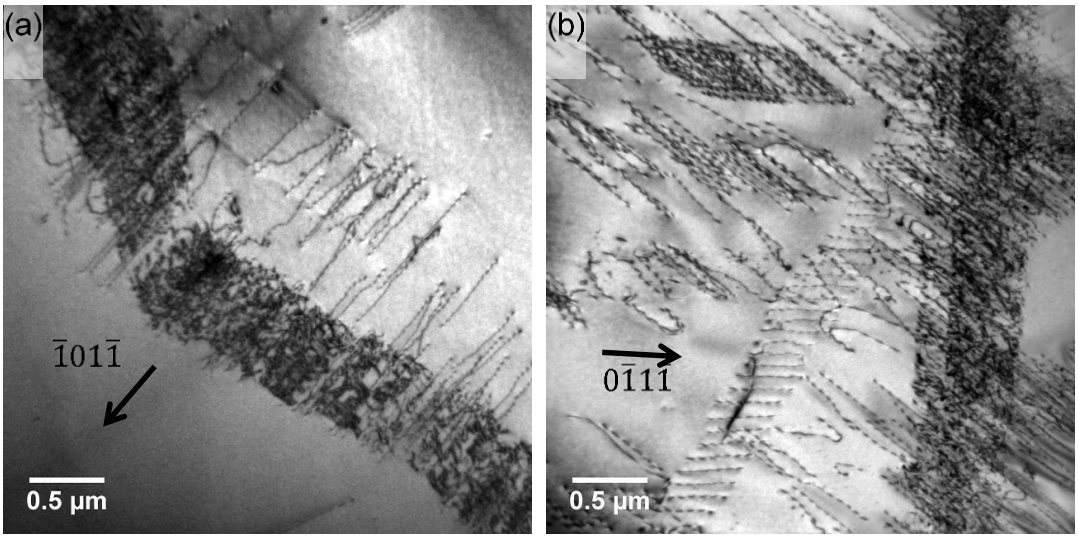

Figure 4.25 Dislocations in different grains of a sample compressed by 2 % (a) $\mathrm{g} = \bar{1}01\bar{1}$, $\mathrm{BD} \sim [1\bar{5}43]$ (b) $\mathrm{g} = 0\bar{1}1\bar{1}$, $\mathrm{BD} \sim [1\bar{2}13]$

The bright field image (Figure 4.26) shows a relatively large region in the compressed sample, which was imaged using the same beam direction and reflection vector as in Figure 4.7b. Compared to the annealed sample (Figure 4.7b), the slip traces in the compressed sample indicate the activation of multiple slip.

In Figure 4.26, the dislocations (labelled 3) are <c+a> dislocations located on the basal plane. They have a similar configuration to the dislocations in the <c+a> LAGB in the annealed sample (c.f. dislocation labelled 1 in Figure 4.7b). The dislocations labelled 4 have segments on the basal plane with some non-basal facets. This dislocation configuration is similar to the dislocations labelled 2 in Figure 4.7b. These <c+a> dislocations (labelled 3 and 4) in the compressed sample are probably grown-in dislocations formed during the annealing.

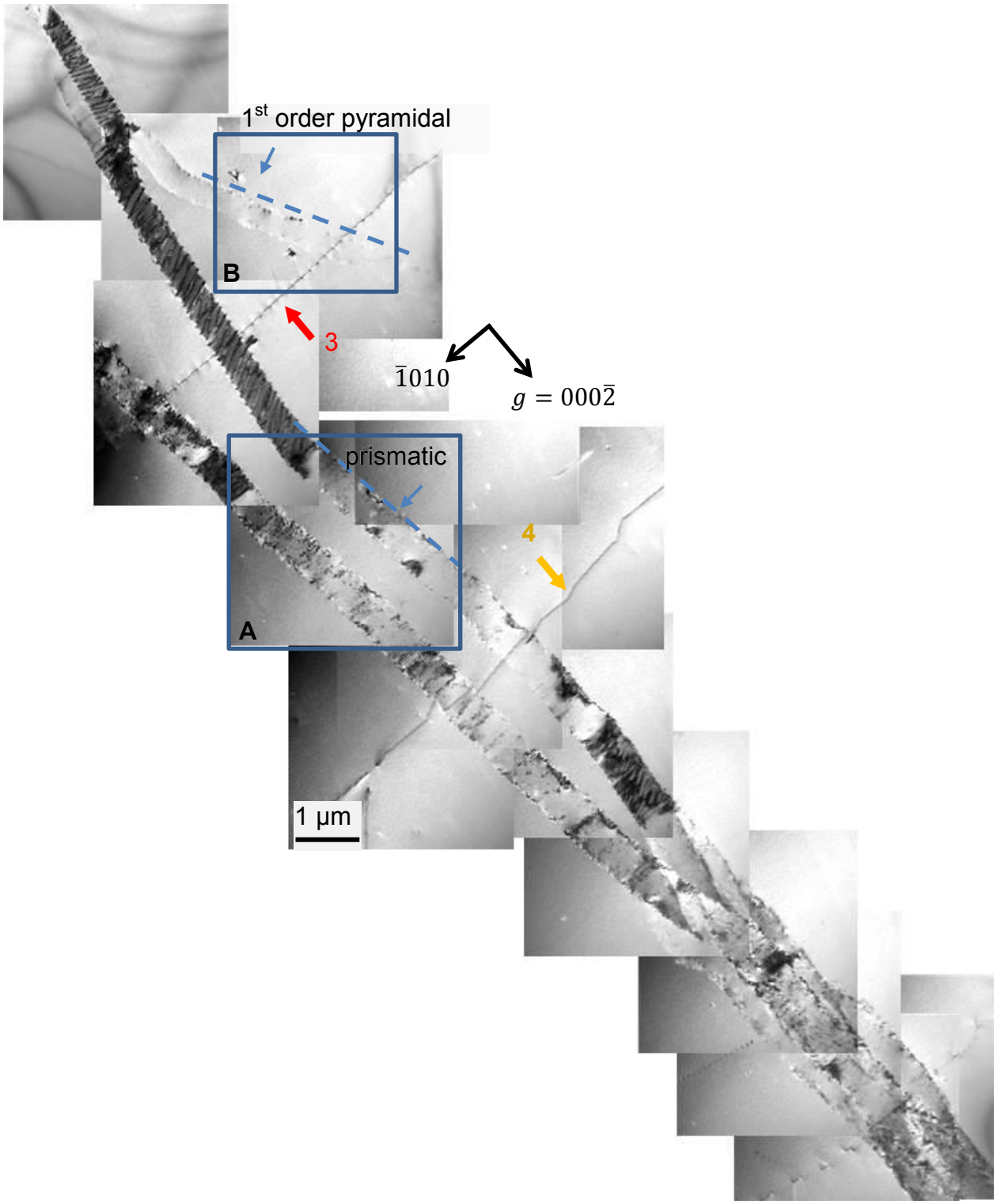

Figure 4.26 Dislocations slip on pyramidal and prismatic planes in the compressed sample. $\mathrm{g} = 000\bar{2}$, $\mathrm{BD} \sim [1\bar{2}10]$

Besides the grown-in dislocations, Figure 4.26 indicates that the compressed sample contains long slip bands on prismatic and pyramidal planes (labelled by the dashed lines). Most of these dislocations have an <a> Burgers vector, and are out of contrast when $\mathrm{g} = 000\bar{2}$. The curved slip bands might be caused by the cross-slip of the <a> dislocations. There are segments in contrast with $\mathrm{g} = 000\bar{2}$, near the intersection of the slip band and the grown-in LAGB labelled 3.

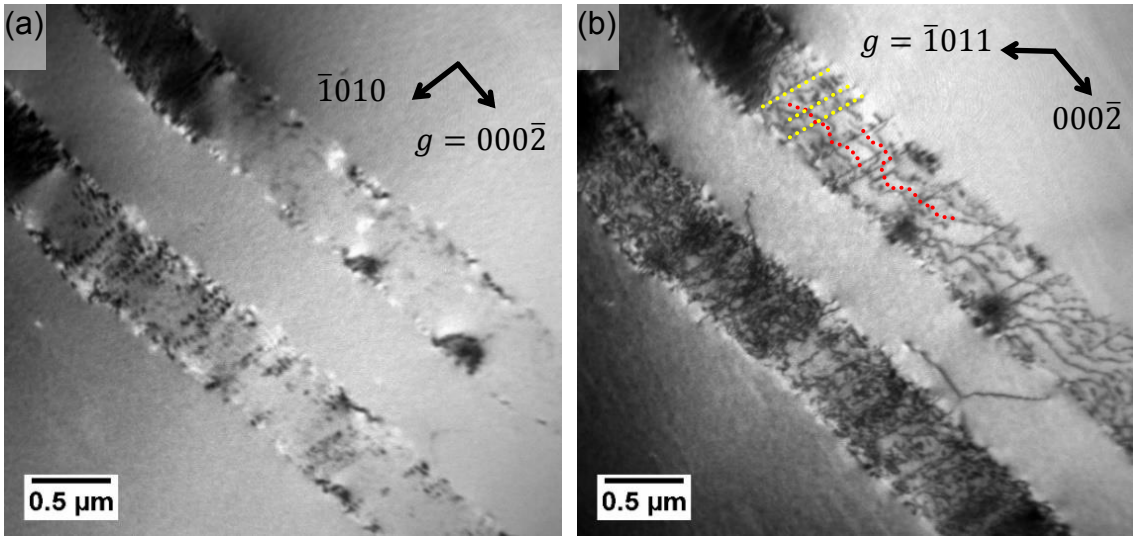

Figure 4.27 <a> dislocations in the slip bands labelled by yellow and red dotted lines are screw and edge dislocations. (a) $\mathrm{g} = 000\bar{2}$, $\mathrm{BD} \sim [1\bar{2}10]$ (b) $\mathrm{g} = \bar{1}011$, $\mathrm{BD} \sim [1\bar{2}10]$

Figure 4.27 shows detailed configuration of dislocations in Box A in Figure 4.26. Since the slip traces are perpendicular to the basal plane, they are prismatic slip bands. Within the slip band, dislocations lines lie in two directions, as marked by the red and yellow dotted lines. Burgers vectors of these dislocations are the same although not fully determined. The yellow dislocations with line direction

perpendicular to slip trace are screw dislocations. Conversely, the red dislocations with line direction parallel to the slip trace have edge character.

The slip trace labelled by the dashed line in Box B in Figure 4.26 is at an angle to the basal plane, which indicates that it is a pyramidal slip band. The slip system of the dislocations in this slip band has been analysed as below. Figure 4.28 is the boxed area B in Figure 4.26 containing the pyramidal slip band and a LAGB using different reflection vectors. All the dislocations in the slip band are out of contrast when $\mathrm{g} = 000\bar{2}$ (Figure 4.28a) and $\mathrm{g} = 1\bar{1}0\bar{1}$ (Figure 4.28b). Thus, these dislocations have a Burgers vector of $\frac{1}{3}[11\bar{2}0]$.

Most of the dislocations in this slip band are straight and parallel to each other. Take the dislocation marked by arrow 1 as an example to analyse its line direction. As shown in Figure 4.28c and 4.28d, it lies on plane (0002) and $(1\bar{1}0\bar{1})$. Therefore, the dislocation line is the intersection of two planes, which is $[11\bar{2}0]$. The line direction is parallel to the Burgers vector. So all the parallel straight dislocations are screw dislocations.

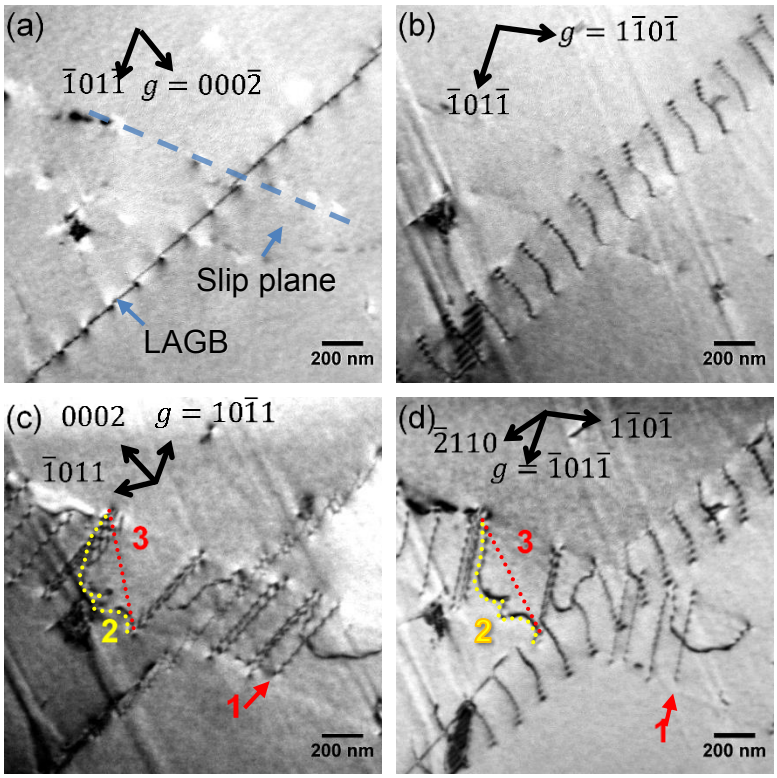

Figure 4.28 (a - d) the same area of slip band imaged using different g vectors. (a) $g = 000\bar{2}$,$BD \sim [1\bar{2}10]$ (b) $g = 1\bar{1}0\bar{1}$, $BD \sim [0\bar{1}11]$ (c) $g = 10\bar{1}1$, $BD \sim [1\bar{2}10]$ (d) $g = \bar{1}01\bar{1}$,$BD \sim [0\bar{1}11]$

The line direction and Burgers vector of the screw dislocations do not define a unique slip plane. Thus, the curved dislocation labelled 2 was chosen to determine the slip plane. Both ends of the curved dislocation were joined by the straight line labelled 3, which also lies on the slip plane. The direction of the connecting line can be inferred using the previous method, and it is $[0\bar{1}1\bar{1}]$. Thus, the slip plane can be determined by the Burgers vector (b) and line direction of the connecting line (u): $b \times \mathrm{u} \rightarrow (1\bar{1}01)$.

Another method is the trace analysis, which determined the slip plane by using the slip trace line and the Burgers vector. As shown in Figure 4.28, the trace lies on plane $(\bar{1}01\bar{1})$. At the same time, it lies on the sample surface, since the slip trace is the intersection of the slip plane and the foil surface. The foil normal of the area of interest is approximately $[1\bar{3}21]$. Converting from real space to reciprocal space, the surface plane is $(10\overline{30}20{,}17)$. The trace line direction can be calculated as $[\overline{67}44{,}23{,}90]$. Thus, the slip plane is $(30\overline{30}0{,}37)$, which is approximately $(1\bar{1}01)$ considering the measurement errors in this type of experiment. The result agrees with the previous calculation.

Figure 4.29 shows a typical cross-slipped slip band in another grain of the compressed sample. Figure 4.30 is the boxed area of the slip band in Figure 4.29 shown using different reflections. All the dislocations shown in the image have the same Burgers vector which can be determined as a_3 from Figure 4.30a and 4.30b. The slip planes marked by the red and blue dashed frames in Figure 4.29 were determined as $(\bar{1}10\bar{1})$ and $(1\bar{1}00)$ from Figure 4.30. The parallel straight dislocations in the slip band have screw character. They cross slipped repeatedly between a prismatic plane and a pyramidal plane.

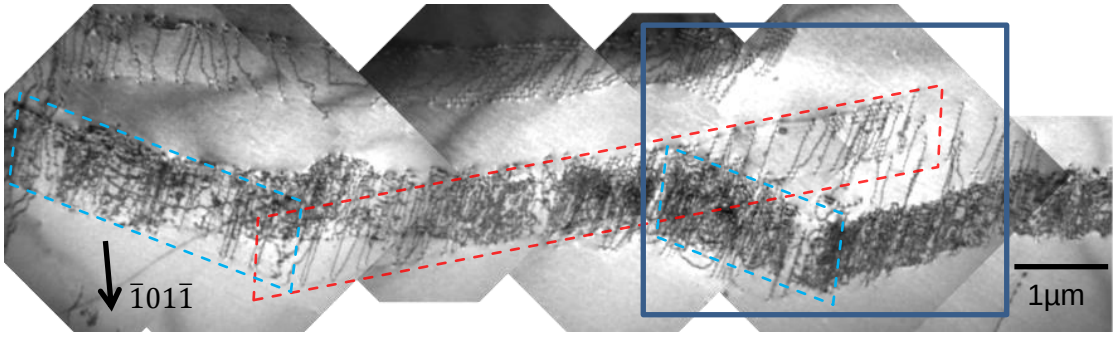

Figure 4.29 A typical cross-slip band in the compressed sample (a) $g = \bar{1}01\bar{1}$, $BD \sim [1\bar{2}10]$.

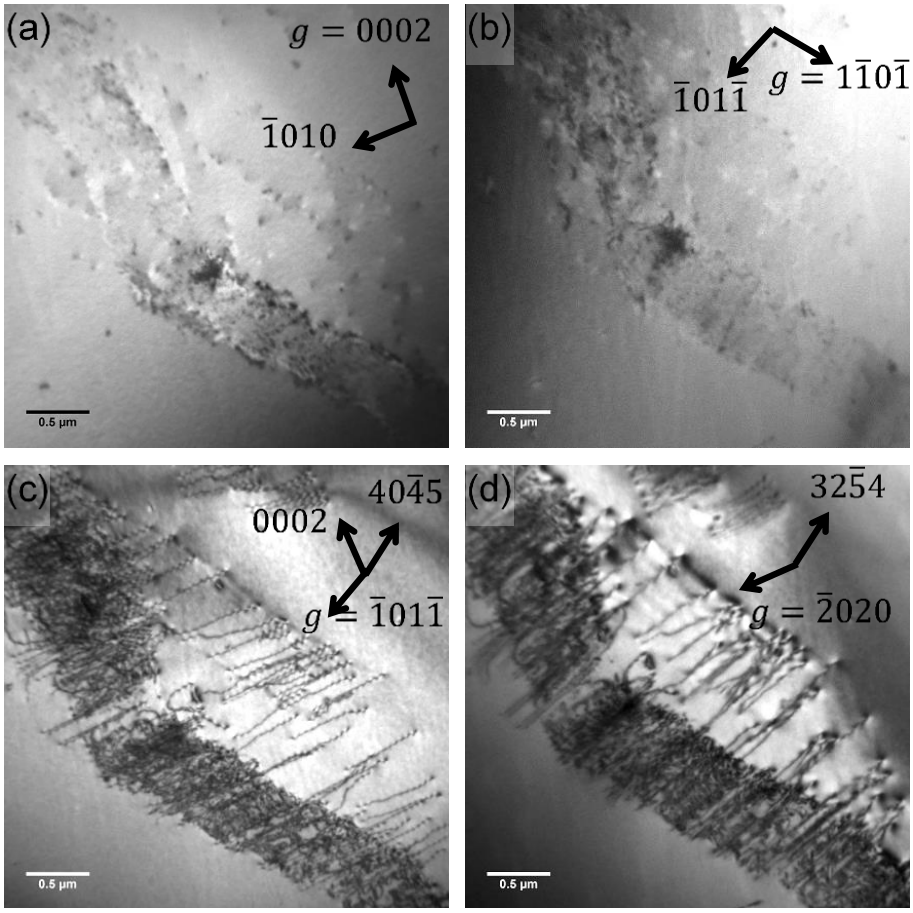

Figure 4.30 multiple slip of <a> dislocations with the same Burgers vector (a) $g = 0002$, $BD \sim [1\bar{2}10]$ (b) $g = 1\bar{1}0\bar{1}$, $BD \sim [0\bar{1}11]$ (c) $g = \bar{1}01\bar{1}$, $BD \sim [1\bar{2}10]$ (d) $g = \bar{2}020$, $BD \sim [2\bar{4}23]$.

4.3.4. Dislocation dissociation

Dislocations with unusual contrast similar to the ones observed in Figure 4.26 were observed repeated in different compressed specimen.

The slip bands labelled 1-10 in Figure 4.31 illustrate different slip systems, and were imaged under different reflection vectors. When the reflection vector is 0002 (Figure 4.31a), the slip bands labelled 1-7 are out of contrast, which indicates they are of <a> type dislocation. They are also out of contrast when $g = \bar{1}01\bar{1}$ (Figure 4.31b). Thus, the Burgers vector of these dislocations is $\pm\frac{1}{3}[1\bar{2}10]$. When the beam direction is $[1\bar{2}10]$ (Figure 4.31a), bands 1-7 present straight narrow lines perpendicular to the basal plane, which indicates that the slip plane is $(10\bar{1}0)$. In Figure 4.31c, among the prismatic slip bands 1-7, band 5 goes straight though the LAGB. Bands 2 and 3, 6 and 7 are staggered by a small distance and obstructed by the LAGB. The difference in the configuration of band 5 from band 2,3,6,7 is that band 5 has more dense dislocations, which may help the dislocations go through the LAGB. The residual contrast of band 5 is also stronger than that of the others.

Bands 8 and 9 are on a prismatic plane, but show strong contrast when $g = 0002$.

Band 10 is on a pyramidal plane. The contrast of band 10 may be associated with dislocation dissociation.

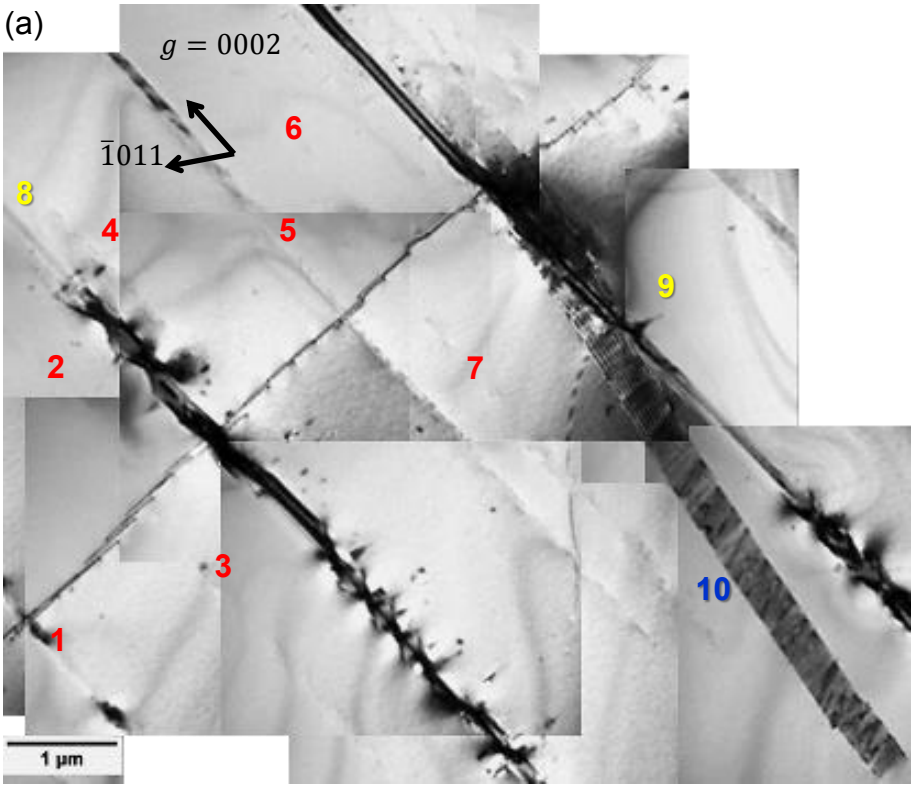
(a)
$g = 0002$
$\bar{1}011$
6
8
4
5
9
2
7
3
10
1
1 μm

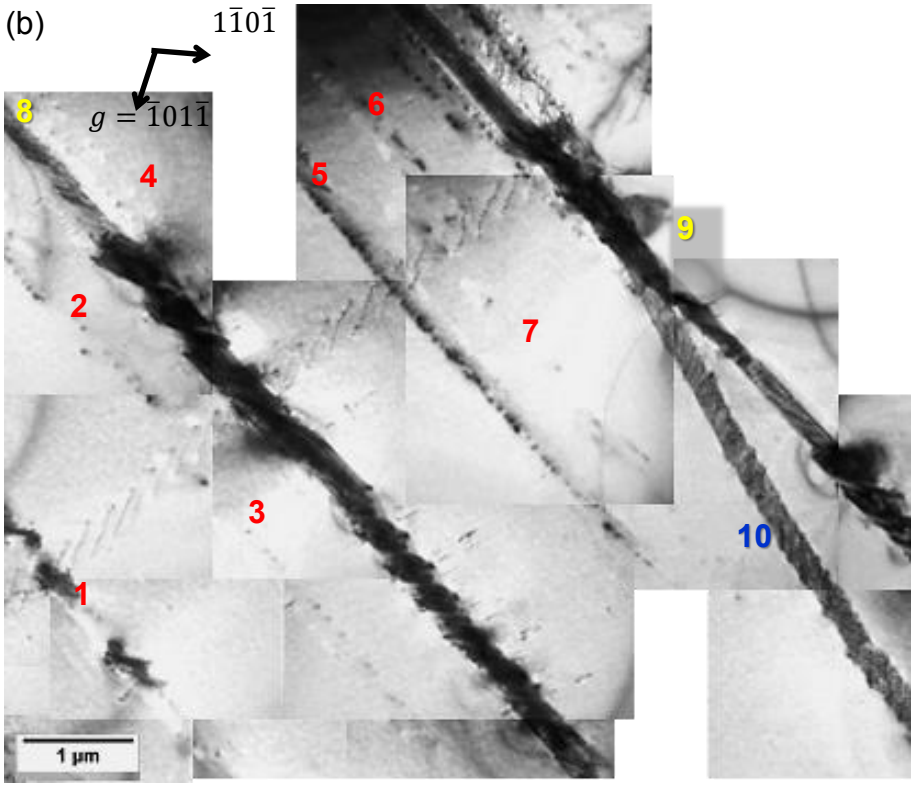
(b)
$1\bar{1}0\bar{1}$
$g = \bar{1}01\bar{1}$
8
6
4
5
9
2
7
3
10
1
1 μm

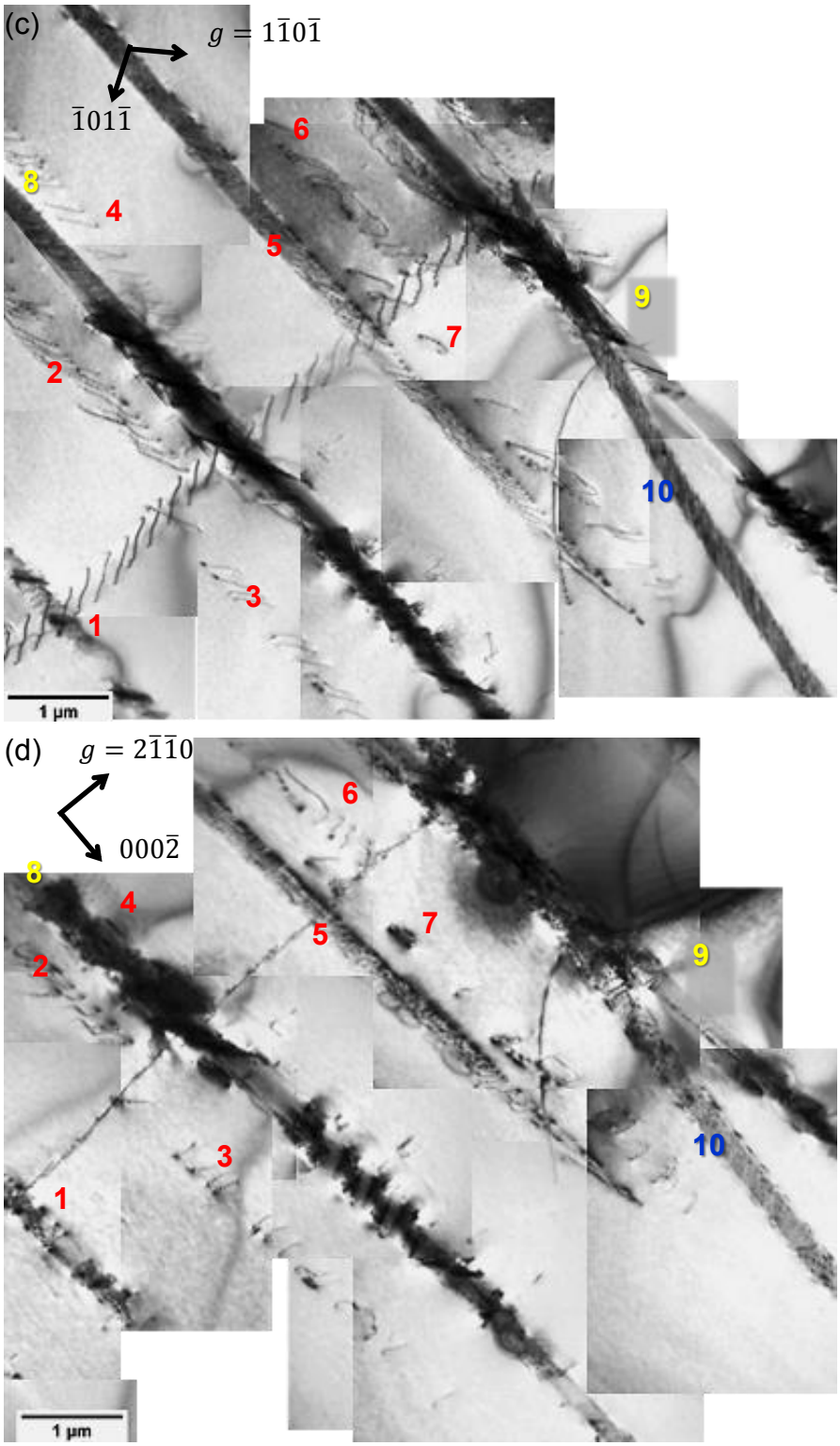

Figure 4.31 (a) to (d) the same area of the sample showing prismatic slip (a) $g = 0002$, $BD \sim [1\bar{2}10]$ (b) $g = \bar{1}01\bar{1}$, $BD \sim [0\bar{1}11]$ (c) $g = 1\bar{1}0\bar{1}$, $BD \sim [0\bar{1}11]$ (d) $g = 2\bar{1}\bar{1}0$, $BD \sim [0\bar{1}10]$

4.3.5. Discussion

4.3.5.1. Planar slip

In the compressed specimen, gliding dislocations form planar slip bands which are common slip features in the low temperature deformed α-TiAl [15]. The reason for the heterogeneous dislocation distribution has been postulated as the breakdown of short-range order (SRO) between Ti, Al and O atoms [113-117]. It was suggested that the addition of Al and O induces SRO into α-TiAl. When the leading dislocation moves through the lattice, SRO is destroyed and cannot be restored by subsequent dislocations. Once a favourable dislocation path has been formed, further slip will concentrate in this slip plane due to the lower friction stress exerted on the trailing dislocations. This leads to planar slip. Theoretically, the strong planar slip character inhibits cross-slip of screw segments [15], since extra stress is required to destroy the SRO within the cross-slip plane. However, when the stress to reactivate a new dislocation source during deformation is much higher than that required for cross-slip, owing to the dislocation starvation effect in materials with planar slip [118], cross-slip occurs. It is reported that cross-slip occurred between two adjacent prismatic slip planes and between a prismatic plane and a pyramidal plane in a cyclically deformed Ti-5at.%Al [115, 119]. This can explain the repeated cross-slip of <a> dislocations between prismatic and pyramidal planes in bulk compressed samples.

4.3.5.2. Extended dislocations

A dislocation can reduce its energy by dissociating into two partials [27, 120, 121]. The band 10 in Figure 4.31a has a similar configuration to the glide of multiple partials on a slip plane [53, 91, 96], which consists of an array of partial dislocations. The discontinuous contrast of the slip band is caused by the uneven distribution of the partial dislocations. The stacking faults are wider when they are away from the first partials. Figure 4.32 is a schematic diagram of an array of partial dislocations. The fringe pattern in band 10 originates in the stacking fault ribbons between partials. Intense cross-slip occurs in the compressed sample as shown in Figure 4.26 and 4.29, especially around prismatic planes. When the cross-slipped dislocations dissociated in these arrays of extended dislocations, the local fringe contrast would change. This may explain the strange configuration of the middle segments of Band 8 and 9. As shown in the upper-left of Band 8 (Figure 4.31b and c), it is an array of extended dislocations on a prismatic plane. When it tangles with another array of extended dislocations nearby, cross-slip accompanied by dislocation dissociation may lead to strong residual contrast. Naka et al. [122] proposed that the a-type screw dislocations in Ti may spilt into two $^{a}/_{9}[1\bar{2}10]$ partials on the $(10\bar{1}0)$ prismatic plane and two $^{a}/_{18}[1\bar{2}10]$ partials on the pyramidal planes $(10\bar{1}1)$ and $(10\bar{1}\bar{1})$. The specific dislocation dissociation reaction need be analysed eventually.

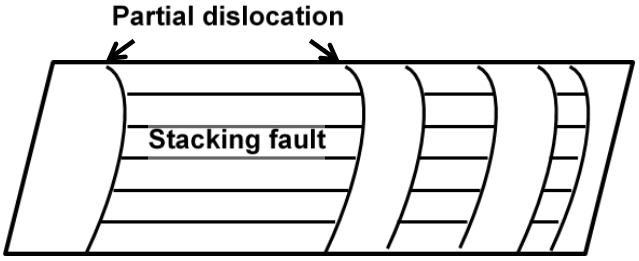

Figure 4.32 A schematic illustration of an array of partial dislocations

4.3.5.3. Interaction of glissile dislocations with LAGB

Both pyramidal (Figure 4.28) and prismatic (Figure 4.31) slip planes were observed to pass unimpeded through the <c+a> LAGB. Compared to the passage of dislocation across grain boundaries studied by Lee et al. [99], the dislocation density in an LAGB is relatively smaller than that in a normal grain boundary, which may relax the restriction of direct transfer. Piled-up dislocations slipping along the LAGB may also occur in the compressed specimen. These piled-up dislocation would decompose into partial dislocations when slipping on the boundaries [99]. The interaction of piled-up dislocations and the grown-in <a> LAGB could be another explanation of the residual contrast of the slip planes in Figure 4.31. In α phases containing <c+a> LAGBs (Figure 4.26 and 4.31), the slip bands are more sparsely distributed and specifically arranged near the LAGB. In α laths without <c+a> LAGBs (Figure 4.25 and 4.29), the dislocations are more separated and homogenously distributed. <a> dislocations cross slip easily between prismatic and pyramidal planes. The existence of <c+a> LAGBs may affect the dislocation distribution due to their intercepting effect on the glissile dislocations. Although some slip bands insusceptibly go through the LAGBs, LAGBs act as grids to filter slip bands.

4.3.6. Conclusions

The heterogeneously distributed dislocations in the compressed specimen exhibit planar slip caused by the breakdown of SRO.

The grown-in <c+a> LAGBs were not moved by compression. They show weak hindering effect on the slip bands generated during compression, although some slip bands go straight though the LAGB. The slip bands are more sparsely distributed and specific arranged near the <c+a> LAGBs. Dislocations in the α laths without <c+a> LAGBs as are more separated and homogeneously distributed.

<a> type dislocations slip on both the prismatic and the first order pyramidal planes in the compressed sample. Mainly screw dislocations were observed. <a> dislocations were observed repeatedly cross slipping between the prismatic plane and the first order pyramidal plane.

Some dislocations on prismatic planes as well as pyramidal planes show unusual contrast when imaged with a $g = 0002$. Dislocation dissociation may cause fringe patterns in pyramidal planes. The cross-slipped dislocations dissociated into extended dislocations on prismatic planes, which may lead to strong residual contrast. The specific dislocation dissociation reaction need be analysed eventually.

Chapter 5. In-situ compression test in TEM

Three groups of pillars were compressed in-situ in TEM.

Group 1 pillars have the loading direction along $[12\bar{3}4]$, for single slip.

Group 2 pillars have the loading direction along $[\overline{20}8,12,7]$, for multiple slip.

Group 3 pillars have the loading direction along $[0001]$, for specific <c+a> slip

5.1. Group 1 pillars with the loading direction along $[12\bar{3}4]$

5.1.1. Preparation of the in-situ test pillars

The pillars in Group 1 were fabricated from the half TEM disc shown in Figure 5.1. The specific preparation method was introduced in Section 3.7.1. The whole TEM specimen belonged to the same grain. The orientation of the α laths was: horizontal direction X~$[\bar{5}053]$, vertical direction Y ~$[\bar{1}\bar{1}2\bar{3}]$, normal direction Z~$[7\overline{11}43]$ (X,Y,Z are shown in the schematic unit cell in Figure 5.1a). The EBSD map of the specimen is shown in Figure 5.1b. The loading direction of in-situ compression was approximately parallel to the vertical direction Y. Six pillars with different sizes of the same orientation were prepared, in order to investigate the effect of sample size upon the plastic deformation. Figure 5.2 shows images through the six pillars. The thickness of all pillars is around 0.5μm, which is not shown in this view. Pillars 1 & 2 are rectangular with standard dimensions about 0.5×1.1×2.1μm. Pillars 4 & 6 are also rectangular but smaller. Pillars 3 & 5 are trapezoid. All the pillars contained only α phase except Pillar 3 which was α/β/α lamellar.

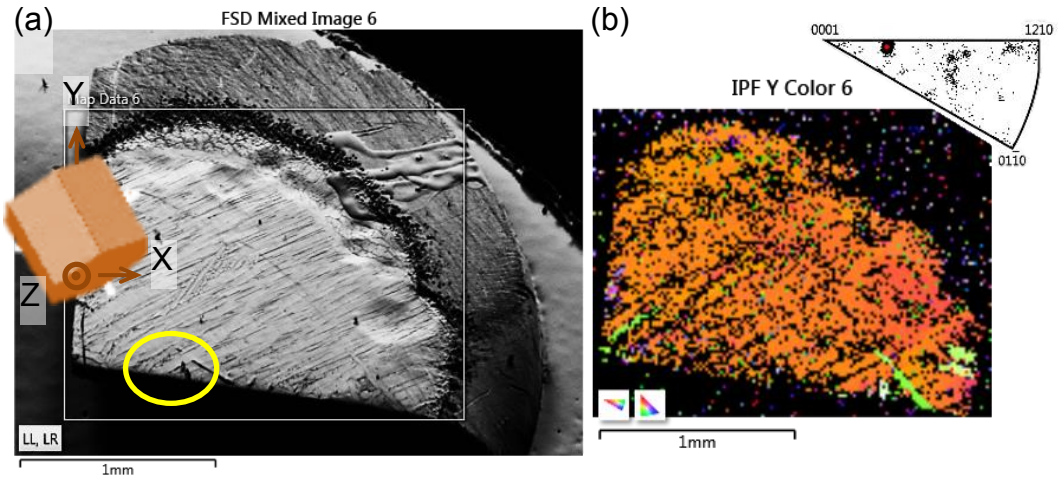

Figure 5.1 (a) SEM image of the TEM disc. The inset schematic cell illustrates the orientation of the α phase: X~$[\bar{5}053]$, Y~$[\bar{1}\bar{1}2\bar{3}]$, Normal~$[7\bar{1}\bar{1}43]$. (b) EBSD mapping of the specimen in the vertical direction Y.

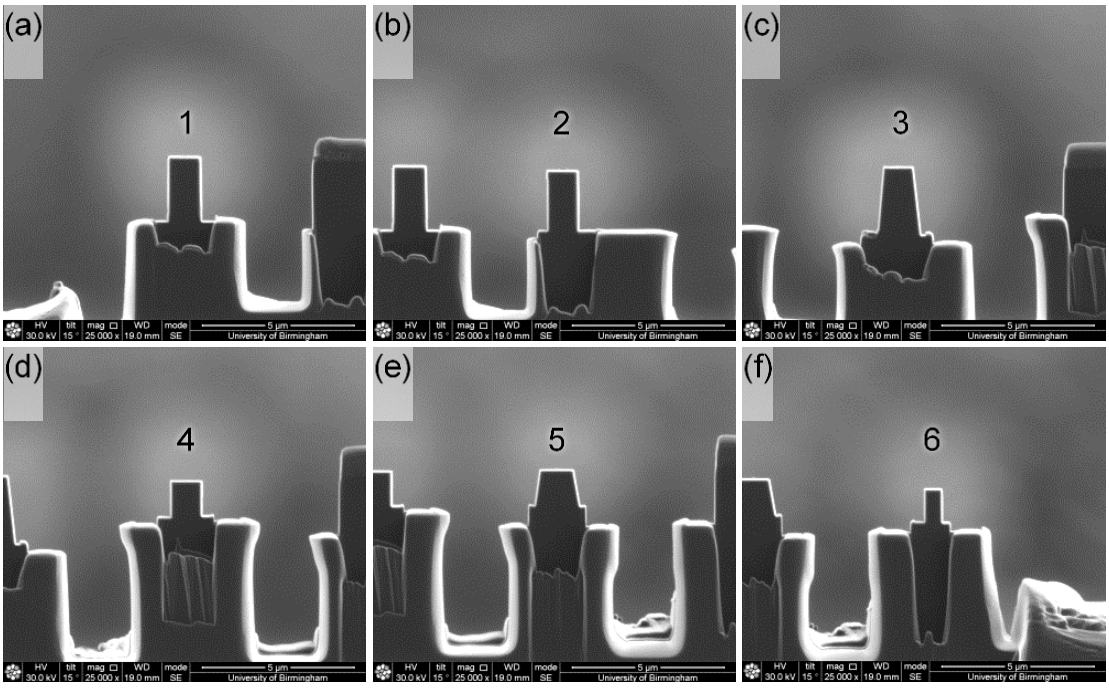

Figure 5.2 (a)-(f) are SEM images of the vertical sections of six pillars in Group 1

The dimensions of the six pillars are shown in Table 5.1. For Pillars 3&5, the length of the upper side of the trapezium is 1.1μm, while the lower edge was 1.45μm. The trapezoid shape was selected as a comparison task to avoid the stress concentration appeared in rehearsals at bottom corners of pillars. Since the slip system in Group 1 was easily activated, there was not obvious stress concentration observed at bottom corners of pillars.

Table 5.1 Dimensions of the pillars in Group 1

pillar	dimensions	pillar	dimensions
1	500nm x 1.1μm x 2.1μm	4	480nm x 1μm x 1.2μm
2	500nm x 1.1μm x 2.1μm	5	480nm x $\frac{1.1}{1.45}$μm x 1.2μm
3	480nm x $\frac{1.1}{1.45}$μm x 2μm	6	480nm x 0.5μm x 1.2μm

Figure 5.3a is a TEM image of Pillar 1. The two accessible beam directions were $\mathrm{B}_1 = [4\bar{1}\bar{1}76]$ and $\mathrm{B}_2 = [11\bar{1}\bar{3}2,3]$ (Figure 5.3b and c). These high-indexed zone axes were inferred by the known indices in the diffraction patterns. The contact plane was $\mathrm{P}_0 = \mathrm{B}_1 \times \mathrm{B}_2 = (47\bar{1}\bar{1}23)$. The loading direction was therefore $[8,14\bar{2}\bar{2}27] \approx [12\bar{3}4]$. Under the above loading condition, slip systems with Schmid factors larger than 0.3 are listed in Table 5.2. Among all the slip systems, $[11\bar{2}0](0002)$ has the largest Schmid factor and is the most likely slip system.

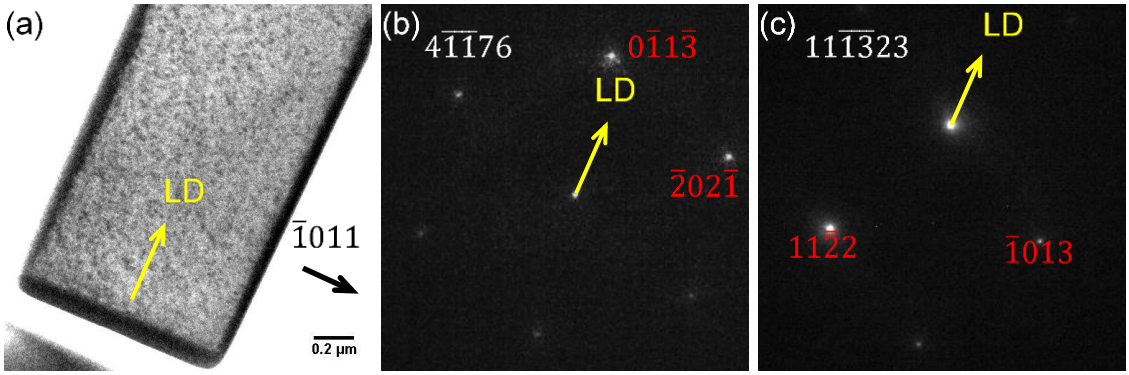

Figure 5.3 (a) Bright field image of Pillar 1 using $\bar{1}011$ reflection, $\mathrm{BD} \sim [2\bar{3}11]$. The loading direction $[12\bar{3}4]$ was along the long axis of the pillar. (b) and (c) are diffraction patterns of two zone axes which were parallel to the beam directions $[4\bar{1}\bar{1}76]$ and $[11\bar{1}\bar{3}23]$. The arrows indicate the loading direction.

Table 5.2 Slip systems with Schmid factors m >0.3

Burgers vector	Slip plane	m	Burgers vector	Slip plane	m	Burgers vector	Slip plane	m
$\frac{1}{3}[11\bar{2}0]$	(0001)	0.48	$\frac{1}{3}[\bar{1}\bar{1}23]$	$(01\bar{1}1)$	0.31	$\frac{1}{3}[1\bar{2}13]$	$(\bar{1}2\bar{1}2)$	0.35
$\frac{1}{3}[\bar{1}2\bar{1}0]$	(0001)	0.31	$\frac{1}{3}[\bar{1}\bar{1}23]$	$(11\bar{2}2)$	0.33	$\frac{1}{3}[\bar{2}113]$	$(10\bar{1}1)$	0.44
$\frac{1}{3}[\bar{1}2\bar{1}0]$	$(10\bar{1}1)$	0.31	$\frac{1}{3}[1\bar{2}13]$	$(01\bar{1}1)$	0.41	$\frac{1}{3}[\bar{2}113]$	$(2\bar{1}\bar{1}2)$	0.34
$\frac{1}{3}[2\bar{1}\bar{1}3]$	$(\bar{1}101)$	0.36						

5.1.2. Dislocation motion

Pillar 2 was compressed in displacement control mode with a maximum displacement of 50nm. The operation of $\frac{1}{3}[11\bar{2}0]$ basal slip in Pillar 2 was recorded during straining (Figure 5.4). Detail dislocation analysis is in section 5.1.4. The still images extracted from the video (supplementary movie 2) are shown in Figure 5.4 in chronological order. The video is obtained with $\mathrm{g} = \bar{1}011$. The arrows in each frame indicate the position where fresh dislocation motion takes place after the former frame.

Before compression (Figure 5.4a), bend contours exist in the pillar as marked by arrows. In the elastic deformation stage, bend contours move from the middle (Figure 5.10b) to the side (Figure 5.4c) of the pillar. The first dislocation generates from the probe/pillar interface in Figure 5.4d and expands on its slip plane in Figure 5.4e. A second dislocation emits from the contact surface on another basal plane in Figure 5.4f. In Figure 5.4g, both dislocations in the two basal planes expand. In Figure 5.4h, two more dislocations glide on the first activated basal plane and expand in Figure 5.4i. In Figure 5.4j, the probe/pillar contact surface releases a burst of dislocations on a third basal plane and the dislocation half loops expand rapidly in Figure 5.4k. The array of dislocations in each basal plane reaches the top free surface of the pillar as labelled in Figure 5.4l. Figure 5.4m shows an image taken at the peak of the loading curve. However, the dislocations are haft in Figure 5.4n when the load slightly declines. Figure 5.4o shows dislocations in Pillar 2 after compression.

The probe/pillar contact surface emitted more than 10 dislocations in the same directions on three basal planes. Plastic deformation starts at 41.7s. The first two

dislocations expand slowly at the beginning. An array of dislocations follows the first generated dislocation before it passes through the pillar to the right free surface. The front end of the first dislocation keeps moving forward inside pillar during the whole test. The emission of new dislocations speeds up from 57.26s with the same strain rate. Dislocations stop expanding when the load is decreased slightly from the peak.

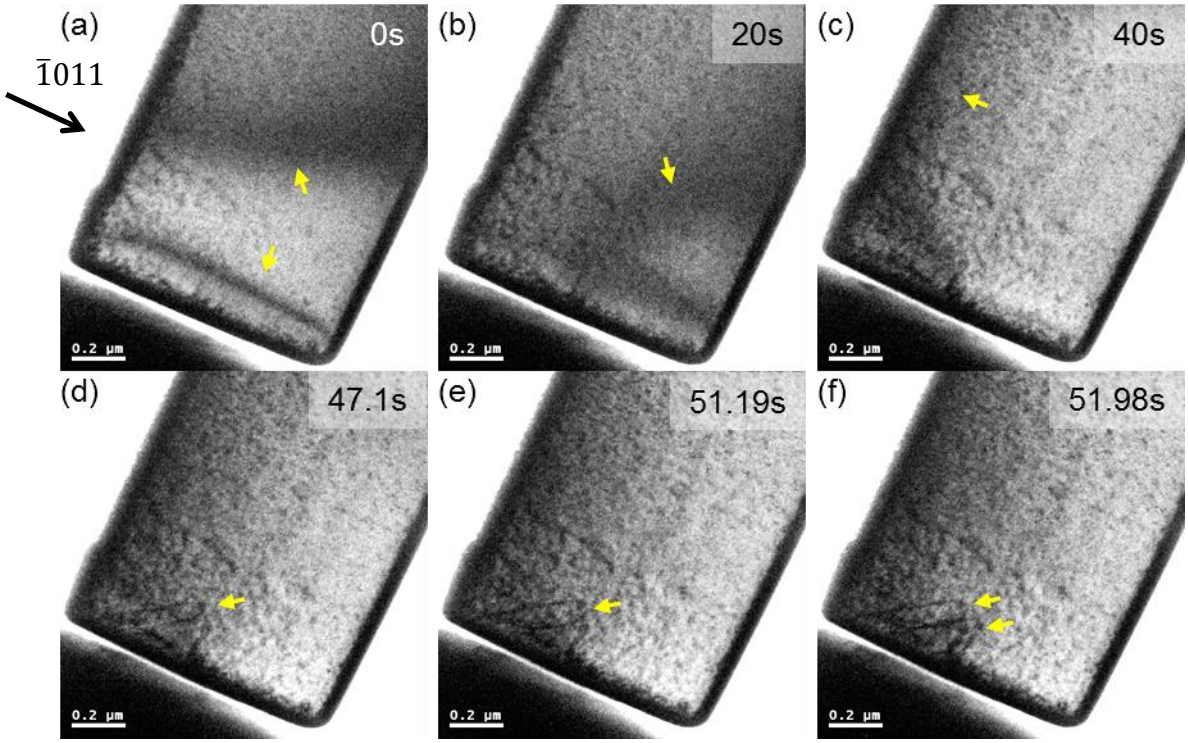

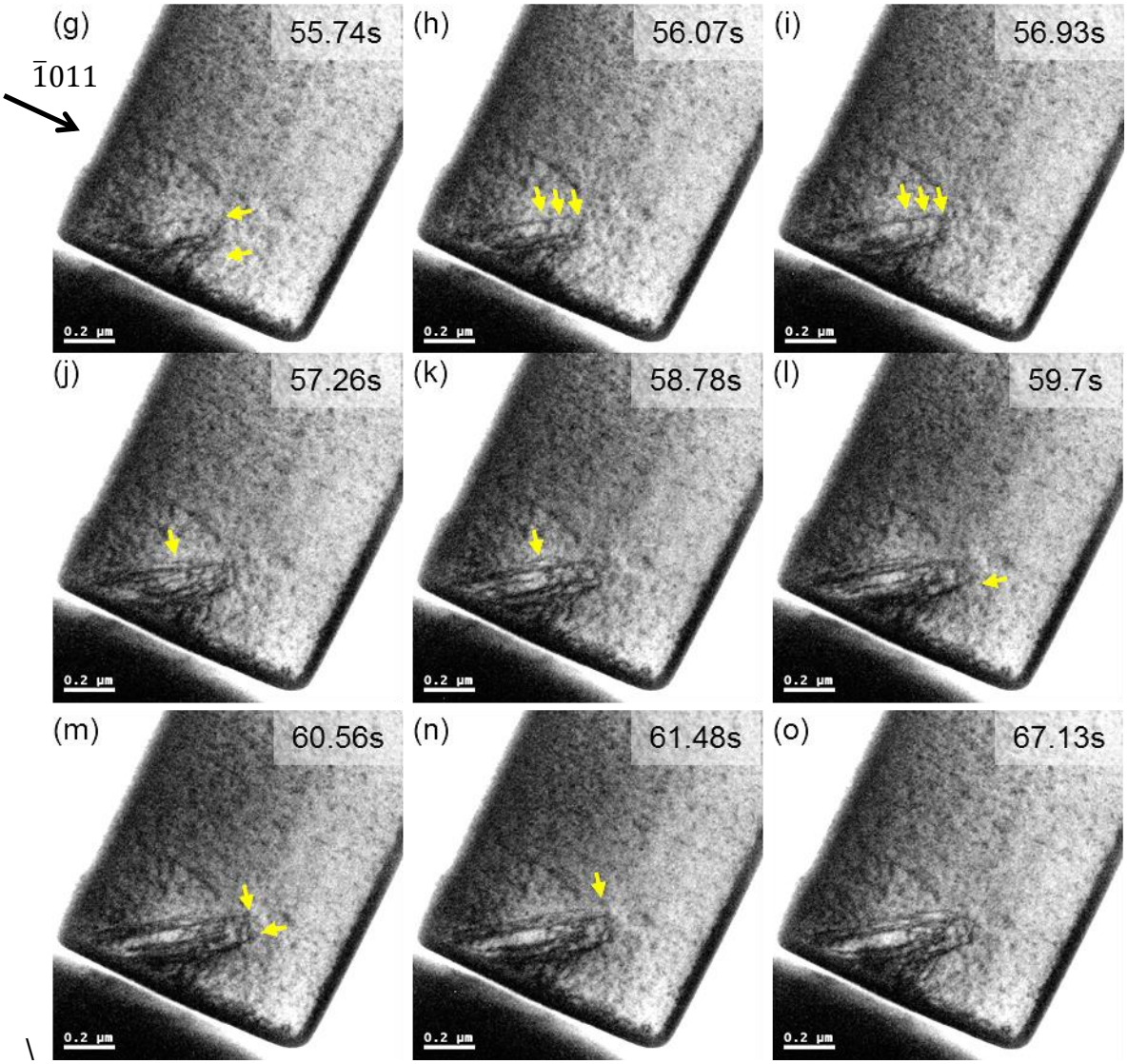

Figure 5.4 (a-o) TEM images of Pillar 2 are video frame images captured during compression in chronological order. $g = \bar{1}011$, $BD \sim [2\bar{3}11]$. (a and o) show the pillar before and after compression. (b and c) shows bend contours at 20s and 40s during elastic deformation. (d and e) The first dislocation appears and expands. (f and g) The second dislocation generates on another basal plane and expands. (h and i) another two dislocations propagate from the first source and expands. (j and k) The probe/pillar contact surface releases a burst of dislocations in a third basal plane and dislocations expand rapidly. (l) The array of dislocations in the same plane reaches the top free surface. (m) shows dislocations imaged at the peak of the loading curve. (n) Dislocations stop when the load was slightly decreased.

5.1.3. Mechanical behaviour

During the tests, dislocations were observed generating firstly from the contact surface between the flat punch and the pillar and then propagating into the sample. Take Pillar 1 for instance: three sequential bright field images (Figure 5.5a-c) using the $\bar{1}011$ reflection indicate how the dislocations were generated. Pillar 1 was compressed twice using loading force 350μN and then 500μN. Figure 5.5a was taken before compression. Figure 5.5b and 5.5c were taken after the first and second compressions respectively. The loading direction was $[12\bar{3}4]$. Figure 5.5d shows the stress-stain curves. The origin of the second compression has been moved to the termination of the first compression. The result shows that the loading segment of the second compression is coincident with the unloading segment of the first.

In the first stress-stain curve (black), point A was the critical point where dislocations started to appear. Pillar 1 was under elastic deformation in segment OA, and plastic deformation from point A to the end point B.

In the second compression curve (red), the dislocations activated during the first compression started to move slowly again from point C. After point D, the dislocations moved more quickly. More dislocation lines were emitted and glided quickly in the same plane after point E. From point F on, the dislocations sped up dramatically and cross slipped to another basal plane, as can be inferred from the two slip traces marked 1&2 in Figure 5.8d. The low mobility of dislocations and their pile-up contributes to the significant work hardening of the sample. The average strain rate was $0.33\times10^{-3}s^{-1}$.

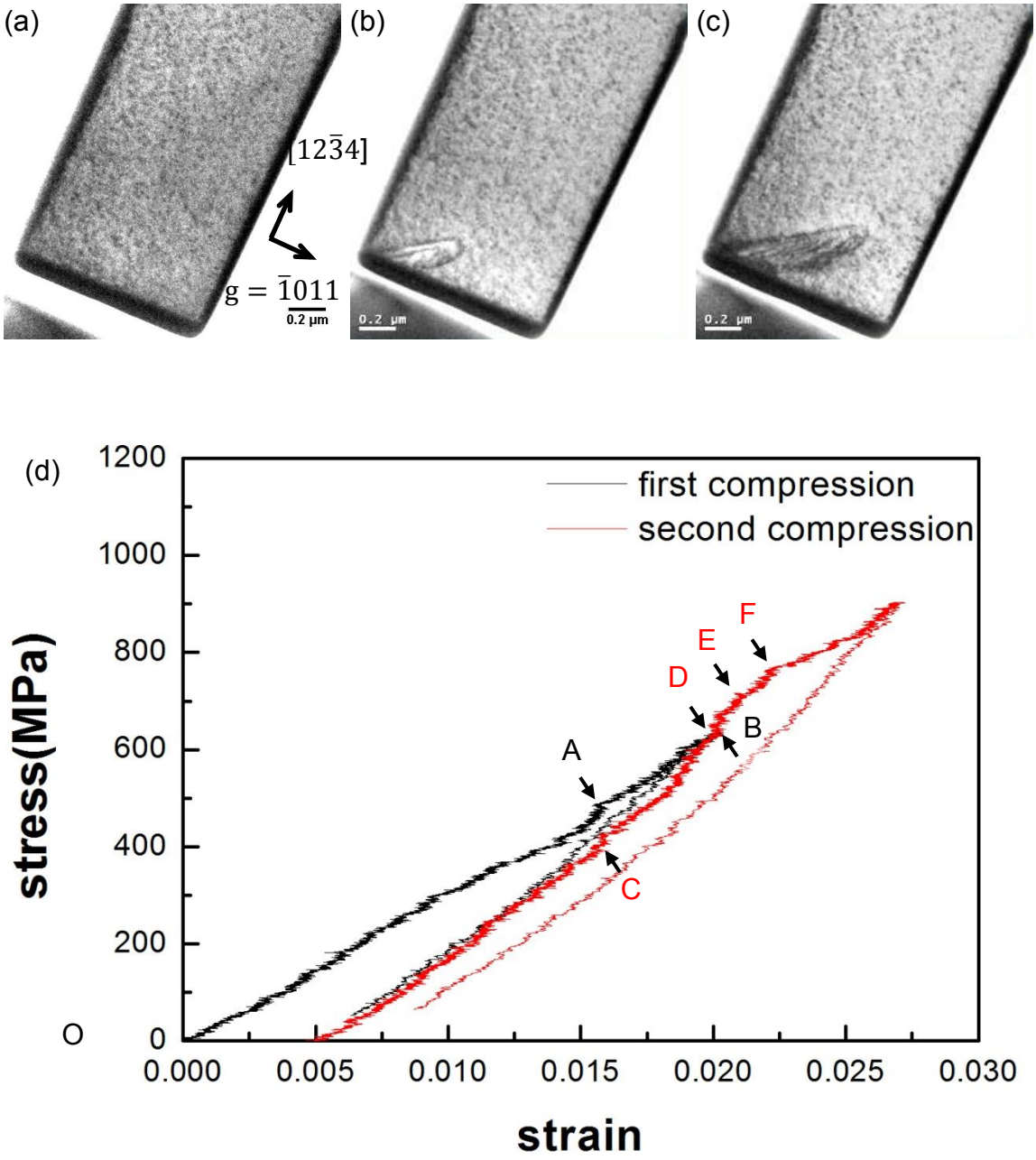

Figure 5.5 (a - c) Sequential TEM images taken during in-situ TEM compression with the stress-stain curves shown in (d). $g = \bar{1}011$, $BD \sim [2\bar{3}11]$. Before the compression test there is no dislocation in (a). Dislocations generated at the probe/sample interface and propagated into the pillar in (b) and (c). (d) The two stress-stain curves represent two compression tests.

Pillar 6 underwent the largest deformation of the six pillars in Group 1. The total strain was approximately 9%. The control mode for Pillar 6 was displacement control. The strain rate was about 1×10^{-3} s^{-1}. Figure 5.6 shows the compressed pillar 6 and the stress-strain curve recorded during compression. Detailed observations of the deformation are shown in Figure 5.7 using still images extracted from the recorded in-situ video and corresponding to the typical data points A to R marked on the stress-strain curve (Figure 5.6b). The full video is available in the attached CD as supporting information. The images are obtained at a high tilt angle (-17.4°) when $\mathrm{g} = \bar{1}\bar{1}22$.

Point A and point R are the start and end points of the curve, corresponding to Figures 5.7a and 5.7r, respectively. In segment AB (Figure 5.6b), Pillar 6 is under elastic deformation. The first dislocation started to glide from the probe/pillar interface at point B (Figure 5.6b) as marked in Figure 5.7b. In segment BC, plastic deformation gradually proceeds. The first dislocation expands on its slip plane and a new dislocation is activated on another basal plane (Figure 5.7c). In segment CD, a large number of dislocations generate from the contact surface and go through the pillar to the right side surface, until the lower-right corner of Pillar 6 was full of dislocations (Figure 5.7d). In the flat segment DE, the lower-right corner full of dislocations shears and forms a small step on the right surface (labelled in Figure 5.7e). Then the slip step grows rapidly (Figure 5.7f) as shear deformation increases and the load drops slightly in segment EF. At point G (Figure 5.6b), a new slip band initiates from the upper-right corner of the pillar and moves to the left side surface as marked in Figure

5.7g. After that, the probe/pillar contact surface releases a burst of dislocations again until point H. The strain burst at point I and load drop at point J correspond to the increase of a small slip step (Figure 5.7i) and large step (Figure 5.7j). Double-headed arrows show the step size. At point K, another slip band emits from the left surface to the right surface of the pillar in the middle of Pillar 6 as labelled in Figure 5.7k. In segment KL, the dislocation source at the contact surface releases dislocations again accompanied by further shear deformation (labelled in Figure 5.7l). The slip step enlarges in Figure 5.7m and 5.7n corresponding to the stain burst at point M and load drop at point N. At point O, a fourth slip band appears as labelled in Figure 5.7o. Dislocations glide from left to right. In segment OP, the shear deformation of the lower-right corner increases. The dislocations on the upper basal plane (marked in Figure 5.7p) expand at the same time. Then the curve becomes flat with a little drop in segment PQ due to the further shear deformation (Figure 5.7q).

Generally, in the ascent stages of the curve (BD, FH, JL and NP), dislocations generate at the front part of the pillar in contact with the probe. The flat segments (DE, JI, LM and PQ) start when dislocations arrive at the right free surface of the pillar. Slip results in the formation of steps on the free surface of the pillar and slightly relieve the strain. The front part keeps shearing when more steps generate as marked by the dotted red lines F, J, N and Q in Figure 5.6a, which led to little drops in the curve (EF, IJ and MN). In segments FH, JL and NP, there are critical stresses (G, K and O) where new slip is activated at other positions of the pillar arrowed 2, 3 and 4 in Figure 5.6a.

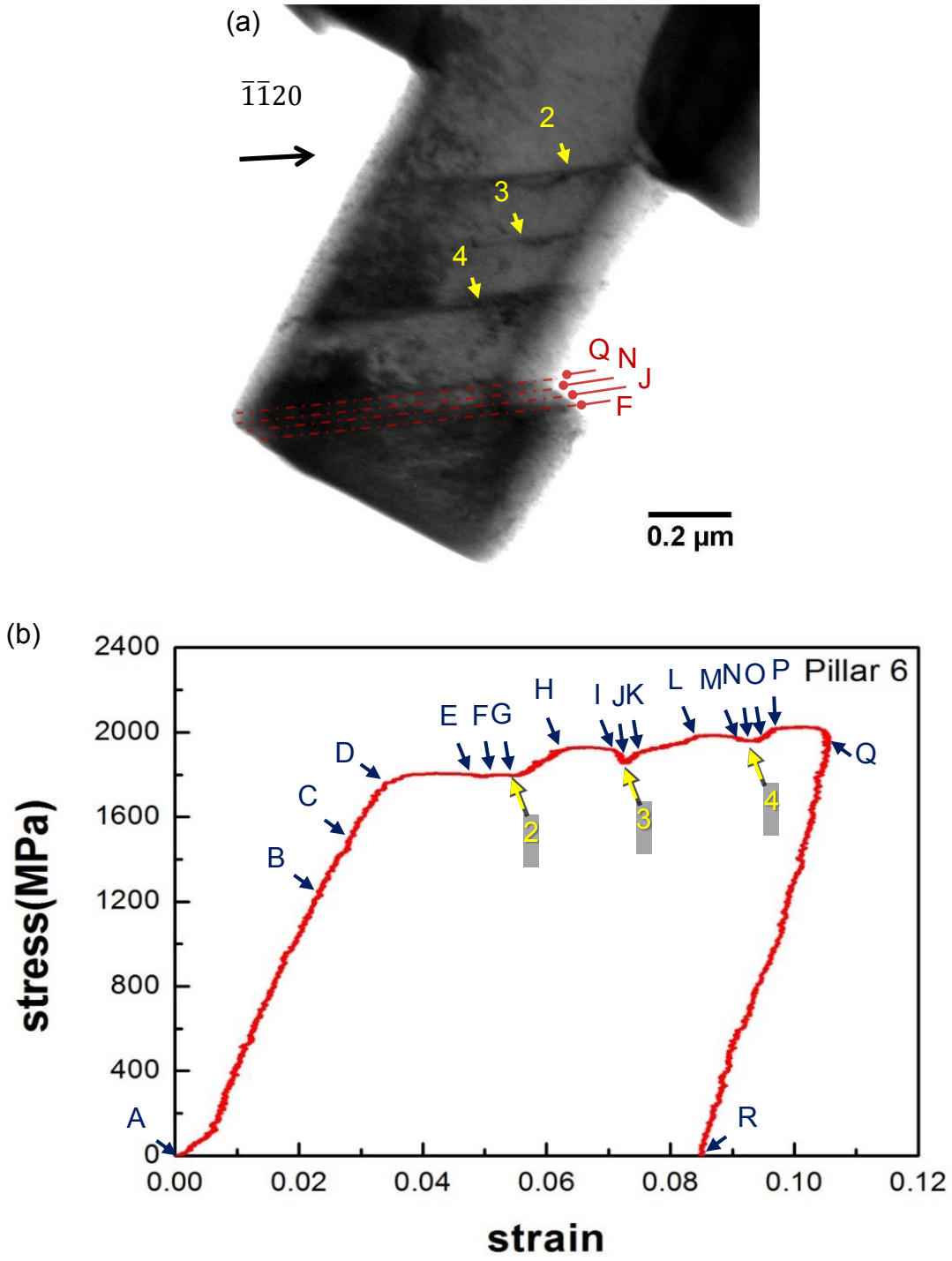

Figure 5.6 (a) Bright field image of Pillar 6 showing the slip bands generated. $\mathrm{g} = \bar{1}\bar{1}20$, $\mathrm{BD} \sim [1\bar{1}00]$. (b) The corresponding stress-strain curve for Pillar 6. The upper case letters correspond to their lower case equivalents in Figure 5.7.

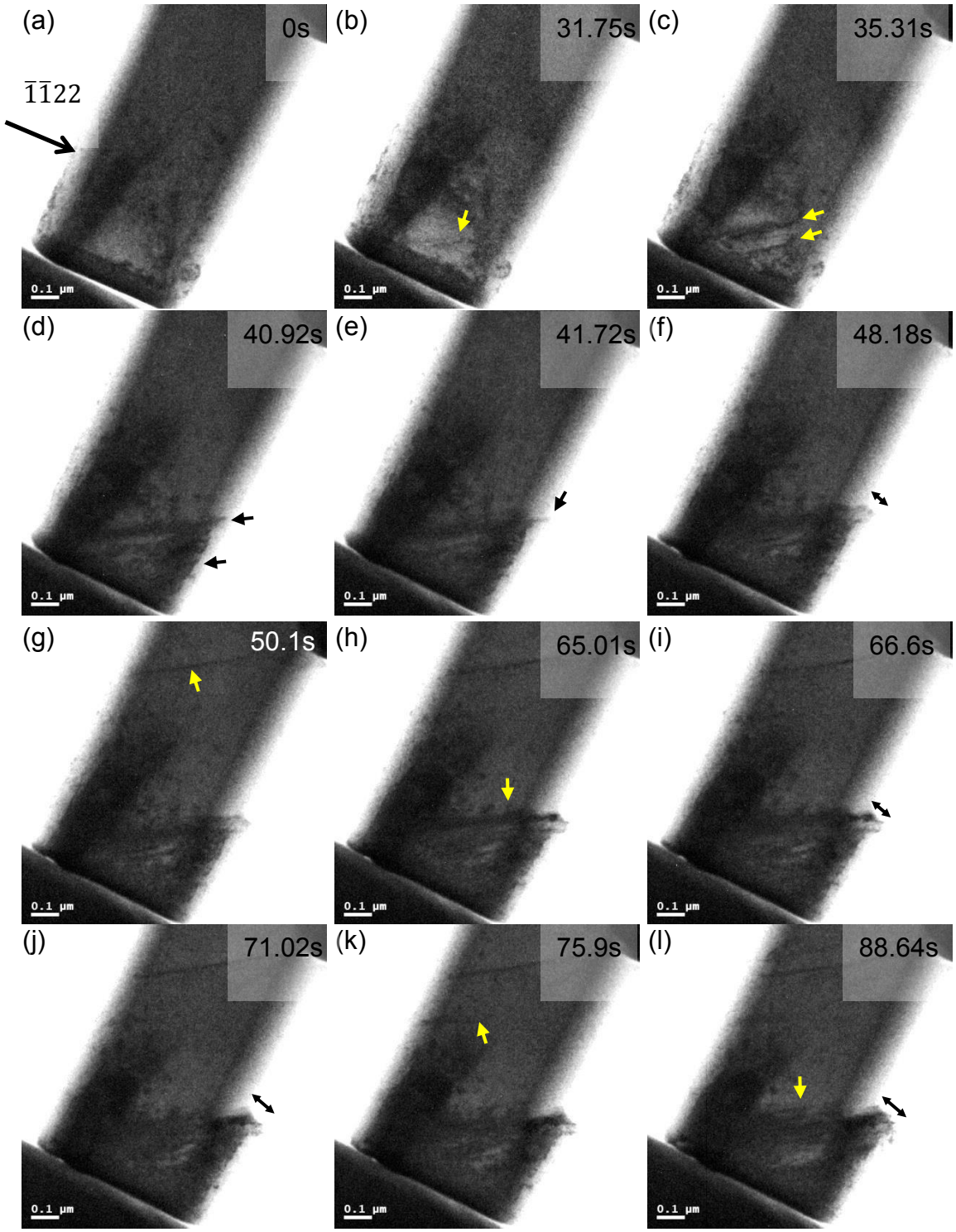
(a)
0s
$\bar{1}\bar{1}122$
(b)
31.75s
(c)
35.31s
(d)
40.92s
(e)
41.72s
(f)
48.18s
(g)
50.1s
(h)
65.01s
(i)
66.6s
(j)
71.02s
(k)
75.9s
(l)
88.64s
0.1 μm

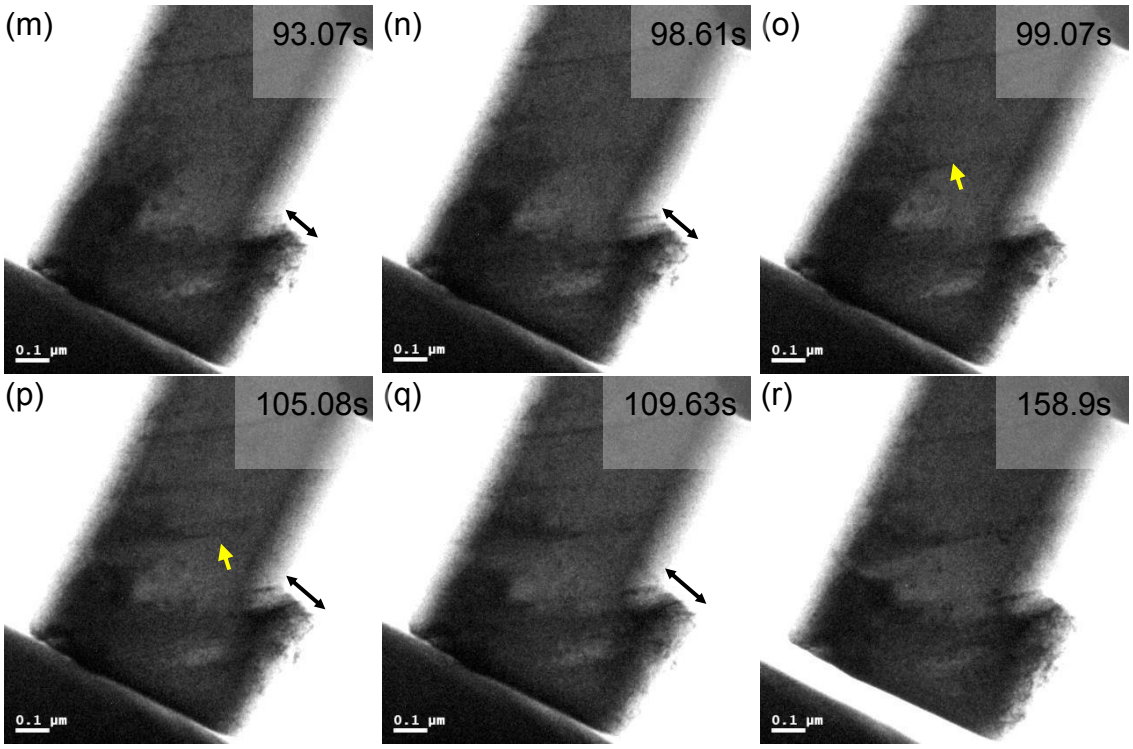

Figure 5.7 (a-r) TEM images of Pillar 6 are video frame images captured during compression in time sequence. $g = \bar{1}\bar{1}22,\ BD \sim [1\bar{1}00]$. (a and r) show the pillar before and after compression. (b, g, k and o) show the formation of dislocation sources at different positions of the pillar with increasing strain. (c and d) show dislocations gliding in the lower-right corner until (e) the first slip step appears on the right free surface of the pillar. (f) shows the slip step size increasing. (h, l and p) the source at the probe/pillar contact surface emits more dislocations until (i, m and q) slip steps form again and enlarge in (j, n).

Table 5.3 shows the comparison of Pillar 1 and Pillar 6. The mechanical properties are reserved from stress-strain curves in Figure 5.5 and 5.6.Two stress-strain curves of Pillar 1 in Figure 5.5 are combined and treated as one curve. The true elastic limit is the lowest stress at which first dislocation move. Pillar 6 has much larger true elastic limit than Pillar 1. It may be connected with the smaller size of Pillar 6, which restricts the activation of dislocations. Stress is proportional to strain up to the proportionality limit. The elastic limit in Table 5.3 is the start of permanent

deformation. The elastic limit of Pillar 1 is close to the standard level of bulk sample [1]. All the stress limits for Pillar 6 are much higher than bulk sample. Theoretically, the elastic modulus (E) should be the same for Pillar 1 and 6 with the same loading direction. However, E of Pillar 1 is smaller than Pillar 6. The inappropriate alignment of Pillar 1 might introduce unexpected elastic deformation which decreased the elastic modulus.

Table 5.3 Comparison of properties of Pillar 1 and Pillar 6

pillar	1	6
dimensions	500nm x 1.1μm x 2.1μm	480nm x 0.5μm x 1.2μm
Loading direction	$[12\bar{3}4]$	$[12\bar{3}4]$
Control mode	Load control	Displacement control
Strain rate	$0.33\times10^{-3}s^{-1}$	$1\times10^{-3}s^{-1}$
True elastic limit	500MPa (Figure 5.5 Point A)	1200MPa (Figure 5.6 Point B)
Proportionality limit	620MPa (Figure 5.5 Point D)	1500MPa (Figure 5.6 Point C)
Elastic limit	750MPa (Figure 5.5 Point F)	1750MPa (Figure 5.6 Point D)
0.2 Proof stress	900MPa (Figure 5.5 peak point)	1800MPa
E	32GPa	66.6GPa

5.1.4. Dislocation analysis

The same types of dislocations were activated in all Group 1 pillars. Take Pillar 1 as an example of analysing the dislocations. Figure 5.8 indicates the same area of Pillar 1 with different reflection vectors g before (a-c) and after (d-g) compression. The new dislocations slip on basal planes labelled 1 and 2 in Figure 5.8d. According to the $\vec{g} \cdot \vec{b} = 0$ invisibility criterion, dislocations invisible with 0002 (Figure 5.8d) and $1\bar{1}0\bar{1}$ (Figure 5.8g) reflections have a Burgers vector of $\frac{1}{3}[11\bar{2}0]$. The experimental result agrees well with the expected activated slip system. Figure 5.9 to Figure 5.13 show a_3 basal slip in Pillar 2 to Pillar 6. In each figure, the first three bright field images (a-c) are of pillars before compression and the last three images (d-f) show pillars after compression.

Different diffraction conditions were used on Pillar 5 (Figure 5.12) during compression to determine the best imaging condition. Finally, a two beam condition ($g = \bar{1}011$) was chosen, where the reflection plane is parallel to the loading direction. This was also the beam condition used for Pillar 1 to Pillar 4. Pillar 6 was imaged using the reflection vector $g = \bar{1}\bar{1}22$, which is also perpendicular to the loading direction. The viewing g vector perpendicular to the loading direction helps to minimise the bend contours during the compression. The pre-existing <a> dislocations in Pillar 5 (Figure 5.12b and 5.12c) did not move during the compression.

Pillar 2 (Figure 5.9) was in the same condition as Pillar 1; same size and dislocation-free before compression. So, the new dislocations have similar configurations to those in Pillar 1. a_3 dislocations slip on basal planes labelled 1, 2 and 3 in Figure 5.9d. In Pillar 3 (Figure 5.10), the activated a_3 moved nearly parallel to the α/β interface. It was not observed that dislocations went through the α/β interface. a_3 dislocations are labelled in Figure 5.10e. Larger strains were applied on Pillar 4 (Figure 5.11) and Pillar 6 (Figure 5.13) with smaller size, 80nm and 100nm, respectively. There was a large shear of the front part in Pillar 4 (labelled in Figure 5.11f) and several slip bands in Pillar 6 (labelled in Figure 5.13f). However, only one slip system, a_3 basal, was activated.

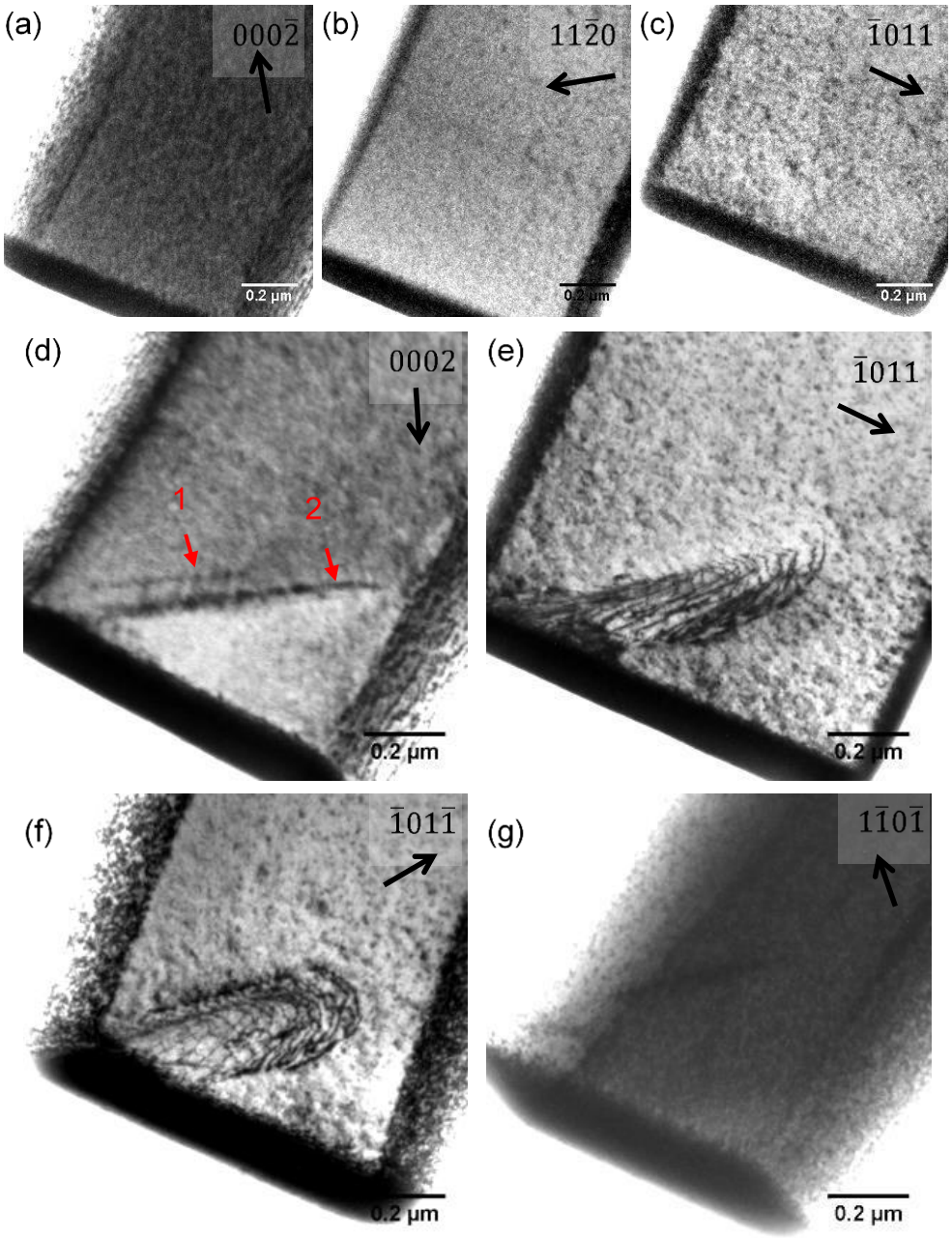

Figure 5.8 (a-c) Bright field TEM images showing the same area of Pillar 1 with different g vectors before the compression. After the compression, a_3 dislocations were activated which are invisible in (d) (g), and visible in (e) (f). (a) $g = 000\bar{2}$, $BD \sim [6\bar{5}\bar{1}0]$ (b) $g = 11\bar{2}0$, $BD \sim [1\bar{1}00]$ (c) $g = \bar{1}011$, $BD \sim [2\bar{3}11]$ (d) $g = 0002$, $BD \sim [1\bar{1}00]$ (e) $g = \bar{1}011$, $BD \sim [5\bar{7}23]$ (f) $g = \bar{1}01\bar{1}$, $BD \sim [2\bar{7}53]$ (g) $g = 1\bar{1}0\bar{1}$, $BD \sim [0\bar{1}11]$

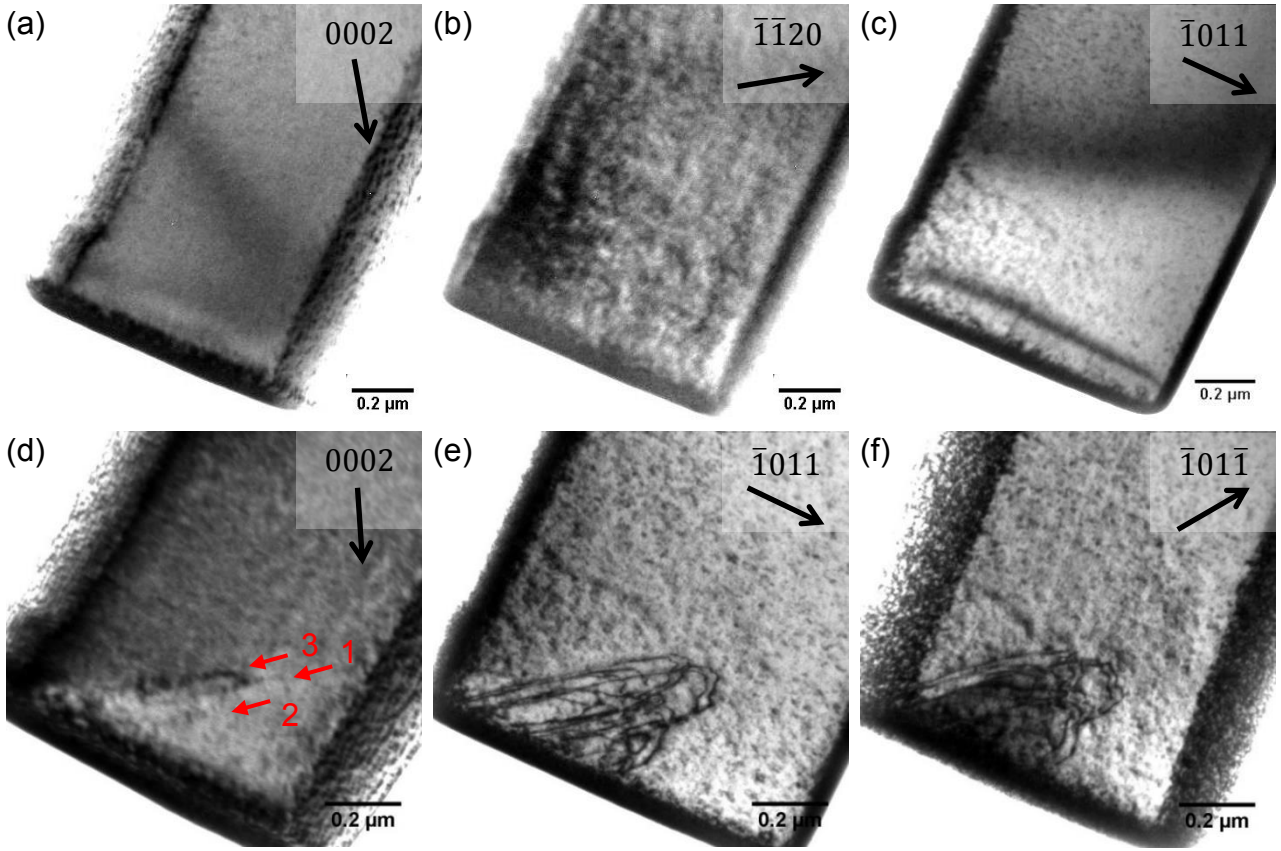

Figure 5.9 (a-c) Bright field images of Pillar 2 before compression. (d-f) a_3 basal slip activated after compression. (a) $g = 000\bar{2}$, $BD \sim [6\bar{5}\bar{1}0]$ (b) $g = 11\bar{2}0$, $BD \sim [1\bar{1}00]$ (c) $g = \bar{1}011$, $BD \sim [2\bar{3}11]$ (d) $g = 0002$, $BD \sim [1\bar{1}00]$ (e) $g = \bar{1}011$, $BD \sim [5\bar{7}23]$ (f) $g = \bar{1}01\bar{1}$, $BD \sim [2\bar{7}53]$

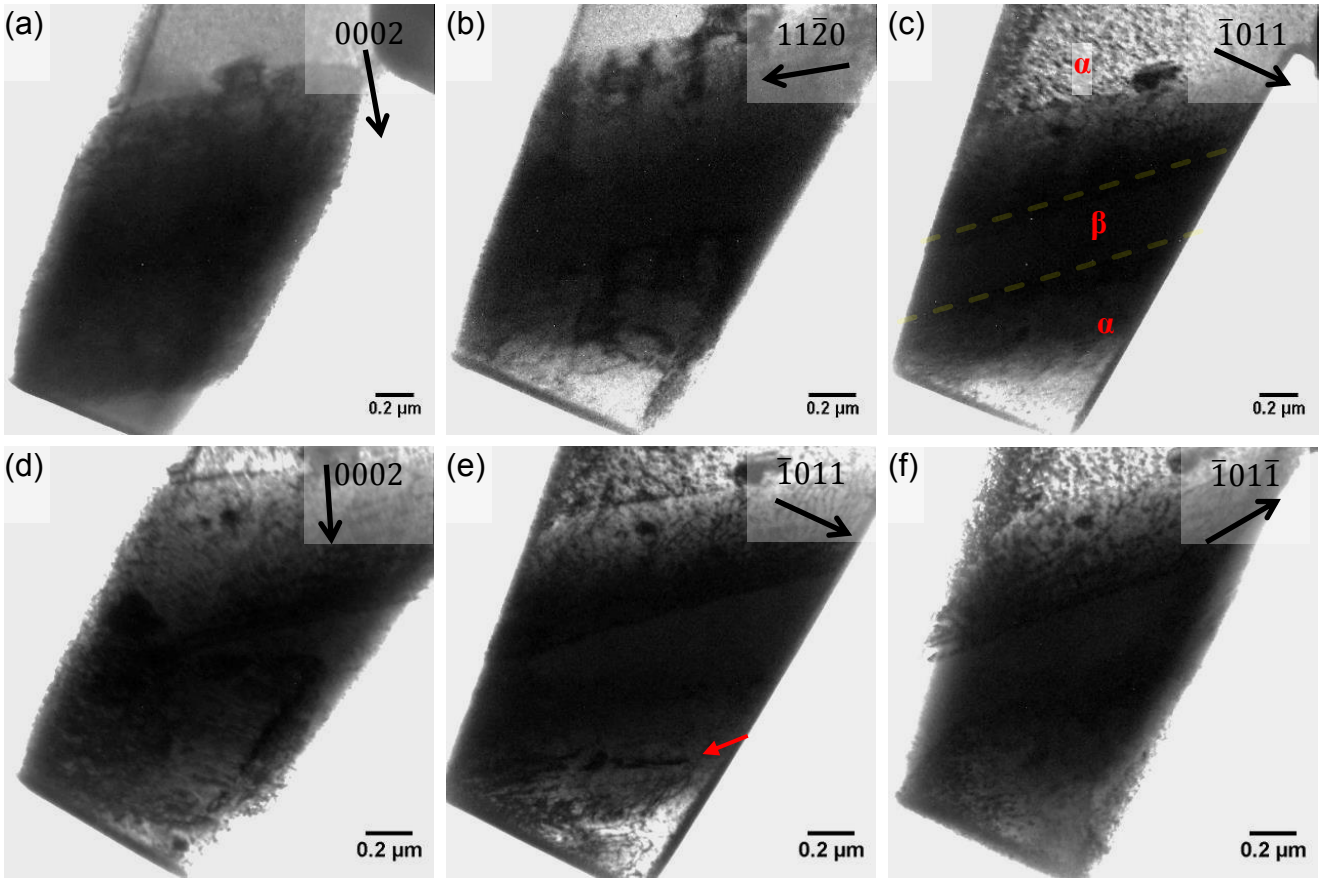

Figure 5.10 (a-c) Pillar 3 before the compression. The interfaces of α/β/α are labelled by dashed lines in (c). (d-f) The activated a_3 dislocations labelled by arrow more parallel to the α/β interface after the compression. (a) $g = 0002$, $BD \sim [6\bar{5}\bar{1}0]$ (b) $g = 11\bar{2}0$, $BD \sim [1\bar{1}00]$ (c) $g = \bar{1}011$, $BD \sim [2\bar{3}11]$ (d) $g = 0002$, $BD \sim [1\bar{1}00]$ (e) $g = \bar{1}011$, $BD \sim [5\bar{7}23]$ (f) $g = \bar{1}01\bar{1}$, $BD \sim [2\bar{7}53]$

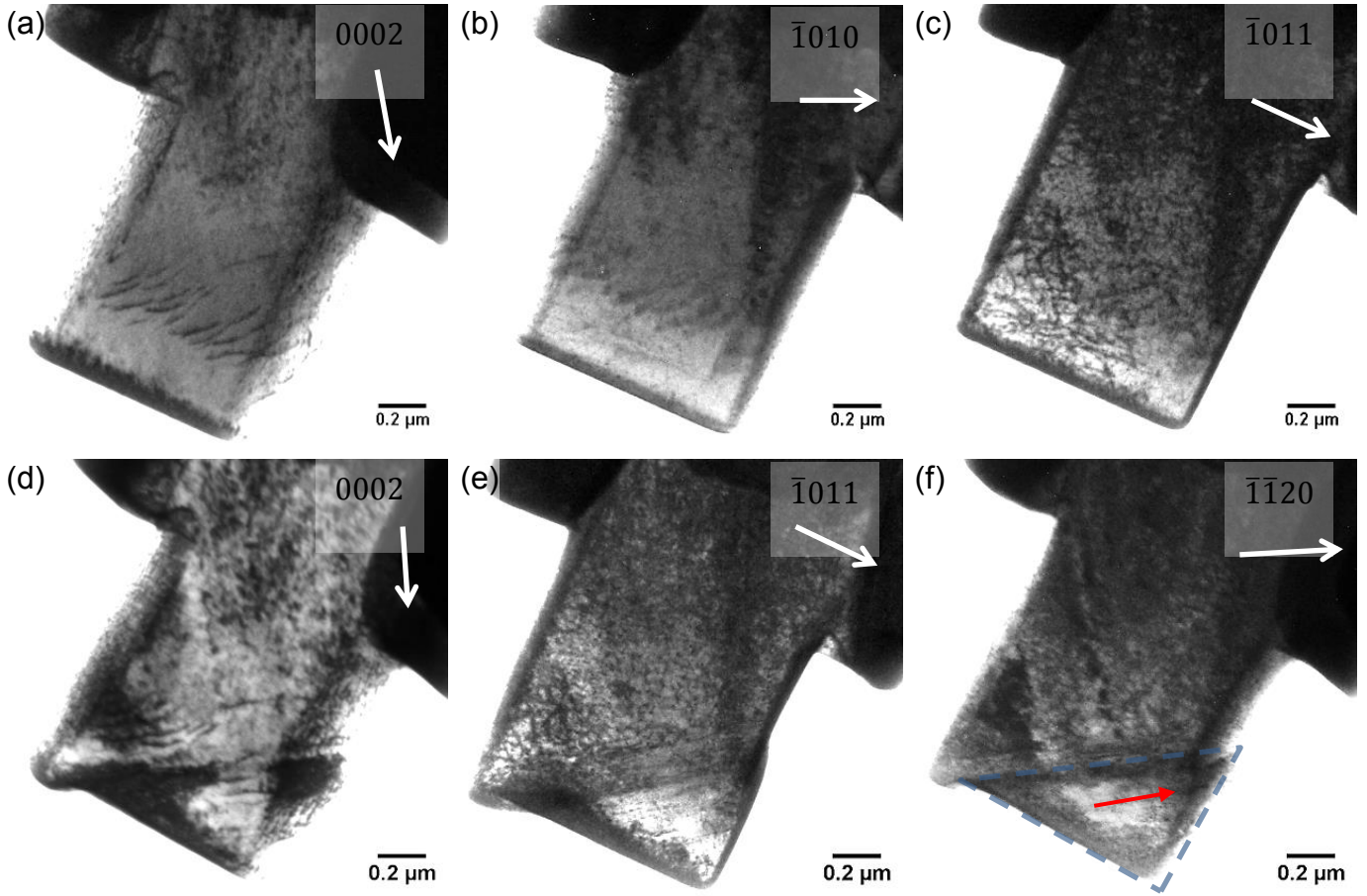

Figure 5.11 Pillar 4 before (a-c) and after (d-f) compression. The front part of the pillar is sheared as indicated in (f). (a) $g = 0002$, $BD \sim [6\bar{5}\bar{1}0]$ (b) $g = \bar{1}010$, $BD \sim [1\bar{2}11]$ (c) $g = \bar{1}011$, $BD \sim [2\bar{3}11]$ (d) $g = 0002$, $BD \sim [1\bar{1}00]$ (e) $g = \bar{1}011$, $BD \sim [5\bar{7}23]$ (f) $g = \bar{1}\bar{1}20$, $BD \sim [1\bar{1}00]$

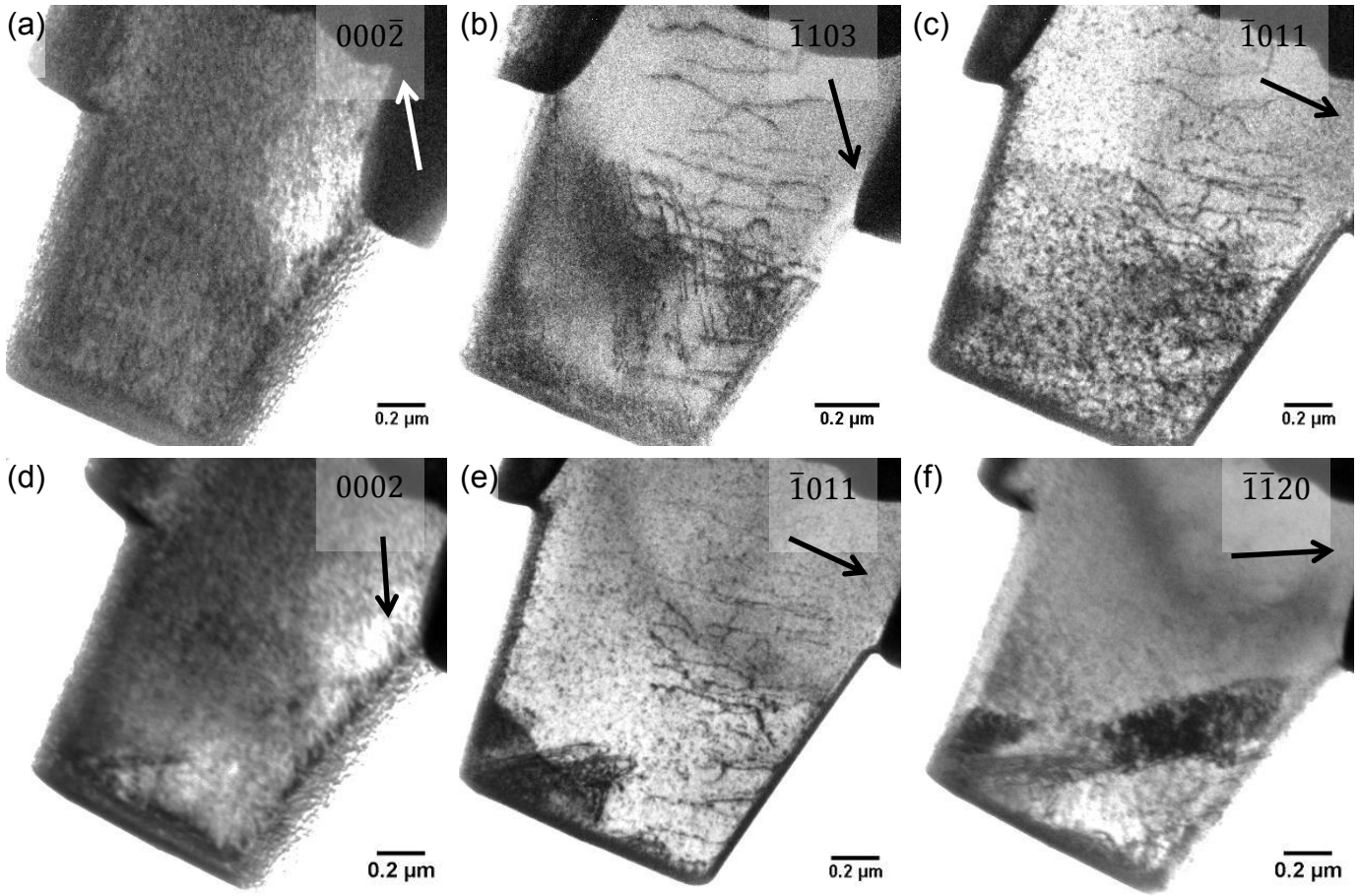

Figure 5.12 Pillar 5 before (a-c) and after (d-f) compression. The pre-existing <a> dislocations did not move. (a) $g = 000\bar{2}$, $BD \sim [6\bar{5}\bar{1}0]$ (b) $g = \bar{1}103$, $BD \sim [1\bar{2}11]$ (c) $g = \bar{1}011$, $BD \sim [2\bar{3}11]$ (d) $g = 0002$, $BD \sim [1\bar{1}00]$ (e) $g = \bar{1}011$, $BD \sim [5\bar{7}23]$ (f) $g = 1\bar{1}20$, $BD \sim [1\bar{1}00]$

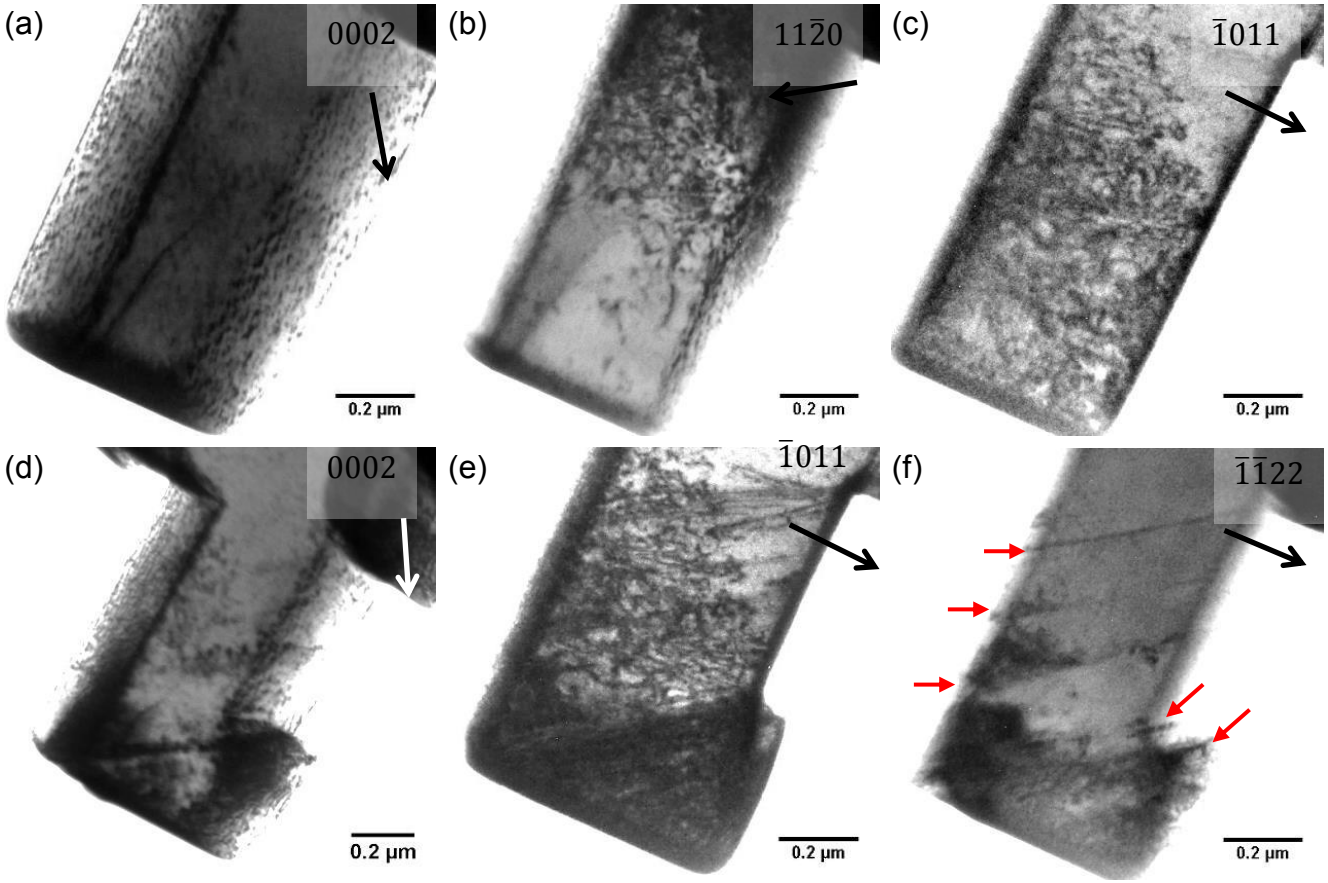

Figure 5.13 Pillar 6 before (a-c) and after (d-f) compression. Arrows in (f) label different positions of the pillar where a_3 basal slip was activated.
(a) $g = 0002$, $BD \sim [6\bar{5}\bar{1}0]$ (b) $g = 11\bar{2}0$, $BD \sim [1\bar{1}00]$ (c) $g = \bar{1}011$, $BD \sim [2\bar{3}11]$ (d) $g = 0002$, $BD \sim [1\bar{1}00]$ (e) $g = \bar{1}011$, $BD \sim [5\bar{7}23]$
(f) $g = \bar{1}\bar{1}22$, $BD \sim [1\bar{1}00]$

5.1.5. Conclusions

After testing using different reflections, it became obvious that the activated dislocations kept in good contrast during compression when the viewing g vector was perpendicular to the loading direction. In this way most bend contours were avoided.

In-situ TEM study shows that $\frac{1}{3}[11\bar{2}0](0002)$slip was the only slip system activated when the sample was compressed along $[12\bar{3}4]$. The plastic deformation was always initiated at the probe/pillar interface. The dislocations generated at this contact interface move relatively slowly as the plastic deformation continues. Several parallel basal planes from the contact surface were activated successively. These dislocation sources release arrays of dislocations before slip steps generate. Slip results in the formation of steps on the free surface of the pillar and slightly relieve the strain. An increase in the size of the slip steps can be linked to a stain burst and a load drop on the stress-strain curves.

During compression, the stress continues to increase and eventually reaches the critical values to activate new slip bands at other positions on the sample, first from the bottom corner of the pillar where the stress is highly concentrated, and then in the middle of the pillar. These dislocations move much more quickly than the ones from the contact surface.

5.2. Group 2 pillars with the loading direction along $[\bar{2}0\bar{8},12,7]$

For the purpose of investigating dislocation interactions, the second group of pillars was made from a compressed sample which contained pre-existing dislocations. The orientation was chosen to obtain multiple slip.

5.2.1. Preparation of the in-situ test pillars

The pillars in Group 2 were fabricated in the middle of the lower edge of the half TEM disc shown in Figure 5.14a. An EBSD map of the specimen is shown in Figure 5.14b. The selected α lath has an orientation of: horizontal direction X~$[\bar{2}\bar{1}36]$, vertical direction Y ~$[4\bar{2}\bar{2}1]$, normal direction Z~$[\bar{2}10\bar{8}3]$. The orientation is also indicated by the schematic cell: Figure 5.14a. The loading direction of the in-situ compression was approximately parallel to the Y axis.

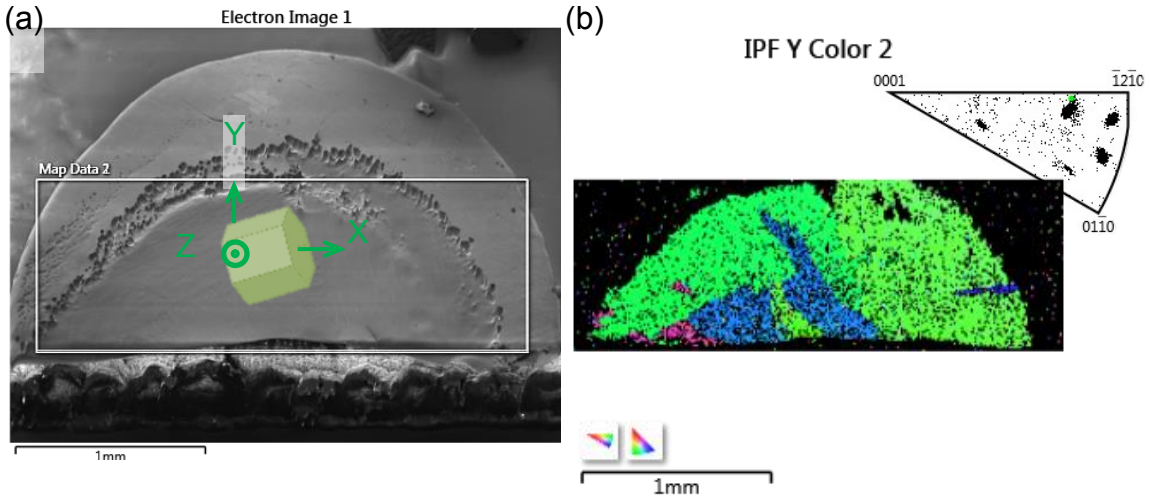

Figure 5.14 (a) SEM image of Sample 2 with a schematic cell illustrating the orientation of the selected area: horizontal direction X~$[\bar{2}\bar{1}36]$, vertical direction Y ~$[4\bar{2}\bar{2}1]$, normal direction Z~$[\bar{2}10\bar{8}3]$. (b) EBSD map of the specimen. Pillars were cut from the green lath between two blue ones.

Figure 5.15a is a TEM image of Pillar 4 in Group 2. The two accessible beam directions were $B_1 = [03\bar{3}1]$ and $B_2 = [1\bar{2}12]$ (Figure 5.15b and 5.15c). The contact surface between the probe and the pillar was $P_0 = B_1 \times B_2 = (\bar{5}233)$.The loading direction was $[\overline{20}8,12,7]$.

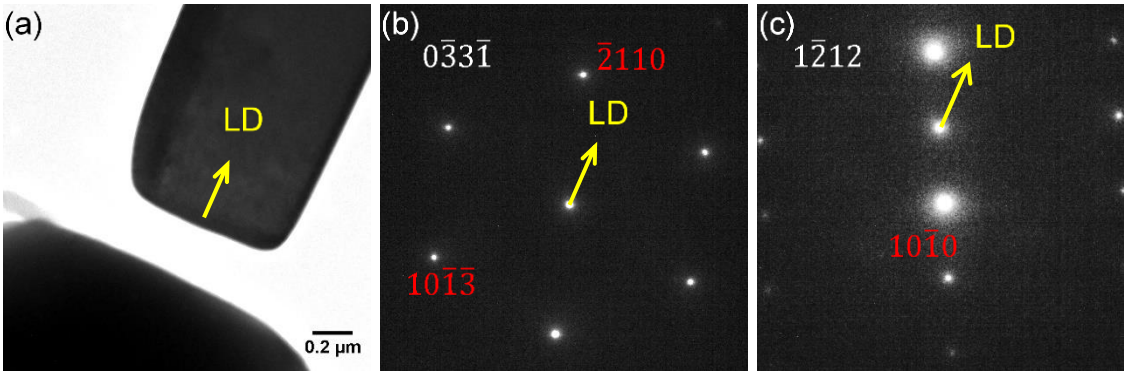

Figure 5.15 (a) Bright field image of Pillar 4 with loading direction ~$[\overline{20}8,12,7]$. (b) and (c) are diffraction patterns at the two accessible zone axes.

All the pillars in Group 2 have the same size: 0.4×1×2μm. Schmid factors for the possible slip systems (larger than 0.3) are listed in Table 5.4.

Table 5.4 Schmid factors (>0.3) of major slip systems in Group 2

Burgers vector	Slip plane	m	Burgers vector	Slip plane	m	Burgers vector	Slip plane	m
$\frac{1}{3}[\bar{1}\bar{1}20]$	$(\bar{1}100)$	0.42	$\frac{1}{3}[\bar{1}2\bar{1}0]$	$(\bar{1}011)$	0.34	$\frac{1}{3}[\bar{2}113]$	$(\bar{1}10\bar{1})$	0.39
$\frac{1}{3}[\bar{1}\bar{1}20]$	$(\bar{1}101)$	0.46	$\frac{1}{3}[\bar{2}110]$	(0001)	0.33	$\frac{1}{3}[\bar{2}113]$	$(\bar{1}01\bar{1})$	0.47
$\frac{1}{3}[\bar{1}2\bar{1}0]$	$(\bar{1}010)$	0.32	$\frac{1}{3}[\bar{1}\bar{1}23]$	$(\bar{1}01\bar{1})$	0.35	$\frac{1}{3}[\bar{2}113]$	$(\bar{2}11\bar{2})$	0.48

5.2.2. Dislocation motion

It was inferred in section 5.1 that a viewing g vector perpendicular to the loading direction is the best option for video recording, since it theoretically avoids the influence of bending to a large extent. However, the feasibility of this preferred viewing g vector quite depends on the practical situation. Sometimes, there is not an appropriate g vector perpendicular to the loading direction, limited by the tilting range of the single-tilt in-situ holder. Or, the viewing g vector satisfies the perpendicular condition, but is not suitable for observing dislocation motion when the observed dislocations are out of contrast with this reflection. The choice of viewing g vector is delicate.

Pillar 1 of Group 2 was deformed using displacement control mode with a maximum displacement of 50nm. The video was obtained using the $10\bar{1}3$ reflection. Video frames in Figure 5.16 are TEM images of Pillar 1 captured during compression in a time sequence of (a) 0, (b) 33, (c) 60, (d) 90, (e) 110 and (f) 157s. Figure 5.16a and 5.16f show dislocations in Pillar 1 before and after compression. Dislocations start to generate from 33s (Figure 5.16b) and stop propagation at 110s (Figure 5.16e). The newly generated dislocations are marked by arrow 1 in Figure 5.16b-f.

The disadvantage of reflection $10\bar{1}3$ is obvious, although it is the g vector nearly perpendicular to the loading direction. The contrast change of the pre-existing dislocation labelled 2 (Figure 5.16b to 5.16e) indicates that there were not perfect two-beam conditions during compression, which interfered with dislocation observations. Also, a_2 dislocations are out of contrast with the $10\bar{1}3$ reflection.

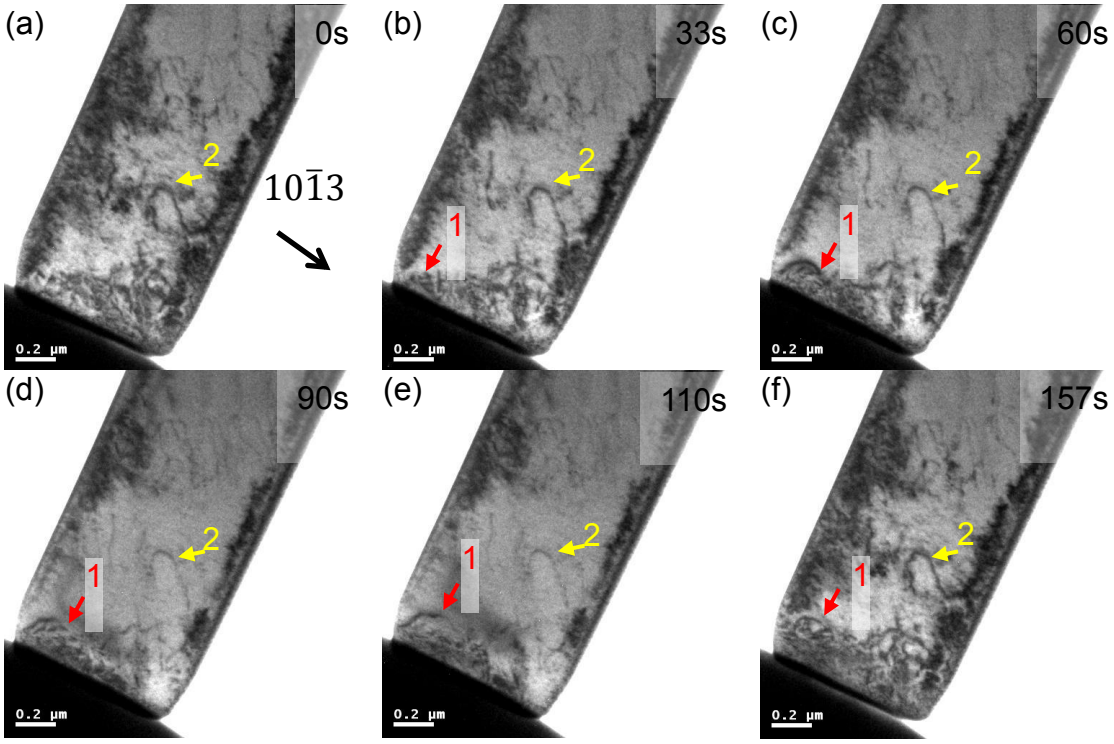

Figure 5.16 TEM images of Pillar 1 are video frames captured during compression in time sequences of (a) 0, (b) 33, (c) 60, (d) 90, (e) 110 and (f) 157s. $g = 10\bar{1}3,\ BD \sim [1\bar{5}41]$.

The activation sequence of a_3 prismatic and a_1 basal can be inferred from Pillar 4. (Detail analysis is in section 5.2.3) Pillar 4 in Group 2 was compressed twice using

the same loading force 300μN. The pillar size was approximately 0.4×1×2μm. The dislocation generation sequence in Pillar 4 can be seen in Figure 5.17. Three sequential TEM images were taken during the compression test. Figure 5.17a is the as-prepared sample before compression. The front part of the pillar is free of dislocations. Pre-existing dislocations lie away from the probe/pillar contact surface. Figure 5.17b and c show the activated slip systems after the first and second loading. As analysed in section 5.2.3, the dislocations in Figure 5.17b (labelled 1) with a Burgers vector of $\frac{1}{3}[\bar{1}\bar{1}20]$ were first activated on a prismatic plane. Then the second system $\frac{1}{3}[\bar{2}110]$ (labelled 2 in Figure 5.17c) on the basal plane was activated. The two types of dislocations were both generated from the probe/pillar contact surface.

The first compression of Pillar 4 mainly activated a_3 prismatic slip system. a_1 basal was activated afterwards. a_3 prismatic indeed generates first which can also be determined from the lightly deformed Pillar 1. However, there is not a distinct boundary when the a_1 basal start to glide. a_3 prismatic keeps expanding in parallel with the generation of a_1 basal. Figure 5.18 shows the remaining pillars of Group 2 before and after compression using a $10\bar{1}1$ reflection. a_1 basal and a_3 prismatic are labelled 1 and 2. Pillar 3 (Figure 5.18b and 5.18e) was compressed using a loading force of 300μN. Pillar 2 (Figure 5.18a and 5.18d) and Pillar 5 (Figure 5.18c and 5.18f) were deformed using displacement control mode with a maximum displacement of 100nm. A shear deformation of the front part of Pillar 2 occurs as shown in Figure 5.18d due to a_3 prismatic slip.

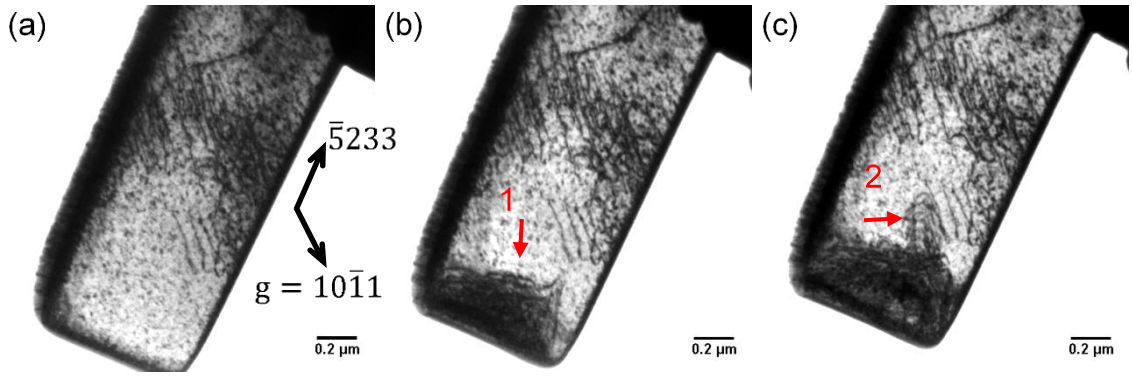

Figure 5.17 (a - c) Sequential TEM images of Pillar 4 taken during compression along the $[\bar{2}08,12,7]$ direction. $g = 10\bar{1}1,\ BD \sim [2\bar{7}53]$. (a) As-prepared sample before compression. The first group of dislocations generated on the prismatic plane is marked by the arrow in (b) and the second group on the basal plane is marked in (c).

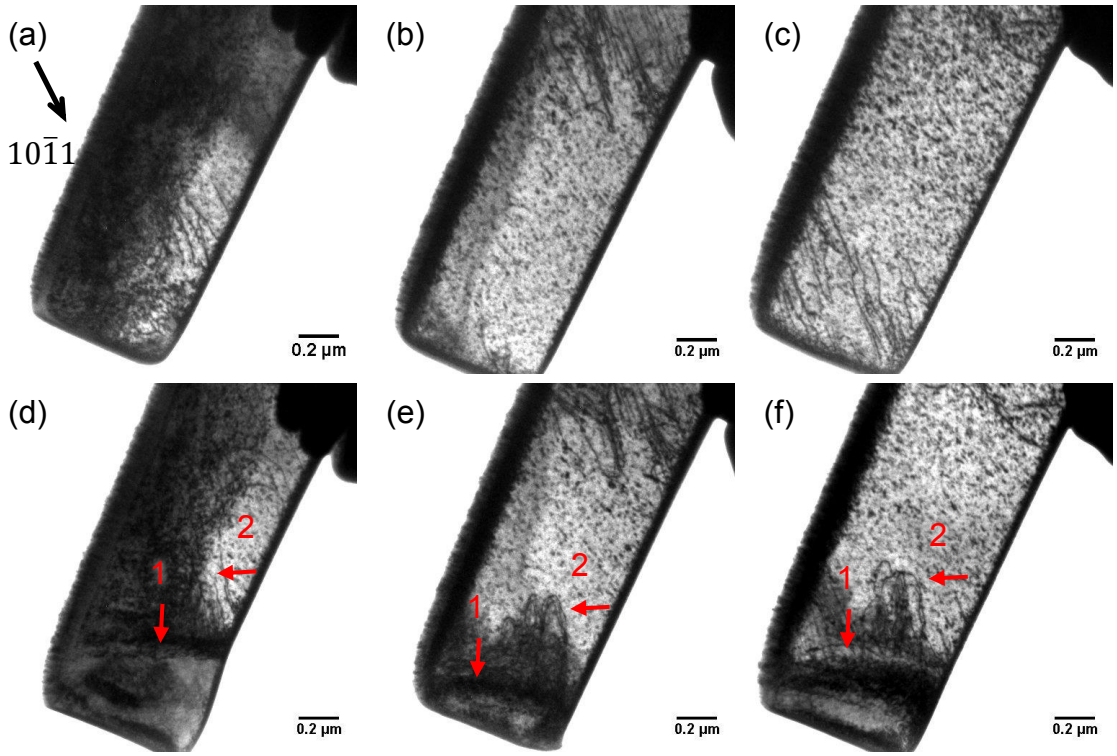

Figure 5.18 (a-c) show Pillar 2, Pillar 3 and Pillar 5 before compression. a_1 basal slip labelled 1 and a_3 prismatic slip labelled 2 generate after compression in (d) Pillar 2, (e) Pillar 3 and (f) Pillar 5. $g = 10\bar{1}1,\ BD \sim [2\bar{7}53]$.

Neither any obvious interaction of newly generated dislocations with pre-existing dislocations nor reactivation of the pre-existing dislocations ($\frac{1}{3}[1\bar{2}10](0001)$, $\frac{1}{3}[11\bar{2}0](1\bar{1}01)$) and $\frac{1}{3}[11\bar{2}0](1\bar{1}00)$) was observed. The loading direction $[\overline{20}8,12,7]$ is against the reactivation of $\frac{1}{3}[1\bar{2}10](0001)$ and $\frac{1}{3}[11\bar{2}0](1\bar{1}01)$ according to Table 5.4. The pre-existing $\frac{1}{3}[11\bar{2}0](1\bar{1}00)$ were not reactivated either because of pinning or the stress gradient. Although the pillar was deformed, the stress where the pre-existing $\frac{1}{3}[11\bar{2}0](1\bar{1}00)$ were located did not apparently achieve the critical value to reactivate a_3 prismatic slip.

5.2.3. Dislocation analysis

Since the pillars in Group 2 were made from a compressed sample investigated in section 4.3, the pre-existing dislocations in the pillars were introduced by the macro-compression of the bulk specimen. According to the Kikuchi maps of the pillars, all the pillars in Group 2 have almost the same orientation. Take Pillar 4 as an example to analyse the dislocations. The pre-existing dislocations in Pillar 4 before in-situ compression are shown in Figure 5.19 using different reflections. Since pillars were installed on the single-tilt compression holder, the g vectors available for analysis were limited.

The dislocations which are invisible in Figure 5.19a and 5.19b but visible in Figure 5.19c and 5.19d have a Burgers vector of $\frac{1}{3}[1\bar{2}10]$. These a_2 dislocations are represented by the red dashed lines in Figure 5.19c and 5.19d and lie on the basal plane. The dislocations visible in Figure 5.19b and 5.19d (labelled by yellow dashed lines) are out of contrast when $g = 0002$ (Figure 5.19a) and $g = \bar{1}102$ (Figure 5.19c). These screw dislocations have a Burgers vector of $\frac{1}{3}[11\bar{2}0]$. Their slip plane is $(1\bar{1}01)$.

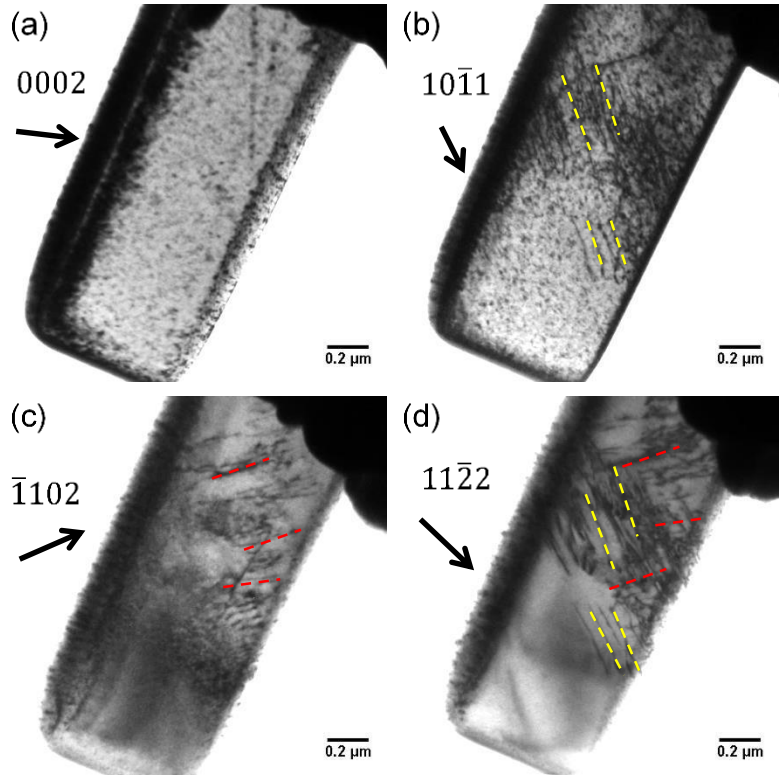

Figure 5.19 Pre-existing dislocations represented by red and yellow dashed lines in Pillar 4 before compression are a_2 (red) and a_3 (yellow). (a) $g = 0002$, BD $\sim [0\bar{1}10]$ (b) $g = 10\bar{1}1$, BD $\sim [2\bar{7}53]$ (c) $g = \bar{1}102$, BD $\sim [5\bar{1}\bar{3}89]$ (d) $g = 11\bar{2}2$, BD $\sim [2\bar{4}23]$

Similarly, Pillar 1 of Group 2 before in-situ compression is shown in Figure 5.21. The red dashed lines represent a_2 dislocations on the basal plane. The yellow dashed and solid lines represent a_3 screw dislocations on the $(1\bar{1}01)$ and $(1\bar{1}00)$ planes.

Figure 5.20 shows Pillar 4 in Group 2 with different reflections operating after in-situ compression. Two types of slip system were activated during in-situ compression. One is on the basal plane (0001) marked 2 in Figure 5.20a, which is similar to the activated slip in Pillar 1 Group 1. Since these dislocations are out of contrast when $\mathrm{g} = 0002$ (Figure 5.20a) and in contrast when $\mathrm{g} = 10\bar{1}1$ (Figure 5.20b) and $\mathrm{g} = \bar{1}101$ (Figure 5.20c), they are a_1 dislocations.

Dislocations labelled 1 are visible when $\mathrm{g} = 10\bar{1}1$ (Figure 5.20b), and invisible when $\mathrm{g} = 0002$ (Figure 5.20a) and $\mathrm{g} = \bar{1}101$ (Figure 5.20c). Thus, they are a_3 dislocations. In Figure 5.20d, the a_3 dislocation labelled 1 is formed from two segments marked by yellow dashed lines. The long segment lies on the $(\bar{1}010)$ plane (Figure 5.20d) and the $(\bar{2}110)$ plane (Figure 5.20a) and has a line direction of $[0001]$. Thus, a_3 dislocations glide on the $(1\bar{1}00)$ plane. The short segment of a_3 is screw, which lies on the $(\bar{1}102)$ plane (Figure 5.20d) and the basal plane (Figure 5.20a).

Several pyramidal slip systems having large Schmid factors (nearly 0.5) in Table 5.4 were not activated due to the large CRSS. Slip system $\frac{1}{3}[\bar{1}\bar{1}20](1\bar{1}00)$ with a relatively large Schmid factor, although not the largest, was activated first.

$\frac{1}{3}[\bar{2}110](0001)$ nearly has the smallest Schmid factor in Table 5.4. The activation of $\frac{1}{3}[\bar{2}110](0001)$ indicates that <a> basal slip is more easily activated than other non-basal slip systems with similar or even larger Schmid factors.

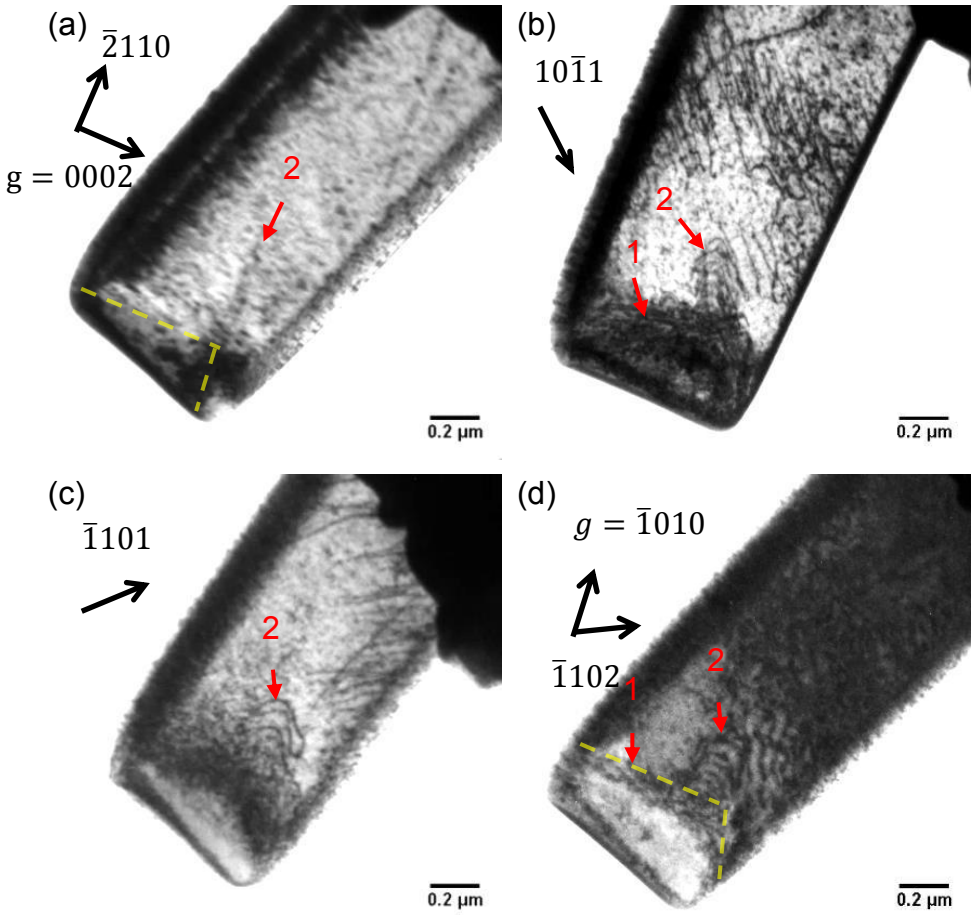

Figure 5.20 Multiple slip activated in Pillar 4 of Group 2 with different reflections . (a) $g = 0002$, $BD \sim [0\bar{1}10]$ (b) $g = 10\bar{1}1$, $BD \sim [2\bar{7}53]$ (c) $g = \bar{1}101$, $BD \sim [0\bar{1}11]$ (d) $g = \bar{1}010$, $BD \sim [2\bar{4}23]$. a_1 basal slip labelled 1, a_3 prismatic slip labelled 2.

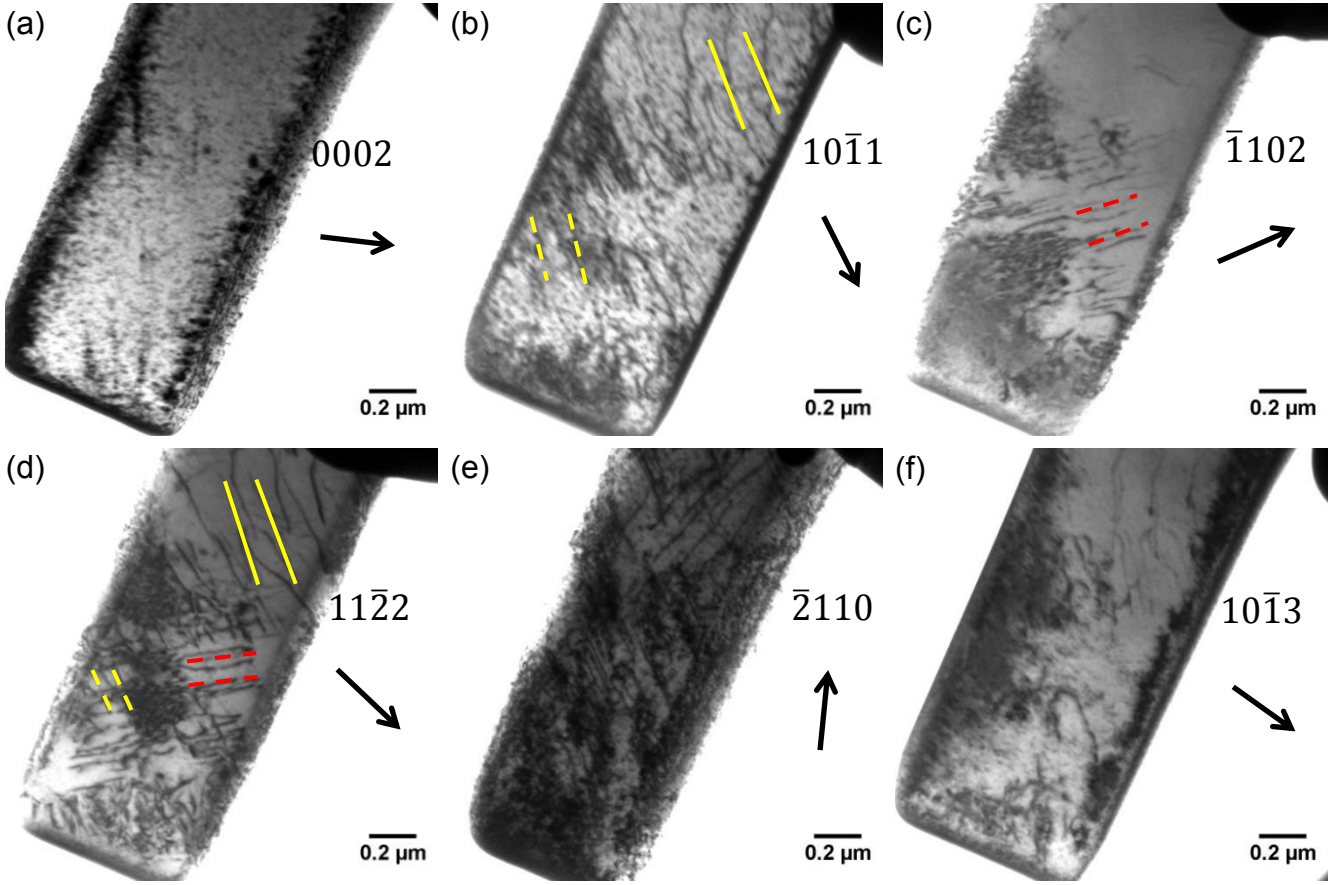

Figure 5.21 Pre-existing dislocations represented by red and yellow dashed lines in Pillar 1 Group 2 before compression are a_2 (red) and a_3 (yellow). (a) $\mathrm{g} = 0002,\ \mathrm{BD} \sim [0\bar{1}10]$ (b) $\mathrm{g} = 10\bar{1}1,\ \mathrm{BD} \sim [2\bar{7}53]$ (c) $\mathrm{g} = \bar{1}102,\ \mathrm{BD} \sim [5\bar{1}\bar{3}89]$ (d) $\mathrm{g} = 11\bar{2}2,\ \mathrm{BD} \sim [2\bar{4}23]$ (e) $\mathrm{g} = \bar{2}110,\ \mathrm{BD} \sim [0\bar{3}3\bar{1}]$ (f) $\mathrm{g} = 10\bar{1}3,\ \mathrm{BD} \sim [1\bar{5}41]$

5.2.4. Conclusions

The theoretically ideal viewing g vector perpendicular to the loading direction does not suit every case. The feasibility depends on practicalities. Limited by the tilting range of the single-tilt in-situ holder, a perpendicular g vector may not exist. Or, the observed dislocations may be out of contrast with this reflection.

Two slip systems were activated under $[\overline{20}8,12,7]$ loading: firstly $\frac{1}{3}[\bar{1}\bar{1}20](1\bar{1}00)$ and secondly $\frac{1}{3}[\bar{2}110](000\bar{1})$. <a> basal slip is more easily activated than other slip systems with similar or even larger Schmid factors.

No obvious interaction of newly generated dislocations and pre-existing dislocations was observed. The pre-existing dislocations were barely activated again.

5.3. Group 3 pillars with the loading direction along $[0002]$

In-situ compression tests were performed along $[0002]$ in the third group of pillars, in order to activate <c+a> dislocations.

5.3.1. Preparation of the in-situ test pillars

The pillars in Group 3 were fabricated at the edge of the red grain in the TEM disc shown in Figure 5.22. The EBSD map of the specimen is shown in Figure 5.22b. The inset schematic cell illustrates the orientation of the selected red α laths: horizontal direction X~$[\bar{1}100]$, vertical direction Y~$[0002]$, normal direction Z ~$[11\bar{2}0]$. The loading direction of the in-situ compression was approximately $[0002]$.

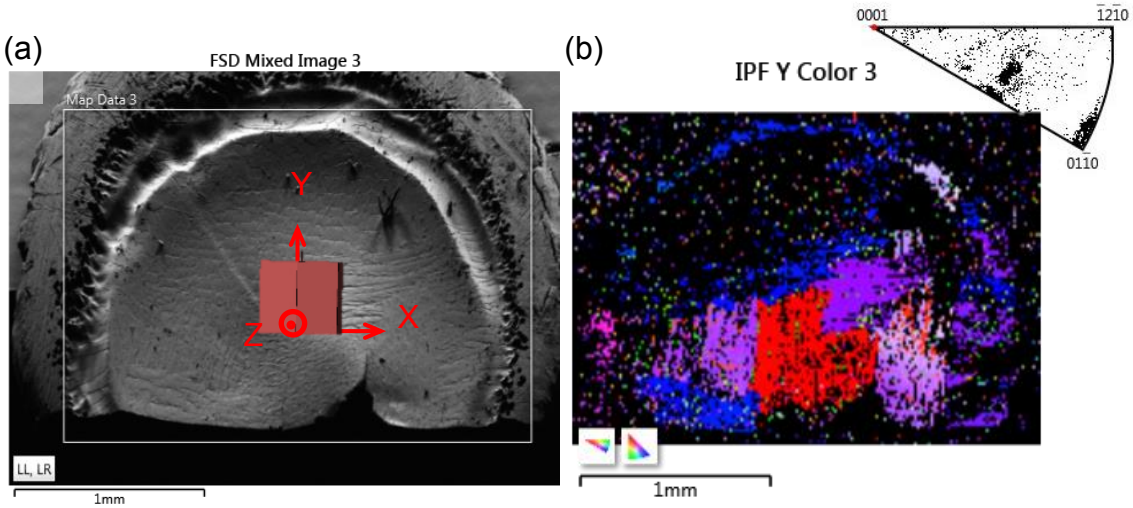

Figure 5.22 (a) SEM image of the sample for c compression tests (b) EBSD map of the pecimen. Pillars of Group 3 were cut from the red α laths: X~$[\bar{1}100]$, Y~$[0002]$, Z~$[11\bar{2}0]$.

Theoretically, when the loading direction is exactly $[0002]$, all Schmid factors for <a> slip are 0. Only <c+a> dislocations can be activated. Schmid factors for slip systems are listed in Table 5.5.

Table 5.5 Schmid factors of slip systems in Group 3

Burgers vector	Slip plane	m	Burgers vector	Slip plane	m	Burgers vector	Slip plane	m
$\frac{1}{3}\langle 1\bar{2}10\rangle$	(0001)	0	$\frac{1}{3}\langle 1\bar{2}10\rangle$	$\{10\bar{1}0\}$	0	$\frac{1}{3}\langle 1\bar{2}10\rangle$	$\{10\bar{1}1\}$	0
$\frac{1}{3}\langle 11\bar{2}3\rangle$	$\{\bar{1}011\}$	0.4	$\frac{1}{3}\langle 11\bar{2}3\rangle$	$\{\bar{1}\bar{1}22\}$	0.45			

There are some challenges for compression under c loading: first, theoretically multiple <c+a> slip would be activated under c loading due to the symmetry of the hcp crystal. The dislocation analysis would then be complicated. Secondly, the PI95 in-situ test holder is a single tilt holder, which means the available imaging conditions are only two-beam condition ($\mathrm{g} = 0002$) or zone axes which contain $\mathrm{g} = 0002$ when the loading direction is $[0002]$. However, $\mathrm{g} = 0002$ is not an ideal two-beam condition, since only <c+a> dislocations are in contrast in this case. Also, any buckling of the pillar, which happens a lot in in-situ compression tests, will drive the sample away from the two beam condition ($\mathrm{g} = 0002$) which hampers dislocation observation.

Thus, the loading direction needs to be close to $[0002]$ but not exactly. The conditions for imaging dislocations were chosen as $\mathrm{B} \approx [1\bar{1}00]$, $\mathrm{g} = 11\bar{2}0$. The pillar size was approximately 0.4 x 0.8 x 1 μm.

5.3.2. Dislocation motion

Pillar 3 in Group 3 was deformed under load control with a peak force of 750 μN. The operation of <c+a> slip in Pillar 3 was recorded using a $\bar{1}\bar{1}20$ reflection. The frames extracted from the video are shown in Figure 5.23 in chronological order. The arrows in each frame show the position of newly generated dislocations.

Figure 5.23a shows the beginning of compression when the probe just contacts the pillar. Set the start time as 0. During the elastic deformation, the contrast of the pillar barely changed as shown in Figure 5.23b. In Figure 5.23c, the first few dislocations bow out from the probe/pillar interface at the same time. They expand and generate in the area between the probe/pillar contact surface and the first LAGB in Figure 5.23d and 5.23e. The first dislocation passes through the LAGB at 95.92s in Figure 5.23f. The dislocation beyond the LAGB extends horizontally parallel to the basal LAGB in Figure 5.23g and 5.23h. The dislocations under the LAGB also propagate during this period. More dislocations generate beyond the LAGB from 135.83s in Figure 5.23i. Figure 5.23k shows the final dislocation configuration at maximum deformation. Figure 5.23l is Pillar 3 after compression.

The pre-existing <c+a> LAGB on the basal plane represented a certain hindrance to the newly generated dislocations. The newly generated dislocations piled up at the boundary and then burst through it when the dislocations accumulated to some degree as shown in Figure 5.23f. However, the Burgers vector of the new dislocations remains the same. It is hard to distinguish the opposite reaction of the new dislocations on the LAGB. The LAGB seems to remain on its basal plane during compression (Figure 5.23g).

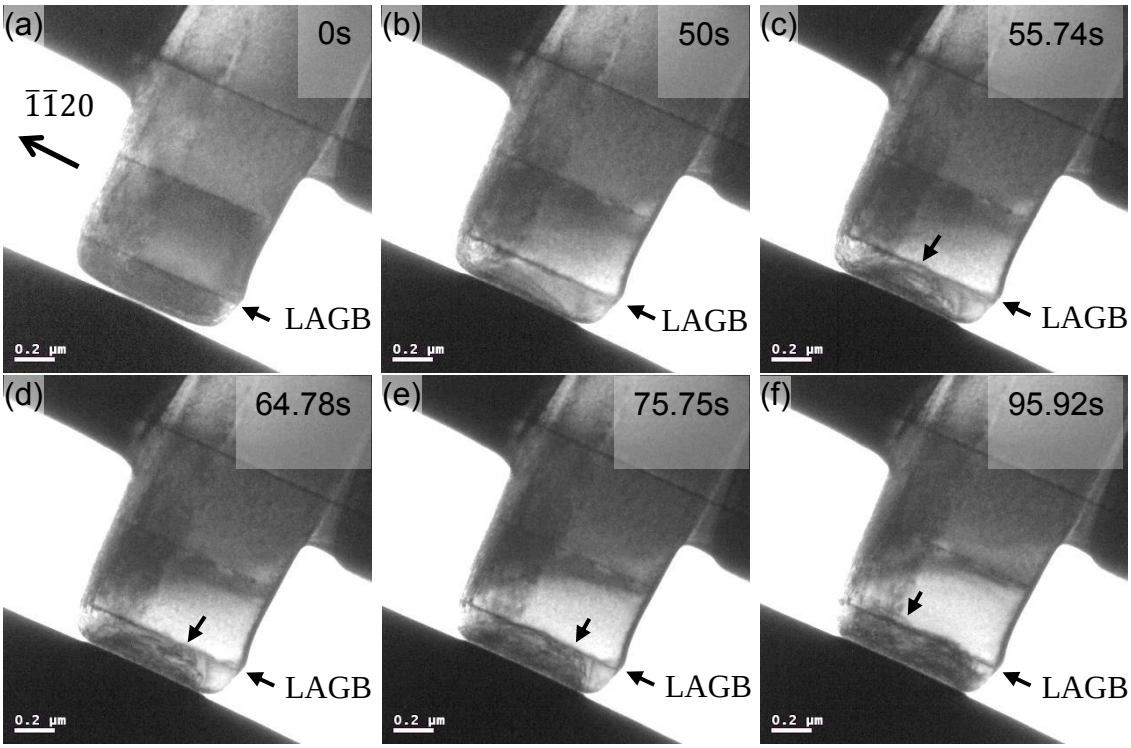

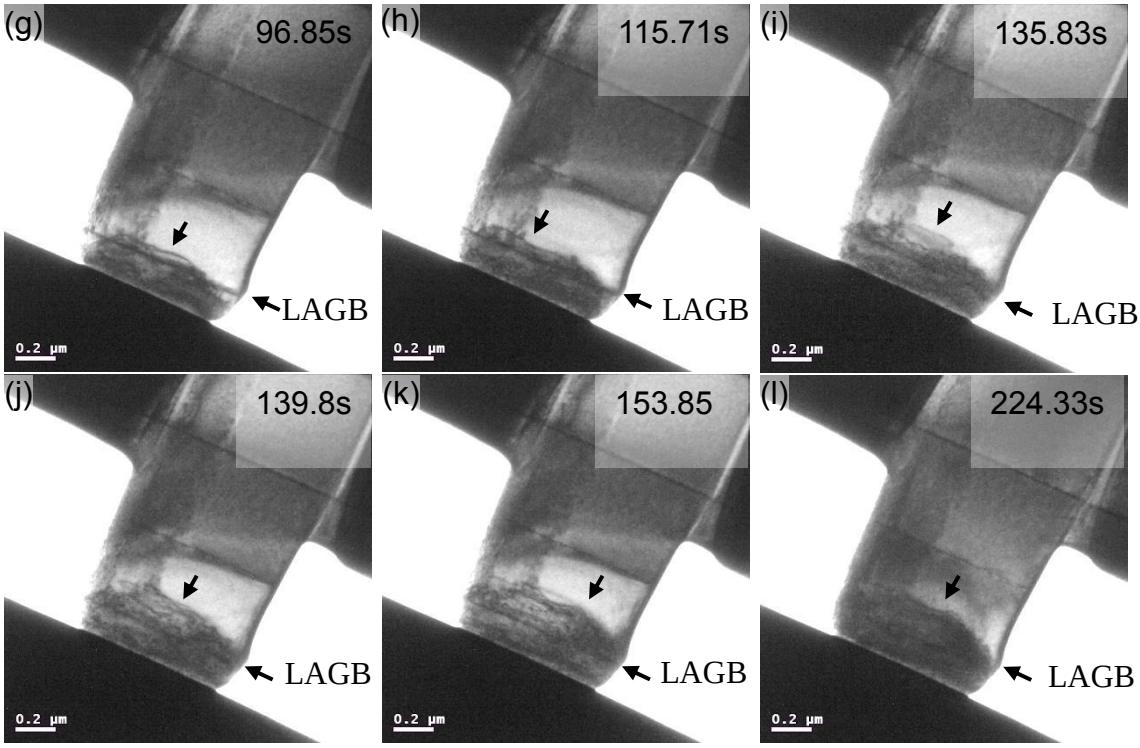

Figure 5.23 (a-l) TEM images of Pillar 3 in Group 3 are video frames captured during compression in time sequence. $\mathrm{g} = \bar{1}\bar{1}20$, $\mathrm{BD} \sim [1\bar{1}00]$. (a and l) show the pillar before and after compression. (b) shows the start of plastic deformation. (c) The first few dislocations emit from the contact surface. (d and e) Dislocations propagate and expand in the area between the contact surface and the LAGB. (f) The first dislocation passes through the LAGB and expands in (g and h). (i) More dislocations generate beyond the LAGB and expand in (j) and (k). (k) shows the pillar at maximum deformation.

The pre-existing non-basal <c+a> dislocations were slightly activated under c loading as observed in other pillars of Group 3. Figure 5.24 shows pre-existing non-basal <c+a> dislocations in Pillars 2 and 4 before compression. The loading direction for Pillar 4 was deviated from the c axis by a few degrees. The 0002 reflection was not available for Pillar 4 due to the limitation of by single-tilt. However, the adjacent Pillar 2 in the same group had the appropriate orientation. The curved dislocations in Figure 5.24a are <c+a> dislocations in the 0002 reflection. Similarly, the curved dislocations in Pillar 4 represented by the dashed lines in Figure 5.24b-d are <c+a>. They are invisible when $\mathrm{g} = 01\bar{1}\bar{1}$ (Figure 5.24c). The Burgers vector is $\pm 1/3\,[\bar{1}2\bar{1}3]$.

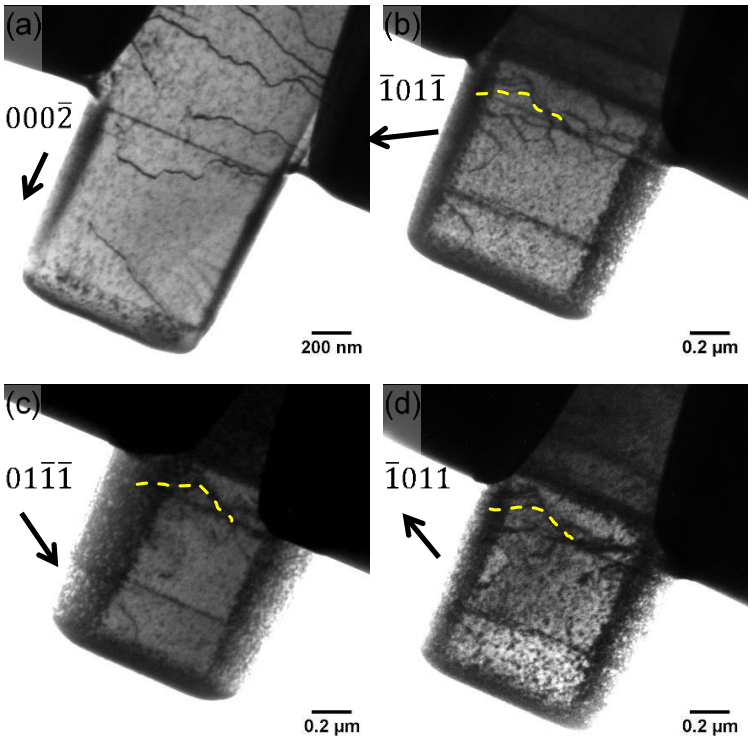

Figure 5.24 (a) Pre-existing non-basal <c+a> dislocations in Pillar 2 of Group 3 before compression. $\mathrm{g} = 000\bar{2},\ \mathrm{BD} \sim [1\bar{1}00]$. (b-d) Pre-existing non-basal <c+a> dislocations in Pillar 4 before compression. (b) $\mathrm{g} = \bar{1}01\bar{1}, \mathrm{BD} \sim [1\bar{2}10]$ (c) $\mathrm{g} = 01\bar{1}\bar{1},\ \mathrm{BD} \sim [1\bar{1}00]$ (d) $\mathrm{g} = \bar{1}011, \mathrm{BD} \sim [1\bar{2}10]$

The motion of pre-existing dislocations in Pillar 4 is shown in Figure 5.25. Pillar 4 in Group 3 was deformed under displacement control with a maximum displacement of 80 nm, using the $\bar{1}\bar{1}20$ reflection. The frames extracted from the video are shown in Figure 5.25 in chronological order. The arrows 1, 2 and 3 show the positions of the activated pre-existing dislocations. Figure 5.25a shows Pillar 4 before compression. Newly generated dislocations start to bow out from the probe/pillar contact surface at 52s (Figure 5.25b). The pre-existing dislocation labelled 1 starts to move at 67s (Figure 5.25c). The short curved segment in the dislocation labelled 1 gradually becomes straight parallel to the basal plane with the right end pinned in the following 4 frames. The dislocation labelled 2 starts to move in Figure 5.25d and continues to bow out in Figure 5.25h and 5.25j. Figure 5.25g, i and k illustrate the motion of dislocation labelled 3. The right end of the dislocation gradually curls up to the left. Figure 5.25l shows Pillar 4 after compression.

Although these pre-existing dislocations moved slightly under c loading, most dislocation segments were strongly pinned. The pre-existing dislocations did not performed as dislocation sources during deformation.

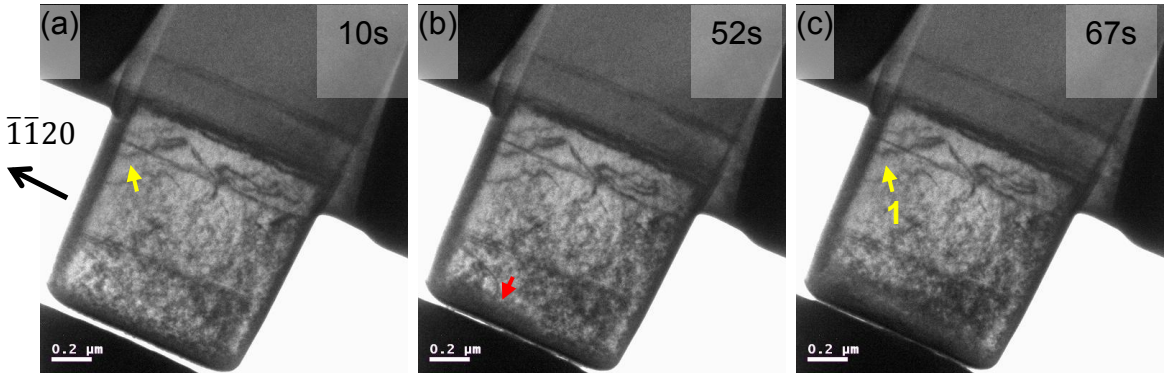

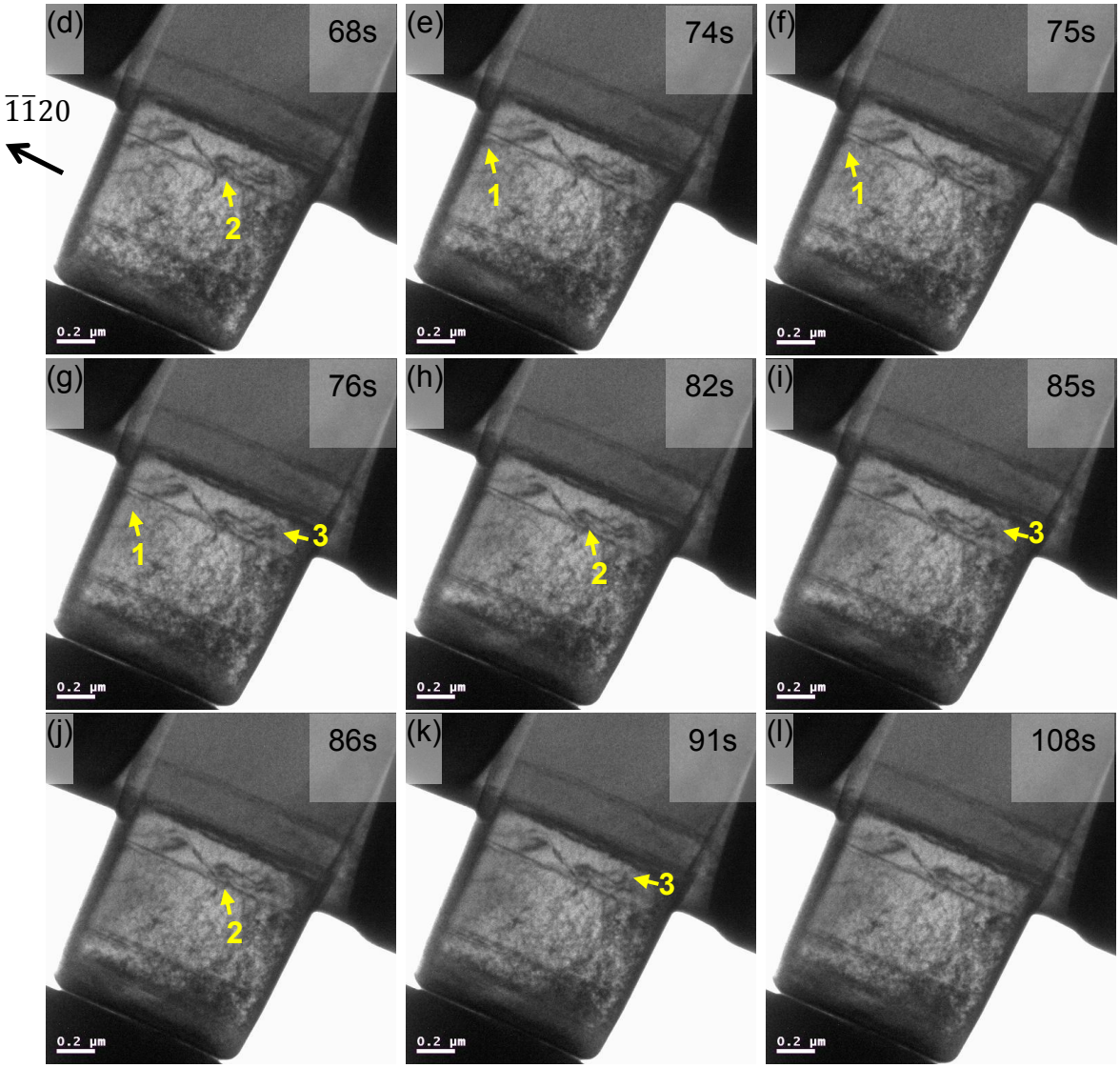

Figure 5.25 (a-l) TEM images of Pillar 4 in Group 3 are video frames captured during compression. $g = \bar{1}\bar{1}20$, $BD \sim [1\bar{1}00]$. (a and l) show Pillar 4 before and after compression. (b) New dislocations start to generate. (c) The curved segment in the pre-existing dislocation labelled 1 starts to move and gradually becomes parallel to the LAGB in (e, f and g). (d) The dislocation labelled 2 starts to move and keeps bowing out in (h) and (j). (g), (i), (k) The right end of the dislocation labelled 3 gradually curls up to the left.

5.3.3. Dislocation analysis

Pillar 1 in Group 3 was dislocation-free before compression as shown in Figure 5.26a. Figure 5.26b-f indicate that <c+a> dislocations were activated in Pillar 1 after the compression test. A dense array of dislocations (labelled by arrows) generated from the probe/pillar contact surface and propagated into the sample shallowly. According to the invisibility criterion, new dislocations invisible with $01\bar{1}1$ (Figure 5.26e) and $\bar{1}010$ (Figure 5.26f) reflection have a Burgers vector of $\frac{1}{3}[1\bar{2}13]$.

Pillar 3 in Group 3 contained pre-existing dislocations before compression as shown in Figure 5.27a. The pre-existing dislocations labelled by yellow arrows on the basal plane formed <c+a> LAGBs just like those (Figure 4.7b) in the annealed sample. The new dislocations (labelled by red arrows) generated from the probe/pillar interface and propagated deep into the sample. Similar as above, the new dislocations have a Burgers vector of $\frac{1}{3}[1\bar{2}13]$.

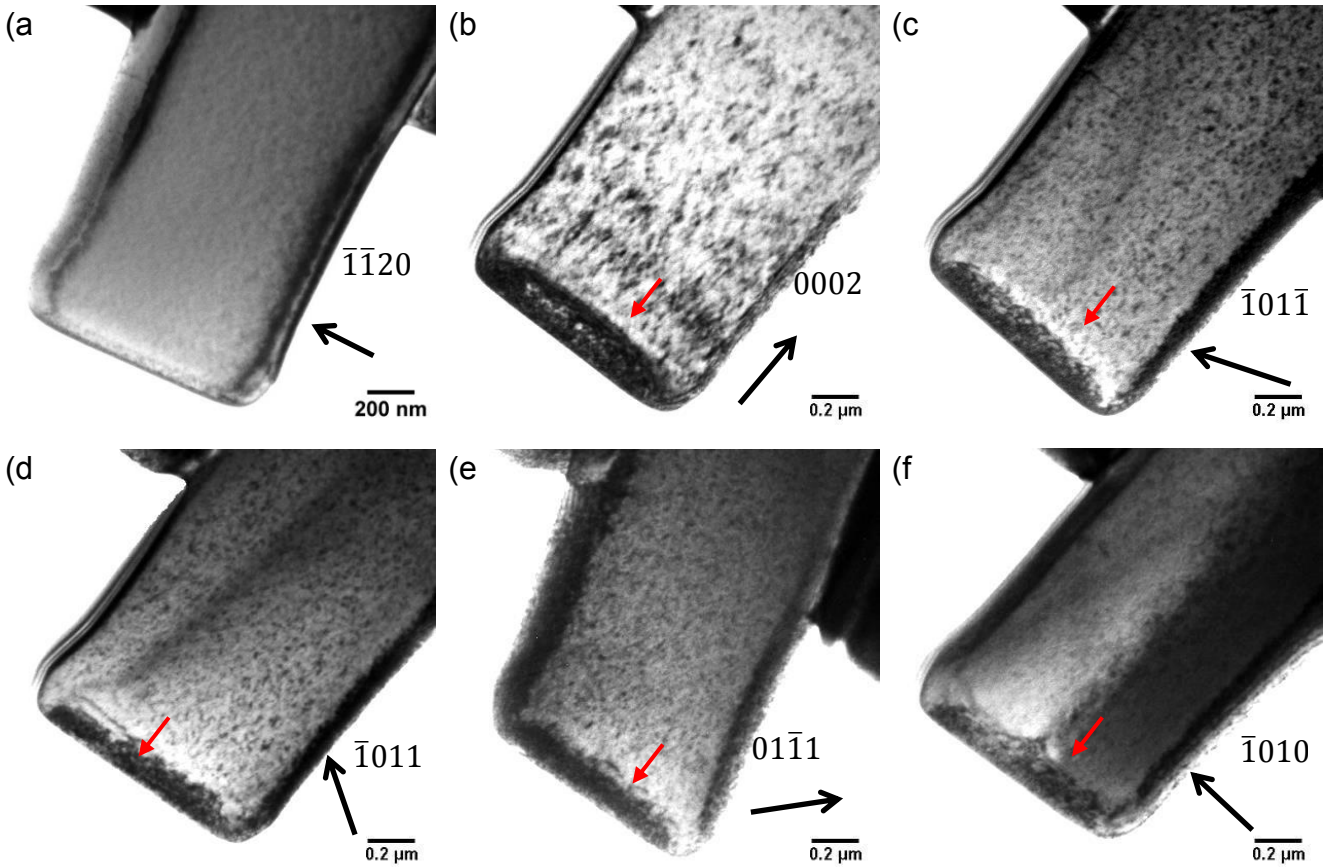

Figure 5.26 (a) Pillar 1 in Group 3 before in-situ compression (b)-(f) Bright field images of Pillar 1 after compression using different g vectors.

(a) $g = \bar{1}\bar{1}20$, BD ~ $[1\bar{1}00]$ (b) $g = 0002$, BD ~ $[1\bar{2}10]$ (c) $g = \bar{1}01\bar{1}$, BD ~ $[7\bar{1}\bar{1}4\bar{3}]$

(d) $g = \bar{1}011$, BD ~ $[5\bar{7}23]$ (e) $g = 01\bar{1}1$, BD ~ $[5\bar{4}\bar{1}3]$ (f) $g = \bar{1}010$, BD ~ $[1\bar{2}11]$

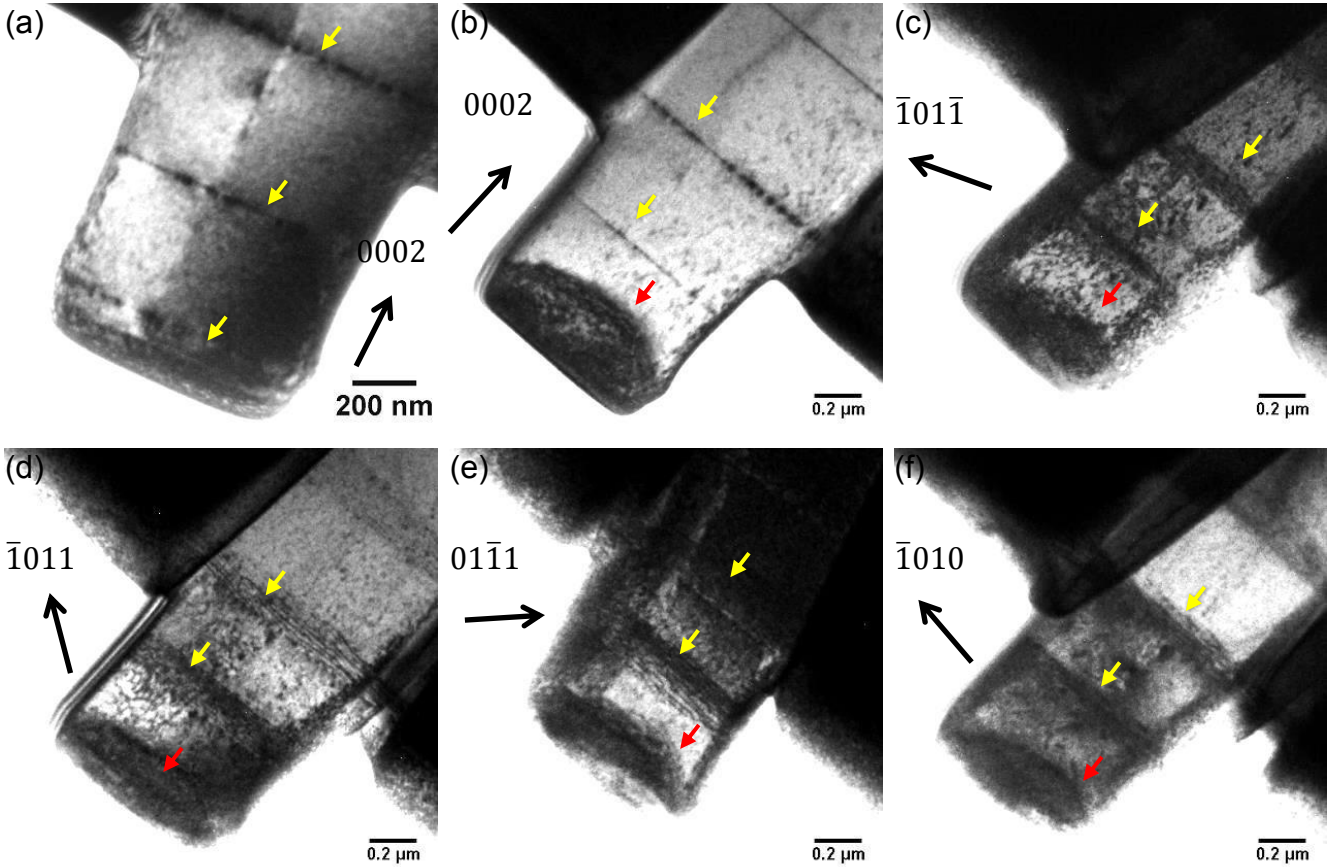

Figure 5.27 (a) Pillar 3 with pre-existing dislocations before in-situ compression (b)-(f) Bright field images of Pillar 3 after compression.

(a) $g = 0002$, $BD \sim [4\bar{5}10]$ (b) $g = 0002$, $BD \sim [1\bar{1}00]$ (c) $g = \bar{1}01\bar{1}$, $BD \sim [4\bar{1}\bar{1}73]$

(d) $g = \bar{1}011$, $BD \sim [4\bar{5}13]$ (e) $g = 01\bar{1}1$, $BD \sim [5\bar{4}\bar{1}3]$ (f) $g = \bar{1}010$, $BD \sim [1\bar{2}11]$

Under $[0002]$ loading, the Schmid factor of the $\langle\bar{2}113\rangle\{2\bar{1}\bar{1}2\}$ slip systems is 0.45 and 0.404 for $\langle\bar{2}113\rangle\{1\bar{1}01\}$. The determination of the slip plane is as follows.

Figure 5.28 shows bright field images of Pillar 3 after compression using different beam directions. In the experiment, the slip plane of the generated <c+a> dislocations in Pillar 3 always had a relatively large projection area, while the beam direction rotated around the c axis from $[2\bar{1}\bar{1}0]$ (Figure 5.28a) to $\left[1\bar{5}40\right]$ (Figure 5.28f).

Among the possible slip systems indicated in Figure 5.29, $\frac{1}{3}[1\bar{2}13](\bar{1}101)$ is the most eligible one. It is symmetrical around $[1\bar{1}00]$ and agrees with the Burgers vector analysis result. For the $(\bar{1}2\bar{1}2)$ plane, the projection would become narrow and tend to be end-up when the beam direction moves towards $[2\bar{1}\bar{1}0]$.

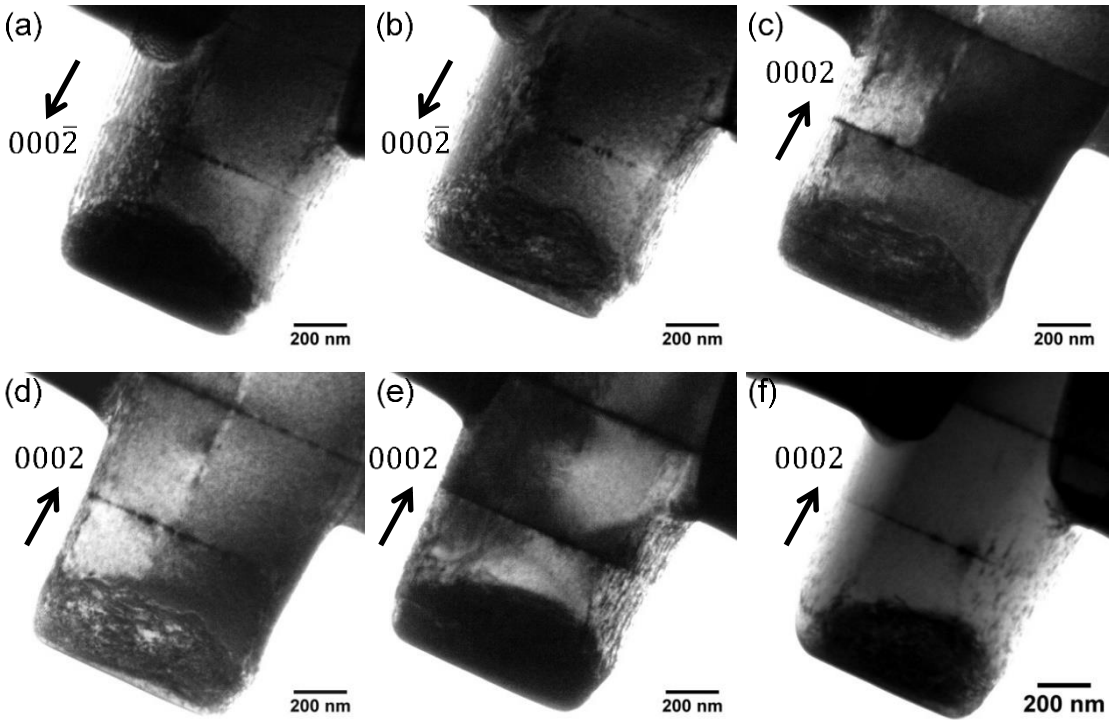

Figure 5.28 Bright field images of Pillar 3 after compression using different beam directions. $g = 0002$ or $g = 000\bar{2}$ (a) $B \sim [2\bar{1}\bar{1}0]$ (b) $B \sim [3\bar{2}\bar{1}0]$ (c) $B \sim [1\bar{1}00]$ (d) $B \sim [4\bar{5}10]$ (e) $B \sim [1\bar{2}10]$ (f) $B \sim [1\bar{5}40]$.

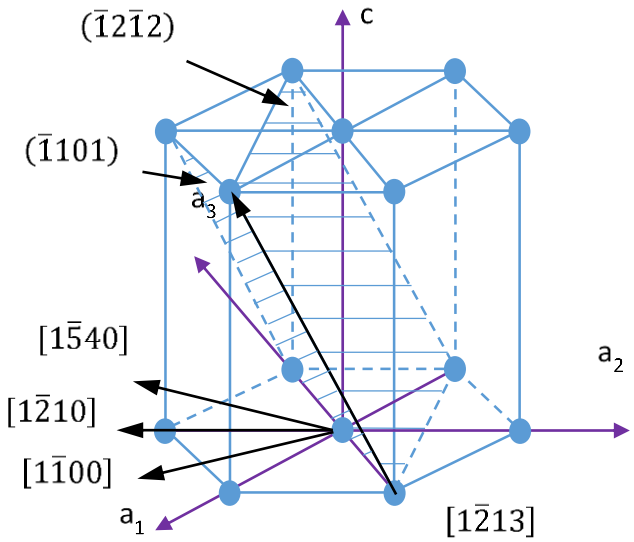

Figure 5.29 Schematic diagram of the possible slip systems in Pillar 3

5.3.4. Conclusions

The $[0002]$ direction is stiff. The pillars in Group 3 were prepared relatively short to minimize instability. $\mathrm{B} \approx [1\bar{1}00]$, $\mathrm{g} = 11\bar{2}0$ was the beam condition used for imaging pillars in Group 3.

In pillars of Group 3, the $\frac{1}{3}[1\bar{2}13](\bar{1}101)$ slip system was activated under c loading.

The pre-existing <c+a> LAGBs on the basal plane prevented the motion of new generated dislocations to some extent. The newly generated dislocations piled up at the LAGB and went through the boundary when enough dislocations were accumulated. The Burgers vector of the new dislocations did not change when passing the LAGB. The LAGB remained on the basal plane during compression.

The pre-existing non-basal <c+a> dislocations were slightly activated during compression, although most of the dislocations were pinned. They did not function as dislocation sources during deformation.

Chapter 6. Discussion

6.1. Macro-compression vs in-situ testing

The behaviour of dislocations in the in-situ test can be used to explain the dislocation configurations in the bulk compressed samples.

6.1.1. Heterogeneous deformation

Planar slip is a typical slip feature in the bulk compressed specimen. The formation mechanism has been discussed in section 4.3.5.1. The deformation of Pillar 6 in Group 1 demonstrated planar slip in which the newly generated dislocations slipped along separate individual slip planes. Similar observations have been reported in in-situ compression of Al [123]. In other reports [124-126], homogenous deformation is more commonly observed during in-situ compression. Ye [123] attributed the uniform deformation to the high strain rate and the presence of strong obstacles.

Planar slip is associated with the loading direction. Pillars in Group 1 show planar slip on basal planes, while c loading in Group 3 did not cause planar slip. Yu et al. [101] also deformed a Ti64 pillar under c loading, which resulted in uniform deformation. Compared to <a> basal slip, <c+a> dislocations in pyramidal planes have stronger interaction with each other. The strong entanglement of dislocations led to uniform deformation. In the same pillar, the probe/pillar contact surface restricted the front part of the pillar, which made the deformation of the top of Pillar 6 Group 1 more homogeneous than in other positions in the pillar. Multiple slip activated in Group 2 led to stronger obstacles which also contribute to the uniform deformation.

In the bulk compressed sample, planar slip was observed in prismatic and pyramidal planes. <c+a> dislocations were not observed forming planar slip. In the in-situ compressed pillars, planar slip was activated on basal planes. Different from bulk samples, the surface condition of the pillars needs to be considered. Beam damage on the pillar surfaces induced by FIB preparation can influence the mechanical response of the pillars [103]. Surface effects and strain localisation may affect the generation of dislocations in pillars.

6.1.2. Dislocation mobility

In the bulk compressed sample, the grown-in <c+a> LAGBs show no sign of being moved. The stability of <c+a> LAGBs during in-situ testing of Pillar 3 of Group 3 is also confirmed. Although the change of Burger vector was unclear, dislocations in the <c+a> LAGBs of Pillar 3 remained in their basal planes during deformation. The pre-existing non-basal <c+a> dislocations in the in-situ sample (Pillar 4 Group 3) were observed to be slightly activated. However, they did not act as dislocation sources due to the strong pinning. The probability of operation of the pre-existing <c+a> segments as dislocation sources is determined by competition between the depinning force and the CRSS.

The grown-in <a> dislocations can hardly be distinguished from the activated <a> slip in the bulk compressed sample. The interaction between them is unknown. In the micro-pillars, the pre-existing <a> dislocations observed were neither reactivated nor did they show any interaction with newly generated dislocations. The possible reasons are: the loading direction is not appropriate to activate pre-existing slip systems; the localized stress is not enough for depinning.

The repeated cross-slip of <a> dislocations between prismatic and first order pyramidal planes is another slip feature in the bulk compressed sample. However, in micro-pillars, cross-slip is not obvious.

6.1.3. Interaction of glissile dislocations and LAGB

The inference that <c+a> LAGBs would slightly intercept the glissile dislocations has been demonstrated in the compression deformation of Pillar 3 Group 3. The <c+a> LAGB hindered the dislocation motion for a while, until pile-ups overcame the boundary without changing its Burgers vectors.

Dislocation dissociation has not been displayed during in-situ compression. The mechanism needs to be further studied.

6.2. Dislocation characters in the micro-test sample

6.2.1. Dislocation nucleation and generation

All the deformations of the micro-pillars in this project started from the probe/pillar interface. The first dislocation always nucleated from the contact surface. Dislocation sources at other positions of the pillar were less favourable until the front part fully deformed and the source near the contact surface became exhausted. It is not always the case in others' in-situ compression results [102, 124, 127, 128]. The source positions were reported to be near the pillar top, in the middle of the pillar or even at the bottom of the pillar as influenced by microstructural features, sample dimensions, surface condition and testing parameters.

Compared to the dislocation starvation theory [77, 81], the exhaustion hardening theory [78, 82] is more suitable to explain the dislocation behaviour in this in-situ study, since dislocations remained in the pillars and multiplied. The competition between the dislocation nucleation rate relative to the dislocation annihilation rate leads to a continuous dislocation source. Pillar 1 in Group 1 shows work hardening due to dislocation accumulation in the pillar.

Yu et al. [101] demonstrated the source mechanism of <c+a> slip, proposed by Yoo et al. [129-131], based on the observation of c directional in-situ compression of Ti-5Al single crystals. They claimed that <c+a> dislocations are initiated from the junction of an <a> segment and a pre-existing <c> segment on the prismatic plane, although <c> segments were not observed in the pillar. Figure 6.1a-c shows a schematic formation of the <c+a> source they proposed. For pillars in Group 3, the

assumption of the existence of <c> dislocations on prismatic plane is invalid. Instead, the <c+a> LAGBs on the basal plane may affect the generation of <c+a> dislocations. Using a similar explanation to the above source mechanism, that <c+a> dislocations initiate from the junction of <a> segment and a pre-existing <c+a> segment on the basal plane (Figure 6.1d and e), is not feasible. By comparison, it is more possible that <c+a> dislocations directly emit from the probe/pillar contact surface. At least the contact surface has a higher stress concentration.

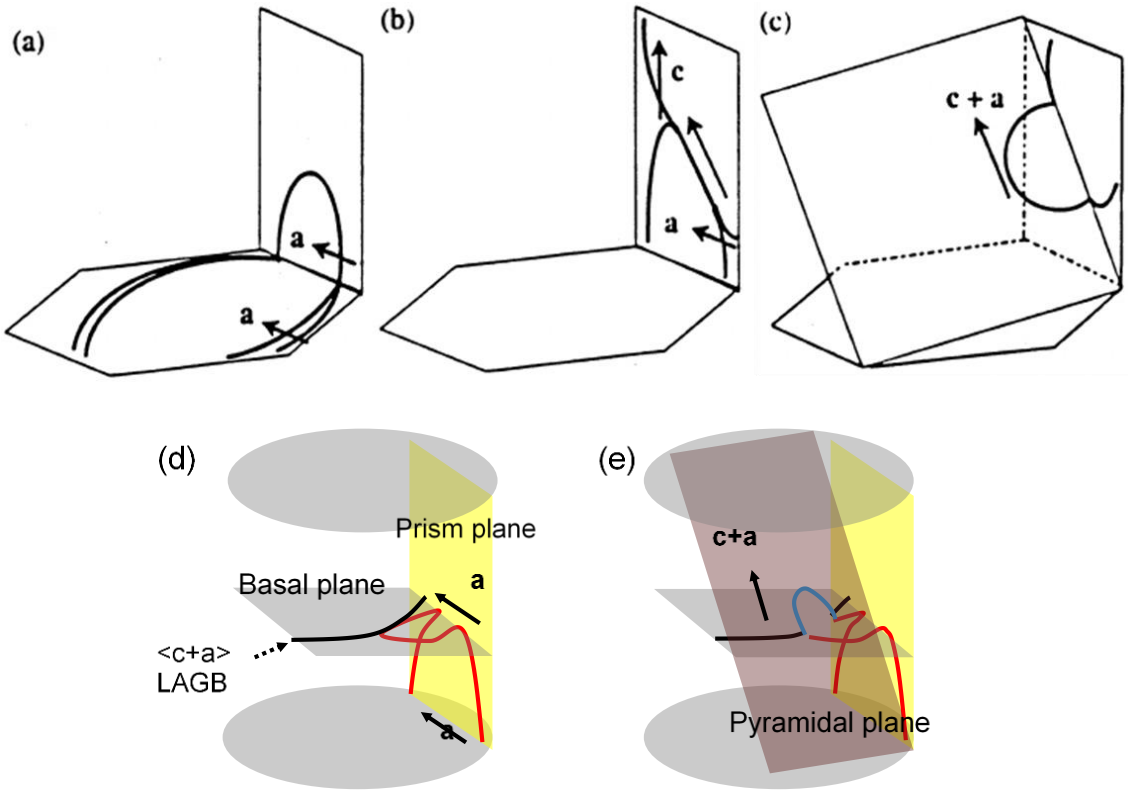

Figure 6.1 (a-c) Schematic source mechanism of <c+a> slip proposed by Yoo et al. [130]. (d-e) A derived source mechanism from this study where <c+a> LAGBs lie on the basal plane.

6.2.2. Dislocation motion velocity

Most of the dislocation movements in the in-situ tests are heterogeneous due to obstacles. Steady or jerky movements can be interpreted in terms of the Peierls mechanism [19] or the locking-unlocking mechanism [88]. The velocity of <a> basal slip in Group 1 and <c+a> pyramidal slip in Group 3 can be compared. The situation of Group 2 is more complex since two slip systems have been activated. For simplicity, assuming that the first emitted dislocation has the longest migration distance, the average velocity is calculated by dividing the distance of the front dislocation to the initial point by the time taken. For Pillar 2 in Group 1, it took 14.38s from the first emission of a dislocation to finalization (Figure 5.10d to 5.10n). The dislocation gliding distance is 0.62μm (Figure5.5d). The average velocity of <a> basal dislocation in Pillar 2 Group 1 is $4.3 \times 10^{-8}\ \mathrm{m/s}$. For Pillar 3 in Group 3, the first dislocation total gliding time is 98.11s (Figure 5.23c to 5.23k). The travel distance is 300nm (Figure 5.25c) in the projected plane, and 341.4nm corrected to the actual slip plane. The average velocity of <c+a> pyramidal slip in Pillar 3 Group 3 is $3.5 \times 10^{-9}\ \mathrm{m/s}$. <a> basal slip is 10 times faster than <c+a> pyramidal slip. Certainly, this is not the most appropriate way to represent the dislocation travel speed. The first dislocation in Pillar 2 Group 1 burst out half way of the whole distance at the beginning of plastic deformation, and moved forward unsteadily. Jerky movement of dislocations also exist in the Pillar 3 Group 3, not to mention the influence of the LAGB on the dislocation generation. However, this provides a qualitative perspective

to compare the speeds of different dislocations. The schematic diagrams in Figure 6.2 indicate the activated slip plane in different pillars of the three groups.

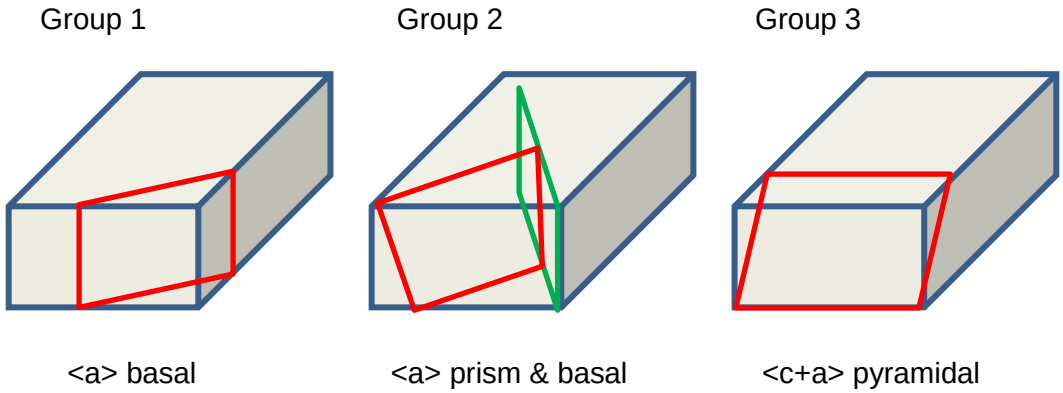

Figure 6.2 Schematic diagram of the activated slip planes in pillars of the three groups

6.3. Mechanical behaviours of different groups of pillars

Figure 6.3 shows the stress-strain curves for bulk compressed sample and different groups of in-situ compressed pillars. The black curve is recorded from the bulk compression test on the annealed sample. The red, green and blue curves are obtained from the compression test along $[12\bar{3}4]$ (Pillar 6 Group 1), $[\overline{20}8,12,7]$ (Pillar 2 Group 2) and $[0002]$ (Pillar 5 Group 3), respectively. The selected pillars underwent almost the largest deformation in the respective group. All three pillars were compressed using displacement control. The maximum displacement is 80nm for Pillar 5 Group 3 and 100nm for the other two pillars. Compared with the bulk sample, yield stresses are dramatically increased for micro-pillars. This is consistent with the

dislocation starvation hypothesis, where a small volume sustains high stress due to a lack of easy dislocation sources.

The yield points in the stress-strain curves for micro-pillars are where the slopes change distinctly, for example Point B on the red curve. Actually, it is not the start of plastic deformation but the first appearance of shear band on the free surface of the pillar. The first dislocation generates in the pillar long before observable yielding. In each curve, Point A, Point C and Point F are the start points where the first dislocation appears in the pillars. For Pillar 6 in Group 1, from Point A to Point B, the multiplication and accumulation of dislocations inside pillars instead of annihilation at the free surface suppressed strain bursts. Dislocations remaining in the pillars makes stress-strain curves to have no stress drop as in others' results [102, 123]. The strain burst at Point B is caused by the obvious formation of a slip step on the free surface as shown in Figure 5.12. After the glissile dislocations are exhausted, further plastic deformation proceeds through the nucleation of new dislocations which have to move through pinning obstacles, and consequently the stress increased. Since Pillar 2 in Group 2 has two slip systems activated, the yield strength is much lower than for the other two pillars. The first slip system was activated at Point C and the second slip system from around Point D. Slip steps formed from Point E. When loading along $[0002]$, <c+a> dislocations did not form obvious slip steps. Thus, the stress shows a nearly linear increase with strain in the blue curve. The strength of the c direction is higher than the $[12\bar{3}4]$ direction.

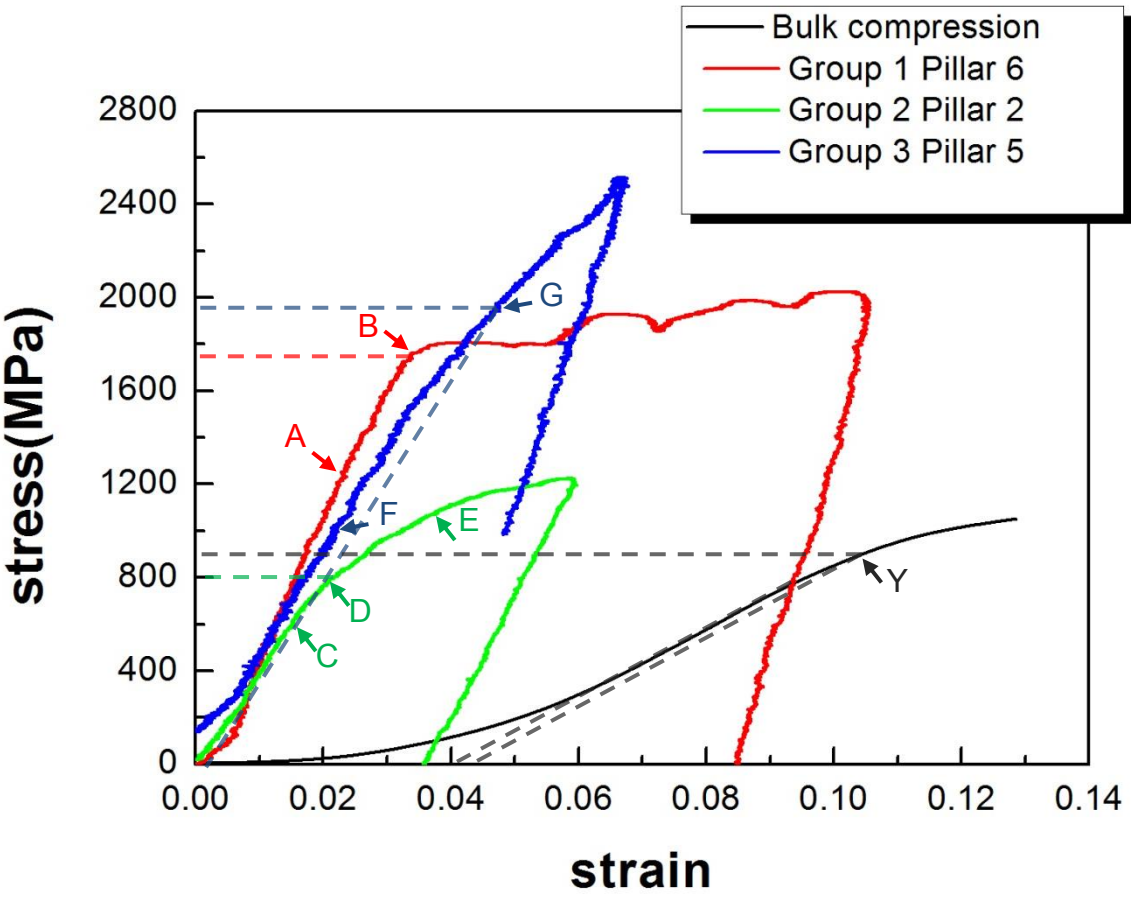

Figure 6.3 Stress-strain curves for bulk sample and micro-pillars in different groups with three loading axes. A, C, F are the start points of first dislocation appears in each pillar. B, D, G, Y are the yield points of each curve. E is where slip steps formed.

Table 5.6 compares properties of typical pillars in Group 1-3 with bulk sample. The mechanical properties are reserved from Figure 6.3. The pillars have higher strength corresponding to size effect. However the elastic moduli are unexpected lower than standard level (110 GPa) [1]. Except the inappropriate alignment of samples which may introduce elastic deformation and reduce E, other factors need to be considered such as loading mode.

Table 6.6 properties of typical pillars in Group 1-3 and bulk sample

	Group 1 Pillar 6	Group 2 Pillar 2	Group 3 Pillar 5	Bulk sample
Dimensions	0.48 x 0.5 x 1.2μm	0.4×1×2μm	0.4 x 0.8 x 1 μm	5×5×8 mm
Loading direction	$[12\bar{3}4]$	$[\overline{20}8,12,7]$	$[0002]$	Radial direction
Slip system	<a> basal	<a> prism & basal	<c+a> pyramidal	Multiple slip
Control mode	Displacement control	Displacement control	Displacement control	-
Strain rate	$1\times10^{-3}s^{-1}$	$0.67\times10^{-3}s^{-1}$	$0.67\times10^{-3}s^{-1}$	$1\times10^{-3}s^{-1}$
True elastic limit	1200MPa (Point A)	600MPa (Point C)	1000MPa (Point F)	-
yield strength	1750MPa (Point B)	800MPa (Point D)	1950MPa (Point G)	900MPa (Point Y)
E	66.6GPa	50GPa	33GPa	-

6.4. Influence of beam condition on the dislocation observation

When the viewing g vector is perpendicular to the loading direction, dislocations in the pillar keep in good contrast during compression. It is an ideal viewing g vector, since most bend contours are theoretically avoided in this way. However, the feasibility depends on the practical situation. Limited as it is by the tilting range of the single-tilt in-situ holder, a perpendicular g vector may not exist. Or, the dislocations to be observed are out of contrast with this reflection.

Chapter 7. Conclusions and future work

The dislocation configuration and deformation behaviour of Ti64 have been investigated in this study by both post-mortem and in-situ TEM experiments.

7.1. Conclusions

7.1.1. LAGB in the as-annealed specimen

The grown-in dislocations contained in the as-annealed specimen form two types of LAGBs: <a> and <c+a>. The <a> LAGB is formed by <a> dislocations with the same Burgers vector and lies on second order prismatic plane. The newfound <c+a> LAGB is formed by <c+a> dislocations with various Burgers vectors and lies on the basal plane. Due to different type of misfit dislocations existing on different β/α interfaces during phase transformation, the consequential LAGBs adopt specific crystallographic planes after annealing. Dislocation interaction may lead to a greater variety of <c+a> dislocations on their LAGB.

7.1.2. Planar slip and cross slip in the compressed sample

The heterogeneously distributed dislocations in the compressed specimen exhibit planar slip caused by the breakdown of SRO. The grown-in <c+a> LAGBs were not moved by compression and show a weak hindering effect on the generated slip bands. The slip bands are more sparsely distributed and specifically arranged near the <c+a> LAGBs, but relatively homogenously distributed without <c+a> LAGBs. <a> type screw dislocations repeatedly cross slip between the prismatic plane and

the first order pyramidal plane. Dislocation dissociation causes fringe patterns in pyramidal planes. The cross-slipped dislocations dissociated into extended dislocations on prismatic planes, which leads to strong residual contrast.

7.1.3. In-situ TEM compression test

Three groups of pillars were compressed in-situ in a TEM. The viewing g vector perpendicular to the loading direction is an ideal beam condition for imaging to avoid most bend contours.

In Group 1, single slip $\frac{1}{3}[11\bar{2}0](0002)$ was activated when compressing along $[12\bar{3}4]$. In Group 2, two slip systems were activated under $[\bar{2}\bar{0}8,12,7]$ loading, first $\frac{1}{3}[\bar{1}\bar{1}20](1\bar{1}00)$ and second $\frac{1}{3}[\bar{2}110](000\bar{1})$. In Group 3, the $\frac{1}{3}[1\bar{2}13](\bar{1}101)$ slip system was activated under c loading. <a> basal slip is more easily activated than other slip systems with similar or even larger Schmid factors.

Plastic deformation was always initiated at the probe/pillar interface. The competition between the dislocation nucleation rate relative to the dislocation annihilation rate leads to continuous creation of dislocations. Dislocation accumulation in the pillar causes work hardening. Eventually, slip results in the formation of steps on the free surface of the pillar and slightly relieves the strain. Increase of slip steps can be linked to stain bursts and load drops in the stress-strain curves.

Dislocation sources at other positions of the pillar were less favourable until the front part fully deformed and the source near the contact surface became exhausted. The dislocations emitted from other sources move much more quickly than the ones from the contact surface.

Planar slip exists in micro-pillars and is loading direction-dependent. Planar slip happened in <a> basal slip but not in <c+a> pyramidal slip, since the strong entanglement of dislocations led to uniform deformation. Surface effects and strain localisation also affect the generation of dislocations in pillars.

The pre-existing <c+a> LAGBs on basal planes prevented the motion of newly generated dislocations to some extent. The newly generated dislocations piled up at the LAGB and went through the boundary without changing its Burgers vectors when enough dislocations were accumulated. The LAGB remained on the basal plane during compression.

The pre-existing non-basal <c+a> dislocations were slightly activated during compression but for the most part were pinned and did not perform as dislocation sources during deformation. The pre-existing <a> dislocations observed were neither reactivated nor showed any interaction with newly generated dislocations due to inappropriate loading direction and/or pinning.

Most of the dislocation movements in the in-situ tests are heterogeneous due to the obstacles. The average velocity of <a> basal slip is $4.3 \times 10^{-8}\,\mathrm{m/s}$ and of <c+a> pyramidal slip is $3.5 \times 10^{-9}\,\mathrm{m/s}$. <a> basal slip is 10 times faster than <c+a> pyramidal slip.

Pillars start to yield when shear bands initiate on the free surface. The first dislocation generates in the pillar long before yielding. Compared with the bulk sample, yield stresses are dramatically increased for micro-pillars. This is consistent with the dislocation starvation hypothesis, where a small volume sustains high stress due to lack of easy dislocation sources. The strength on the c direction is higher than on the $[12\bar{3}4]$ direction. The pillar in Group 2 where were activated two slip systems has a much lower yield strength.

7.2. Future work

Based on the results obtained from the current study, some suggestions for future work are made as follows:

1. The Burgers vectors of <c+a> dislocations in the LAGB can be further confirmed by computer simulation.
2. The mechanism of dislocation dissociation needs to be further studied. EDS can be used to detect whether impurity concentrations exist in the areas with strong residual contrast.
3. Cross slip and dislocation dissociation have not been observed in in-situ tests. By changing the orientation of the pillars, these slip behaviors could be further investigated.
4. Mechanical properties of the existing pillars can be further analyzed from the deformation behaviours and corresponding stress-stain curves. More information can be digged from mobile dislocations and TEM images, for example, local stress and strain.
5. For in-situ mechanical testing, tensile testing is a good way to avoid sample buckling and get better images for dislocation observation. However, it has more challenges in sample preparation and experiment operation.

References

1. Lütjering G., Williams J.C., *Titanium.* 2007: p. 19-21.
2. Banerjee S., Mukhopadhyay P., *Phase Transformations: Examples from Titanium and Zirconium Alloys*. Vol. 12. Elsevier Science, 2010.
3. Lutjering G., Albrecht J., Ivasishin O.M., *Microstructure and Mechanical Properties of Conventional Titanium Alloys.* Microstructure/Property Relationships of Titanium Alloys, 1994: p. 65-74.
4. Picu R.C., Majorell A., *Mechanical behavior of Ti-6Al-4V at high and moderate temperatures - Part II: constitutive modeling.* Materials Science and Engineering A-Structural Materials Properties Microstructure and Processing, 2002. **326**(2): p. 306-316.
5. Rie K.T., Lampe T., *Thermochemical surface-treatment of titanium and titanium alloy Ti-6Al-4V by low-energy nitrogen ion bombardment.* Materials Science and Engineering, 1985. **69**(2): p. 473-481.
6. Burgers W.G., *On the process of transition of the cubic-body-centered modification into the hexagonal-close-packed modification of zirconium.* Physica, 1934. **1**: p. 561-586.
7. Mayeur J.R., McDowell D.L., *A three-dimensional crystal plasticity model for duplex Ti-6Al-4V.* International Journal of Plasticity, 2007. **23**(9): p. 1457-1485.
8. Zhang M., Zhang J., McDowell D.L., *Micro structure-based crystal plasticity modeling of cyclic deformation of Ti-6Al-4V.* International Journal of Plasticity, 2007. **23**(8): p. 1328-1348.
9. Lutjering G., *Influence of processing on microstructure and mechanical properties of (alpha+beta) titanium alloys.* Materials Science and Engineering A-Structural Materials Properties Microstructure and Processing, 1998. **243**(1-2): p. 32-45.
10. Yeh M.S.,Huang J.H., *Hydrogen-induced subcritical crack growth in Ti–6Al–4V alloy.* Materials Science and Engineering: A, 1998. **242**(1): p. 96-107.
11. Peters J., Ritchie R., *Foreign-object damage and high-cycle fatigue of Ti–6Al–4V.* Materials Science and Engineering: A, 2001. **319**: p. 597-601.
12. Fager D.N., Spurr W.F., *Some characteristics of aqueous stress corrosion in titanium alloys*, 1967, DTIC Document.
13. Lin F., Starke E., Chakrabortty S., Gysler A., *The effect of microstructure on the deformation modes and mechanical properties of Ti-6Al-2Nb-1Ta-0.8 Mo: Part I. Widmanstätten structures.* Metallurgical Transactions A, 1984. **15**(6): p. 1229-1246.
14. Schoenfeld S.E., Bimal K., *Texture effects on shear response in Ti–6Al–4V plates.* International Journal of Plasticity, 2002. **18**(4): p. 461-486.
15. Zhang M., *Crystal plasticity modeling of Ti-6Al-4V and its application in cyclic and fretting fatigue analysis.* Ph.D. Thesis, Georgia Institute of Technology, 2008.

16. Soeren M., Rene N., Sven G., *Influence of the Forming Temperature on the Microstructure and Mechanical Properties of Extruded Ti6Al4V Rods*, in *Proceedings of the 13th World Conference on Titanium*. 2016, John Wiley & Sons, Inc. p. 235-240.
17. Roylance D. *The Dislocation Basis of Yield and Creep*. Modules in Mechanics of Materials [a collection of web-based instructional modules funded by the Curriculum and Laboratory Improvement Program of the National Science Foundation] 2001.
18. Taylor G.I., *A theory of the plasticity of crystals.* Zeitschrift Fur Kristallographie, 1934. **89**(3/4): p. 375-385.
19. Petukhov B., *Dislocation Dynamics in a Crystal Lattice (Peierls-Nabarro) Relief.* Vardanian R.A. (Ed.), Crystal Lattice Defects and Dislocation Dynamics., Nova Science Publishers, New York (2000), pp. 71-108.
20. Nabarro F.R.N., *Dislocations in a Simple Cubic Lattice.* Proceedings of the Physical Society of London, 1947. **59**(332): p. 256-272.
21. Peierls R., *The size of a dislocation.* Proceedings of the Physical Society, 1940. **52**: p. 34-37.
22. Hirth J.P., *Dislocations in Solids: A Tribute to F.R.N. Nabarro*. revised ed. Vol. 14. 2011: Elsevier Science. p. 484.
23. Sakai T., Fine M.E., *Plastic-deformation of Ti-Al single-crystals in prismatic slip.* Acta Metallurgica, 1974. **22**(11): p. 1359-1372.
24. Boyer R., Welsch G., Collings E.W., *Materials properties handbook : titanium alloys.* ASM International, 1993: p. 1051-1056.
25. Williams J., Baggerly R., Paton N., *Deformation behavior of HCP Ti-Al alloy single crystals.* Metallurgical and Materials Transactions A, 2002. **33**(13): p. 837-850.
26. Bridier F., Villechaise P., Mendez J., *Analysis of the different slip systems activated by tension in a alpha/beta titanium alloy in relation with local crystallographic orientation.* Acta Materialia, 2005. **53**(3): p. 555-567.
27. Jones I.P., Hutchinson W.B., *Stress-state dependence of slip in Titanium-6Al-4V and other H.C.P. metals.* Acta Metallurgica, 1981. **29**(6): p. 951-968.
28. Vitek V., *Structure of dislocation cores in metallic materials and its impact on their plastic behavior.* Progress In Materials Science, 1992. **36**: p. 1-27.
29. Minonishi Y., Morozumi S., Yoshinaga H., *{1122} <1123> slip in titanium.* Scripta Metallurgica, 1982. **16**(4): p. 427-430.
30. Schmid E., Boas W., *Plasticity of Crystals, With Special Reference to Metals*. F A Hughes and Co Ltd, 1950.
31. Okamoto P.R., Thomas G., *On four-axis hexagonal reciprocal lattice and its use in indexing of transmission electron diffraction patterns.* Physica Status Solidi, 1968. **25**(1): p. 81-91.
32. Singh G., Sen I., Gopinath K., Ramamurty U., *Influence of minor addition of boron on tensile and fatigue properties of wrought Ti-6Al-4V alloy.* Materials Science and Engineering A-Structural Materials Properties Microstructure and Processing, 2012. **540**: p. 142-151.

33. Medina Perilla J.A., Gil Sevillano J., *Two-dimensional sections of the yield locus of a Ti-6%AL-4%V alloy with a strong trasverse-type crystallographic α-texture.* Materials Science and Engineering: A, 1995. **221**: p. 103-110.
34. Salem A.A., Semiatin S.L., *Anisotropy of the hot plastic deformation of Ti-6Al-4V single-colony samples.* Materials Science and Engineering A-Structural Materials Properties Microstructure and Processing, 2009. **508**(1-2): p. 114-120.
35. Savage M.F., Tatalovich J., Zupan M., Hemker K.J., Mills M.J., *Deformation mechanisms and microtensile behavior of single colony Ti-6242Si.* Materials Science and Engineering A-Structural Materials Properties Microstructure and Processing, 2001. **319**: p. 398-403.
36. Mayeur J.R., *Three Dimensional Modeling of Ti-Al Alloys with Application to Attachment Fatigue.* Master thesis, Georgia Institute of Technology, 2004.
37. Ding R.G., Gong J.C., Wilkinson A.J., Jones I.P., *<c+a> Dislocations in deformed Ti-6A1-4V micro-cantilevers.* Acta Materialia, 2014. **76**: p. 127-134.
38. Ding R.G., Gong J.C., Wilkinson A.J., Jones I.P., *Transmission electron microscopy of deformed Ti-6Al-4 V micro-cantilevers.* Philosophical Magazine, 2012. **92**(25-27): p. 3290-3314.
39. Paton N.E., Williams J.C., Rauscher G.P., *The deformation of α-phase titanium.* Titanium Science and Technology, 1973: p. 1049-1069.
40. Dunst D., Mecking H., *Analysis of experimental and theoretical rolling textures of two-phase titanium alloys.* Zeitschrift Fur Metallkunde, 1996. **87**(6): p. 498-507.
41. Fundenberger J.J., Philippe M.J., Wagner F., Esling C., *Modelling and prediction of mechanical properties for materials with hexagonal symmetry (zinc, titanium and zirconium alloys).* Acta Materialia, 1997. **45**(10): p. 4041-4055.
42. Lebensohn R.A., Canova G.R., *A self-consistent approach for modelling texture development of two-phase polycrystals: Application to titanium alloys.* Acta Materialia, 1997. **45**(9): p. 3687-3694.
43. Semiatin S.L., Bieler T.R., *Effect of texture changes on flow softening during hot working of Ti-6Al-4V.* Metallurgical and Materials Transactions A-Physical Metallurgy and Materials Science, 2001. **32**(7): p. 1871-1875.
44. Akhtar A., Teghtsoonian E., *Dislocation substructure in α-Ti single crystals.* Journal of Crystal Growth, 1975. **28**(2): p. 227-230.
45. Hull D., Bacon D.J., *Introduction to Dislocations*. Elsevier Science, 2011.
46. Read W.T., Shockley W., *Imperfections in Nearly Perfect Crystals*. Wiley New York, 1952.
47. Frank F.C., *Symposium on the plastic deformation of crystalline solids.* Carnegie Institute of Technology and the Department of the Navy Office of Naval Research, 1950: p. 150.
48. Nakamura A., Tochigi E., Shibata N., Yamamoto T., Ikuhara Y., *Structure and Configuration of Boundary Dislocations on Low Angle Tilt Grain Boundaries in Alumina.* Materials Transactions, 2009. **50**(5): p. 1008-1014.

49. Ikuhara Y., Nishimura H., Nakamura A., Matsunaga K., Yamamoto T., *Dislocation Structures of Low-Angle and Near-Σ3 Grain Boundaries in Alumina Bicrystals.* Journal of the American Ceramic Society, 2003. **86**(4): p. 595-602.
50. Oktyabrsky S., Kalyanaraman R., Jagannadham K., Narayan J., *Dislocation structure of low-angle grain boundaries in $YBa_2Cu_3O_{7-\delta}$/MgO films.* Journal of Materials Research, 1999. **14**(7): p. 2764-2772.
51. Shibata N., Morishige N., Yamamoto T., Ikuhara Y., Sakuma T., *Stacking-fault formation in [001] small-angle symmetric tilt grain boundaries in cubic zirconia bicrystals.* Philosophical Magazine Letters, 2002. **82**(4): p. 175-181.
52. Wang J., Beyerlein I.J., *Atomic structures of symmetric tilt grain boundaries in hexagonal close packed (hcp) crystals.* Modelling and Simulation in Materials Science and Engineering, 2012. **20**(2): p. 024002.
53. Balluffi R.W., Schober T., Komem Y., *Electron microscope studies of grain boundary dislocation behavior.* Surface Science, 1972. **31**(1): p. 68-103.
54. Lim A.T., Srolovitz D.J., Haataja M., *Low-angle grain boundary migration in the presence of extrinsic dislocations.* Acta Materialia, 2009. **57**(17): p. 5013-5022.
55. Lim A.T., *Migration and Mobility of Low-Angle Grain Boundaries.* Ph.D. thesis, Princeton University, 2012.
56. Liu B., Eisenlohr P., Roters F., Raabe D., *Simulation of dislocation penetration through a general low-angle grain boundary.* Acta Materialia, 2012. **60**(13-14): p. 5380-5390.
57. Lin D.L., Liu Y., *Microstructural evolution and mechanisms of superplasticity in large-grained iron aluminides.* Materials Science and Engineering A-Structural Materials Properties Microstructure and Processing, 1999. **268**(1-2): p. 83-89.
58. Lin D.L., Liu Y., *An electron back-scattered diffraction study on the microstructural evolution in large-grained iron aluminides during superplastic deformation.* Materials Science and Engineering A-Structural Materials Properties Microstructure and Processing, 2002. **329**: p. 863-871.
59. Liu B., Raabe D., Eisenlohr P., Roters F., Arsenlis A., Hommes G., *Dislocation interactions and low-angle grain boundary strengthening.* Acta Materialia, 2011. **59**(19): p. 7125-7134.
60. Moretti P., Miguel M.C., Zaiser M., Zapperi S., *Depinning transition of dislocation assemblies: Pileups and low-angle grain boundaries.* Physical Review B, 2004. **69**(21) : p. 214103.
61. Hemker K.J., Sharpe W.N., *Microscale characterization of mechanical properties*. Annual Review of Materials Research, 2007. **37**:p. 93-126.
62. Cai J., Li F.G., Liu T.Y., Chen B., *Microindentation study of Ti-6Al-4V alloy.* Materials & Design, 2011. **32**(5): p. 2756-2762.
63. Thouless M.D., *Modeling the Development and Relaxation of Stresses in Films.* Annual Review of Materials Science, 1995. **25**: p. 69-96.
64. Vlassak J.J., Nix W.D., *A New Bulge Test Technique for the Determination of Young Modulus and Poisson Ratio of Thin-Films.* Journal of Materials Research, 1992. **7**(12): p. 3242-3249.

65. Jung B.B., Ko S.H., Lee H.K., Park H., *Measurement of Young's modulus and Poisson's ratio of thin film by combination of bulge test and nano-indentation.* Advances in Fracture and Materials Behavior, Pts 1 and 2, 2008. **33-37**: p. 969-974.
66. Ding R.G., Gong J.C., Wilkinson A.J., Jones I.P., *Transmission electron microscopy of deformed Ti-6Al-4V micro-cantilevers.* Philosophical Magazine, 2012. **92**(25-27): p. 3290-3314.
67. Maekawa S., Takashima K., Shimojo M., Higo Y., Sugiura S., Pfister B., Swain M.V., *Fatigue tests of Ni-P amorphous alloy microcantilever beams.* Japanese Journal of Applied Physics Part 1-Regular Papers Short Notes & Review Papers, 1999. **38**(12B): p. 7194-7198.
68. Shade P.A., *Small scale mechanical testing techniques and application to evaluate a single crystal nickel superalloy.* Ph.D. thesis, The Ohio State University, 2008: p. 14.
69. Haque M.A., Saif M.T.A., *Strain gradient effect in nanoscale thin films.* Acta Materialia, 2003. **51**(11): p. 3053-3061.
70. Haque M.A., Saif M.T.A., *In-situ tensile testing of nano-scale specimens in SEM and TEM.* Experimental Mechanics, 2002. **42**(1): p. 123-128.
71. Gianola D.S., Eberl C., *Micro- and nanoscale tensile testing of materials.* JOM, 2009. **61**(3): p. 24-35.
72. Sevillano J.G., Arizcorreta I.O., Kubin L.P., *Intrinsic size effects in plasticity by dislocation glide.* Materials Science and Engineering A-Structural Materials Properties Microstructure and Processing, 2001. **309**: p. 393-405.
73. Ang W.C., Kropelnicki P., Soe O., Ling J.H.L., Randles A.B., Hum A.J.W., Tsai J.M.L., Tay A.A.O., Leong K.C., Tan C.S., *Novel development of the micro-tensile test at elevated temperature using a test structure with integrated micro-heater.* Journal of Micromechanics and Microengineering, 2012. **22**(8).
74. Espinosa H.D., Prorok B.C., Peng B., *Plasticity size effects in free-standing submicron polycrystalline FCC films subjected to pure tension.* Journal of the Mechanics and Physics of Solids, 2004. **52**(3): p. 667-689.
75. Bagdahn J., Sharpe W.N., Jadaan O., *Fracture strength of polysilicon at stress concentrations.* Journal of Microelectromechanical Systems, 2003. **12**(3): p. 302-312.
76. Demir E., Raabe D., Roters F., *The mechanical size effect as a mean-field breakdown phenomenon: Example of microscale single crystal beam bending.* Acta Materialia, 2010. **58**(5): p. 1876-1886.
77. Greer J.R., Nix W.D., *Nanoscale gold pillars strengthened through dislocation starvation.* Physical Review B, 2006. **73**(24): p. 245410.
78. Parthasarathy T.A., Rao S.I., Dimiduk D.M., Uchic M.D., Trinkle D.R., *Contribution to size effect of yield strength from the stochastics of dislocation source lengths in finite samples.* Scripta Materialia, 2007. **56**(4): p. 313-316.
79. Norfleet D.M., Dimiduk D.M., Polasik S.J., Uchic M.D., Mills M.J., *Dislocation structures and their relationship to strength in deformed nickel microcrystals.* Acta Materialia, 2008. **56**(13): p. 2988-3001.

80. Brenner S.S., *Tensile Strength of Whiskers.* Journal of Applied Physics, 1956. **27**(12): p. 1484-1491.
81. Greer J.R., Oliver W.C., Nix W.D., *Size dependence of mechanical properties of gold at the micron scale in the absence of strain gradients.* Acta Materialia, 2005. **53**(6): p. 1821-1830.
82. Rao S.I., Dimiduk D.M., Tang M., Parthasarathy T.A., Uchic M.D., Woodward C., *Estimating the strength of single-ended dislocation sources in micron-sized single crystals.* Philosophical Magazine, 2007. **87**(30): p. 4777-4794.
83. Jennings A.T., Li J., Greer J.R., *Emergence of strain-rate sensitivity in Cu nanopillars: Transition from dislocation multiplication to dislocation nucleation.* Acta Materialia, 2011. **59**(14): p. 5627-5637.
84. Kiener D., Motz C., Dehm G., Pippan R., *Overview on established and novel FIB based miniaturized mechanical testing using in-situ SEM.* International Journal of Materials Research, 2009. **100**(8): p. 1074-1087.
85. Dou R., Derby B., *A universal scaling law for the strength of metal micropillars and nanowires.* Scripta Materialia, 2009. **61**(5): p. 524-527.
86. Head A.K., *The Interaction of Dislocations and Boundaries.* Philosophical Magazine, 1953. **44**(348): p. 92-94.
87. Legros M., *In situ mechanical TEM: Seeing and measuring under stress with electrons.* Comptes Rendus Physique, 2014. **15**(2-3): p. 224-240.
88. Couret A., Crestou J., Farenc S., Molenat G., Clement N., Coujou A., Caillard D., *In situ deformation in T.E.M.: recent developments.* Microscopy Microanalysis Microstructures, 1993. **4**(2-3): p. 153-170.
89. Bernal R.A., Ramachandramoorthy R., Espinosa H.D., *Double-tilt in situ TEM holder with multiple electrical contacts and its application in MEMS-based mechanical testing of nanomaterials.* Ultramicroscopy, 2015. **156**: p. 23-28.
90. Hirsch P.B., Horne R.W., Whelan M.J., *Direct Observations of the Arrangement and Motion of Dislocations in Aluminum.* Philosophical Magazine, 1956. **1**(7): p. 677-684.
91. Whelan M.J., Hirsch P.B., Horne R.W., Bollmann W., *Dislocations and Stacking Faults in Stainless Steel.* Proceedings of the Royal Society of London Series A-Mathematical and Physical Sciences, 1957. **240**(1223): p. 524-538.
92. Sumino K., Sato M., *In-situ HVEM Observations of Dislocation Processes during High Temperature Deformation of Silicon Crystals.* Kristall und Technik, 1979. **14**(11): p. 1343-1350.
93. Farenc S., Caillard D., Couret A., *An in situ study of prismatic glide in α titanium at low temperatures.* Acta Metallurgica Et Materialia, 1993. **41**(9): p. 2701-2709.
94. Castany P., Pettinari-Sturmel E., Douin J., Coujou A., *In situ transmission electron microscopy deformation of the titanium alloy Ti-6Al-4V: Interface behaviour.* Materials Science and Engineering A-Structural Materials Properties Microstructure and Processing, 2008. **483-84**: p. 719-722.

95. Haque M.A., Saif M.T.A., *Application of MEMS force sensors for in situ mechanical characterization of nano-scale thin films in SEM and TEM.* Sensors and Actuators A-Physical, 2002. **97-8**: p. 239-245.
96. Oh S.H., Legros M., Kiener D., Gruber P., Dehm G., *In situ TEM straining of single crystal Au films on polyimide: Change of deformation mechanisms at the nanoscale.* Acta Materialia, 2007. **55**(16): p. 5558-5571.
97. Castany P., Pettinari-Sturmel F., Crestou J., Douin J., Coujou A., *Experimental study of dislocation mobility in a Ti-6Al-4V alloy.* Acta Materialia, 2007. **55**(18): p. 6284-6291.
98. Castany P., Besse M., Gloriant T., *In situ TEM study of dislocation slip in a metastable beta titanium alloy.* Scripta Materialia, 2012. **66**(6): p. 371-373.
99. Lee T.C., Robertson I.M., Birnbaum H.K., *TEM in situ deformation study of the interaction of lattice dislocations with grain boundaries in metals.* Philosophical Magazine A, 1990. **62**(1): p. 131-153.
100. Clark B.G., Ferreira P., Robertson I.M., *In Situ Electron Microscopy Methods.* Microscopy Research and Technique, 2009. **72**(3): p. 121-121.
101. Yu Q., Sun J., Morris J.W., Minor A.M., *Source mechanism of non-basal <c+a> slip in Ti alloy.* Scripta Materialia, 2013. **69**(1): p. 57-60.
102. Ye J., Mishra R.K., Sachdev A.K., Minor A.M., *In situ TEM compression testing of Mg and Mg-0.2 wt.% Ce single crystals.* Scripta Materialia, 2011. **64**(3): p. 292-295.
103. Bei H., Shim S., *Effects of focused ion beam milling on the nanomechanical behavior of a molybdenum-alloy single crystal.* Applied Physics Letters, 2007. **91**(11): p. 111915.
104. Picoindenter T., *PI 95 TEM PicoIndenter.* 2006: p. 8-9.
105. Kiener D., Motz C., Dehm G., *Micro-compression testing: A critical discussion of experimental constraints.* Materials Science and Engineering A-Structural Materials Properties Microstructure and Processing, 2009. **505**(1-2): p. 79-87.
106. Elmer J.W., Palmer T.A., Wong J., *In situ observations of phase transitions in Ti-6Al-4V alloy welds using spatially resolved x-ray diffraction.* Journal of Applied Physics, 2003. **93**(4): p. 1941-1947.
107. Suri S., Viswanathan G.B., Neeraj T., Hou D.H., Mills M.J., *Room temperature deformation and mechanisms of slip transmission in oriented single-colony crystals of an alpha/beta titanium alloy.* Acta Materialia, 1999. **47**(3): p. 1019-1034.
108. Menon E.S.K., Aaronson H.I., *Interfacial structure of widmanstatten plates in a Ti-Cr alloy.* Acta Metallurgica, 1986. **34**(10): p. 1975-1981.
109. Furuhara T., Howe J.M., Aaronson H.I., *Interphase boundary structures of intragranular proeutectoid α plates in a hypoeutectoid Ti-Cr alloy.* Acta Metallurgica Et Materialia, 1991. **39**(11): p. 2873-2886.
110. Hughes D.A., Hansen N., Bammann D.J., *Geometrically necessary boundaries, incidental dislocation boundaries and geometrically necessary dislocations.* Scripta Materialia, 2003. **48**(2): p. 147-153.

111. Seki Y., Watanabe H., Matsui J., *Impurity effect on grown-in dislocation density of InP And GaAs crystals.* Journal of Applied Physics, 1978. **49**(2): p. 822-828.
112. Wade C., Watanabe M., *Direct TEM/STEM Observation and Analysis of Bismuth Segregation to Grain Boundary Dislocation Cores in Bismuth Embrittled Copper Bicrystals.* Microscopy and Microanalysis, 2015. **21**(S3): p. 1743-1744.
113. Neeraj T., Hou D.H., Daehn G.S., Mills M.J., *Phenomenological and microstructural analysis of room temperature creep in titanium alloys.* Acta Materialia, 2000. **48**(6): p. 1225-1238.
114. Neeraj T., Mills M.J., *Short-range order (SRO) and its effect on the primary creep behavior of a Ti–6wt.%Al alloy.* Materials Science and Engineering: A, 2001. **319–321**: p. 415-419.
115. Xiao L., Umakoshi Y., *Cyclic deformation behaviour and dislocation structure of Ti-5 at.% Al single crystals oriented for double prism slip.* Philosophical Magazine A, 2002. **82**(12): p. 2379-2396.
116. Banerjee D., Williams J.C., *Perspectives on Titanium Science and Technology.* Acta Materialia, 2013. **61**(3): p. 844-879.
117. Brandes M., Mills M.J., *Static recovery in titanium alloys at lower temperatures.* Materials Science and Engineering A-Structural Materials Properties Microstructure and Processing, 2004. **387**: p. 570-575.
118. Li Y.F., Laird C., *Cyclic response and dislocation structures of AISI 316L stainless steel. I: Single crystals fatigued at intermediate strain amplitude.* Materials Science and Engineering A-Structural Materials Properties Microstructure and Processing, 1994. **186**(1-2): p. 65-86.
119. Xiao L., Umakoshi Y., *Cyclic deformation behaviour and saturation bundle structure in Ti–5 at.% Al single crystals deforming by single prism slip.* Philosophical Magazine, 2003. **83**(30): p. 3407-3426.
120. Mendelso.S, *Dislocation Dissociations In hcp Metals.* Journal of Applied Physics, 1970. **41**(5): p. 1893-1910.
121. Churchman A.T., *The slip modes of titanium and the effect of purity on their occurrence during tensile deformation of single crystals.* Proceedings of the Royal Society of London Series A-Mathematical and Physical Sciences, 1954. **226**(1165): p. 216-226.
122. Naka S., Lasalmonie A., Costa P., Kubin L.P., *The low-temperature plastic deformation of α-titanium and the core structure of a-type screw dislocations.* Philosophical Magazine A-Physics of Condensed Matter Structure Defects and Mechanical Properties, 1988. **57**(5): p. 717-740.
123. Ye J., Mishra R.K., Minor A.M., *Relating nanoscale plasticity to bulk ductility in aluminum alloys.* Scripta Materialia, 2008. **59**(9): p. 951-954.
124. Schneider A.S., Kiener D., Yakacki C.M., Maier H.J., Gruber P.A., Tamura N., Kunz M., Minor A.M., Frick C.P., *Influence of bulk pre-straining on the size effect in nickel compression pillars.* Materials Science and Engineering A-Structural Materials Properties Microstructure and Processing, 2013. **559**: p. 147-158.

125. Wang J., Zeng Z., Weinberger C.R., Zhang Z., Zhu T., Mao S.X., *In situ atomic-scale observation of twinning-dominated deformation in nanoscale body-centred cubic tungsten.* Nat Mater, 2015. **14**(6): p. 594-600.
126. Ye J., Mishra R.K., Pelton A.R., Minor A.M., *Direct observation of the NiTi martensitic phase transformation in nanoscale volumes.* Acta Materialia, 2010. **58**(2): p. 490-498.
127. David F.C., Takahito O., Ling Z., Jérôme L., Michelle D., Christopher S., John K., Margaret H., *Nanomechanical and in situ TEM characterization of boron carbide thin films on helium implanted substrates: Delamination, real-time cracking and substrate buckling.* Materials Science and Engineering: A, 2015. **639**: p. 54-64.
128. Imrich P.J., Kirchlechner C., Kiener D., Dehm G., *Internal and external stresses: In situ TEM compression of Cu bicrystals containing a twin boundary.* Scripta Materialia, 2015. **100**: p. 94-97.
129. Yoo M.H., *c+a dislocation reactions in H.C.P. metals.* Scripta Metallurgica, 1968. **2**(10): p. 537-540.
130. Yoo M.H., Agnew S.R., Morris J.R., Ho K.M., *Non-basal slip systems in HCP metals and alloys: Source mechanisms.* Materials Science and Engineering: A, 2001. **319-321**: p. 87-92.
131. Yoo M.H., Morris J.R., Ho K.M., Agnew S.R., *Nonbasal deformation modes of HCP metals and alloys: Role of dislocation source and mobility.* Metallurgical and Materials Transactions A-Physical Metallurgy and Materials Science, 2002. **33**(3): p. 813-822.